Observations of the Active Galactic Nucleus 1ES 1218+304 with the MAGIC-telescope

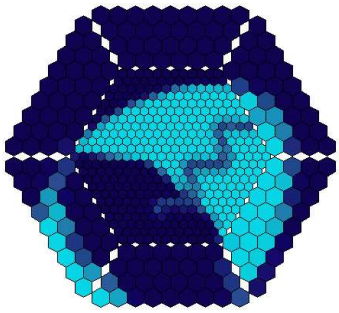

Dissertation zur Erlangung des naturwissenschaftlichen Doktorgrades der Bayerischen Julius-Maximilians-Universität Würzburg

THOMAS BRETZ
aus
Frankfurt am Main

Würzburg 2006

Abstract

The astronomical exploration at energies between 30 GeV and $\lesssim 350$ GeV was the main motivation for building the MAGIC-telescope. With its 17 m $\varnothing$ mirror it is the worldwide largest imaging air-Cherenkov telescope. It is located at the Roque de los Muchachos at the Canary island of San Miguel de La Palma at 28.8° N, 17.8° W, 2200 m a.s.l. The telescope detects Cherenkov light produced by relativistic electrons and positrons in air showers initiated by cosmic gamma-rays.

The imaging technique is used to powerfully reject the background due to hadronically induced air showers from cosmic rays. Their inverse power-law energy-distribution leads to an increase of the event rate with decreasing energy threshold. For MAGIC this implies a trigger rate in the order of 250 Hz, and a correspondingly large data stream to be recorded and analyzed. A robust analysis software package, including the general framework MARS, was developed and commissioned to allow automation, necessary for data taken under variable observing conditions.

Since many of the astronomical sources of high-energy radiation, in particular the enigmatic gamma-ray bursts, are of a transient nature, the telescope was designed to allow repositioning in several tens of seconds, keeping a tracking accuracy of $\lesssim 0.01°$. Employing a starguider, a tracking accuracy of $\lesssim 1.3$ minutes of arc was obtained.

The main class of sources at very high gamma-ray energies, known from previous imaging air-Cherenkov telescopes, are Active Galactic Nuclei with relativistic jets, the so-called high-peaked Blazars. Their spectrum is entirely dominated by non-thermal emission, spanning more than 15 orders of magnitude in energy, from radio to gamma-ray energies. Predictions based on radiation models invoking a synchrotron self-Compton or hadronic origin of the gamma-rays suggest, that a fairly large number of them should be detectable by MAGIC.

Promising candidates have been chosen from existing compilations, requiring high (synchrotron) X-ray flux, assumed to be related to a high (possibly inverse-Compton) flux at GeV energies, and a low distance, in oder to avoid strong attenuation due to pair-production in interactions with low-energy photons from the extragalactic background radiation along the line of sight. Based on this selection the first AGN, emitting gamma-rays at 100 GeV, 1ES 1218+304 at a redshift of $z = 0.182$, was discovered, one of the two farthest known AGN emitting in the TeV energy region. In this context, the automated analysis chain was successfully demonstrated. The source was observed in January 2005 during six moonless nights for 8.2 h. At the same time the collaborating KVA-telescope, located near the MAGIC site, observed in the optical band.

The lightcurve calculated showed no day-to-day variability and is compatible with a constant flux of $F(>100\,\mathrm{GeV}) = (8.7 \pm 1.4) \cdot 10^{-7}\,\mathrm{m^{-2}\,s^{-1}}$ within the statistical errors. A differential spectrum between 87 GeV and 630 GeV was calculated and is compatible with a power law of $F_E(E) = (8.1 \pm 2.1) \cdot 10^{-7}(E/250\,\mathrm{GeV})^{-3.0\pm0.4}\,\mathrm{TeV^{-1}\,m^{-2}\,s^{-1}}$ within the statistical errors. The spectrum emitted by the source was obtained by taking into account the attenuation due to pair-production with photons of the extragalactic background at low photon energies. A homogeneous, one-zone synchrotron self-Compton model has been fitted to the collected multi-wavelength data. Using the simultaneous optical data, a best fit model could be obtained from which some physical properties of the emitting plasma could be inferred. The result was compared with the so-called *Blazar sequence*.

Zusammenfassung

Die wesentliche Motivation zum Bau des MAGIC-Teleskops war die Untersuchung astronomischer Objekte zwischen 30 GeV und $\lesssim 350$ GeV. Mit einem 17 m $\varnothing$ Spiegel ist es das weltweit größte abbildende Luft-Cherenkov Teleskop. Es steht auf der Kanarischen Insel San Miguel de La Palma auf dem Roque de los Muchachos. Das Teleskop detektiert Cherenkov Licht von Elektronen und Positron aus Luftschauern, erzeugt von kosmischer Gammastrahlung.

Die abbildende Technik ist das Hauptmerkmal einer guten Unterdrückung des Untergrundes, der hauptsächlich aus Luftschauern der kosmischen Strahlung besteht. Ihre Energieverteilung, beschrieben durch ein steil abfallendes Potenzgesetz, führt zu einem starken Anstieg der Ereignisrate bei sinkender Energieschwelle. Für MAGIC bedeutet das Raten von etwa 250 Hz, was zu einem großen Datenstrom führt, der verarbeitet werden muss. Dazu wurde eine robuste Analyse Software, einschließlich des Grundgerüstes MARS, entwickelt und ihre Anwendung automatisiert. Dies ist nötig um wechselnde Beobachtungsbedingungen berücksichtigen zu können.

Da viele Quellen von Hochenergie Gammastrahlen, insbesondere die rätselhaften *Gamma-Ray Bursts*, stark veränderliche Phänomene sind, wurde das Teleskop so ausgelegt, dass es Neuausrichtungen innerhalb weniger Sekunden ermöglicht, und trotzdem eine Nachführgenauigkeit von $\lesssim 0.01^\circ$ erreicht, die mit einem *Starguider* auf $\lesssim 1.3'$ verbessert wird.

Die wichtigsten Quellen sehr hochenergetischer Gammastrahlung sind Aktive Galaktische Kerne mit relativistischen Jets, die sog. *high-peaked Blazars*. Ihr Spektrum erstreckt sich über mehr als 15 Größenordnungen, vom Radio- bis zum Gammabereich, und ist vollständig durch nichtthermische Strahlung dominiert. Modelle, die *synchrotron selbst-Compton* Strahlung oder Strahlung aus hadroninduzierten Kaskaden zu Grunde legen, sagen voraus, dass eine große Anzahl dieser Quellen von MAGIC zu detektieren sein müssten.

Vielversprechende Kandidaten wurden aus existierenden Katalogen ausgesucht mit der Anforderung eines großen Röntgenflusses (Synchrotronstrahlung), von dem erwartet wird, dass er einen großen Fluss bei GeV-Energien zur Folge hat. Außerdem wurden nur nahe Quellen ausgewählt um nicht von der Abschwächung des Flusses durch Paarbildung an der extragalaktischen Hintergrundstrahlung entlang der Sichtlinie betroffen zu sein. Basierend auf dieser Auswahl wurde zum ersten Mal Gammastrahlung von 100 GeV bei einem AGN (1ES 1218+304,$z = 0.182$) nachgewiesen. Hierbei wurde die automatische Analysekette erfolgreich demonstriert. Die Quelle wurde im Januar 2005 während sechs mondloser Nächte 8.2 Stunden lang beobachtet. Zeitgleich wurden Daten im optischen Bereich vom mitarbeitenden KVA-Teleskop aufgenommen.

Die berechnete Lichtkurve ist innerhalb der statistischen Fehler mit einem konstanten Fluss von $F(>100\,\mathrm{GeV}) = (8.7 \pm 1.4) \cdot 10^{-7}\,\mathrm{m^{-2}\,s^{-1}}$ verträglich. Das differentielle Spektrum wurde zwischen 87 GeV und 630 GeV bestimmt und ist innerhalb der statistischen Fehler mit einem Potenzgesetz $F_E(E) = (8.1 \pm 2.1) \cdot 10^{-7}\,(E/250\,\mathrm{GeV})^{-3.0\pm0.4}\,\mathrm{TeV^{-1}\,m^{-2}\,s^{-1}}$ vereinbar. Daraus wurde das von der Quelle emittierte Spektrum errechnet, indem die Paarbildung am extragalaktischen Hintergrund entlang der Sichtlinie berücksichtigt wurde. An das resultierende Spektrum und weitere gesammelte Multiwellenlängendaten wurde ein homogenes einzonen *synchrotron selbst-Compton* Modell angepasst. Unter Berücksichtigung der zeitgleichen optischen Daten konnten physikalische Größen des emittierenden Plasma bestimmt werden. Das Resultat wurde mit der sog. *Blazar-Sequenz* verglichen.

Contents

1. Introduction

Frau Sonne uns Licht und Leben schenkt,
Doch liebt sie nicht den, der da grübelt und denkt.
Drum müht sie sich ab gar manches Jahr,
Wie sie wohl schlau ihr Geheimnis bewahr'.
Doch jüngst kam der liebe Mond zu Gast,
Vor Freude begann sie zu leuchten fast,
Ist auch um ihr liebes Geheimnis gekommen –
Der Eddington hat es ja aufgenommen.

— Albert Einstein, 1919.

After Albert Einstein published his monumental work about special relativity in 1905 and the general theory of relativity in 1916, it was only a matter of time until **Black Holes** have been predicted. Since then these spectacular objects, which are fully described by only three parameters (mass, angular momentum and charge), fascinated everybody.

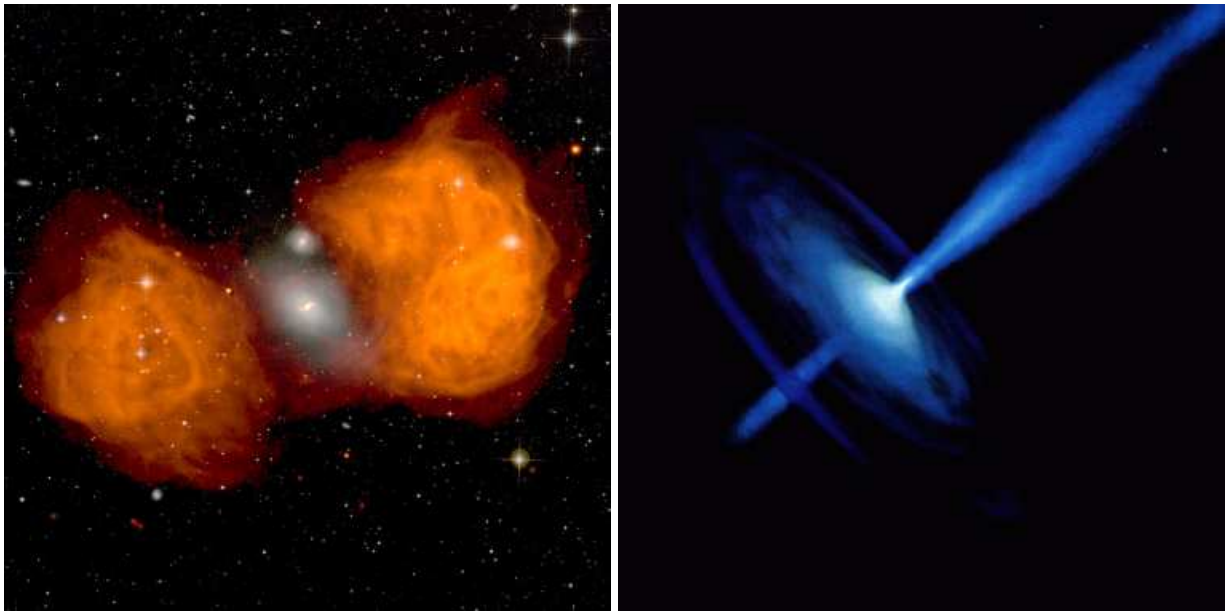

Figure 1.1.: Left: False colored multi-wavelength image of the galaxy Fornax A (www-01). Right: Artist impression of an Active Galactic Nucleus (www-02).

History This dissertation will describe the measurement of very high energy gamma-rays with a ground based detector, emitted from phenomena driven energetically by a black hole. Although the details of black holes and their environment will not be a main constituent of this thesis, a short outline of black hole's history (Müller, 2005) is given in the following paragraph.

After Karl Schwarzschild found the first solution of the theory of general relativity already in 1916, the Indian physicist Chandrasekhar discovered in 1930 that degenerated, relativistic matter below a critical mass ($\sim$1.4 solar masses, $M_\odot$) becomes a white dwarf. Five years later, searching vehemently for a counterargument, Sir Arthur S. Eddington showed, that the existence of this critical mass would allow heavier stars to collapse to an object whose gravitational field even photons could not escape. This photon-capture and the consequent shielding from the outside by an event horizon was discovered by Oppenheimer and Snyder (1939) calculating the collapse. The name HORIZON was introduced by Wolfgang Rindler in the 50's after Eddington and Finkelstein introduced a new coordinate system to get rid of the coordinate singularity of the Schwarzschild solution. A more general description also including rotation was introduced by Roy Patrick Kerr, 1963. One year afterward Roger Penrose assumed a singularity inside the horizon. Later he developed together with Stephen W. Hawking the singularity theorems for which the existence of a singularity is mandatory. So far these object were commonly named *frozen stars*, until it was replaced by the astronomer John Archibald Wheeler, who invented the name BLACK HOLE. He also introduced the so-called *no-hair theorem*, according to which a black hole does not have more than the three properties: mass, angular momentum and charge. In the years 1969 and 1971 the astrophysicists Lynden-Bell and Rees established the idea that accreting super-massive black holes are responsible for the enormous luminosity of *Active Galactic Nuclei* (AGN) and Quasars, the AGN-paradigm. At the same time, in 1970, Hawking proved that the extension of the event horizon is continuously increasing.
One year later the first candidate for a galactic black hole, Cygnus X-1, with a mass of 10 $M_\odot$ was identified by the Canadian Tom Bolton. Another two years later Nikolai Ivanovich Shakura and Rashid Alievich Sunyaev discovered a new solution for accretion, a flat, radiation-cooled disk (standard accretion disc or Shakura-Sunyaev-disk, SSD).
The so-called Hawking-radiation, i.e. the radiation of a black hole due to pair production taking place near the event horizon, was derived in 1975 theoretically. This mechanism is much too weak to be responsible for the high luminosities measured, e.g. in AGN. In 1977 R. D. Blandford and R. L. Znajek showed, that it is possible to extract rotational energy electromagnetically from the black hole, feeding the jets of AGN with electrons and positrons, so-called Blandford-Znajek-mechanism or Blandford-Znajek Poynting-flux.
In the 80's the X-ray satellite *Einstein* discovered objects with a luminosity of more than 10^{39} erg/s between 0.2 keV and 3.5 keV. The first all-sky survey at X-ray energy by the German-British ROSAT satellite launched in July 1990, showed that the X-ray background is made of a large number of faint and distant AGN (Hasinger et al., 1998).

Maybe the most challenging result from this observations was, that black holes could not only be detected by their gravitational impact, but high energetic radiation from their accretion disk could be measured directly. It turned out that a black hole with all its ambient processes was not *black* anymore but a colorful object for its observers, since the processes taking place in the

neighborhood of black holes emit radiation from the optical through many orders of magnitude into the very high energetic region. Here especially the corresponding processes are of interest because they accelerate particles to the highest energies currently known in our universe. For these highest energetic processes a huge accumulation of matter is necessary. While black holes feature the accretion of matter, a surrounding reservoir of matter must be available. By accreting matter from this reservoir the black holes become very massive ($>1000\,M_\odot$) forming so-called super-massive black holes ($\gtrsim 10^6\,M_\odot$). In the majority of cases this reservoir is the matter of a surrounding galaxy, in which such a super-massive black hole is hosted, which then is called *Active Galactic Nucleus*.

The surrounding matter (mainly gas, dust and occasional stars) is captured by the gravity of the black hole. Due to its angular momentum the attracted matter follows a spiral into the black hole forming a hot accretion disk. Viscous processes in this plasma generate enormous amounts of radiative energy. The central region of the accretion disk is quite small, approximately 10^{-4} pc in diameter. Around the central black hole there can be a large opaque torus extending several seconds of arc into the universe, containing a hot gas with embedded regions of high density. Energy from regions closer to the black hole can thus be absorbed by these clouds and reemitted, seen as emission lines in the spectrum.

Along the rotation axis a combination of the rotating magnetosphere of the black hole and the disk wind from the accretion disk collimates matter flowing out of the accretion disk. One or two relativistic jets perpendicular to the accretion disk carry a high energetic plasma away from the AGN. Inside the jets the highly energetic photons and particles of the plasma interact with each other and the intense magnetic field. These jets can extend as far as many tens of kiloparsecs from the central black hole.

For a review on black holes and its gravitation driven phenomena, as observed in AGN, see e.g. Begelman and Rees, 1995. Artistic views of AGN are shown in figure 1.2.

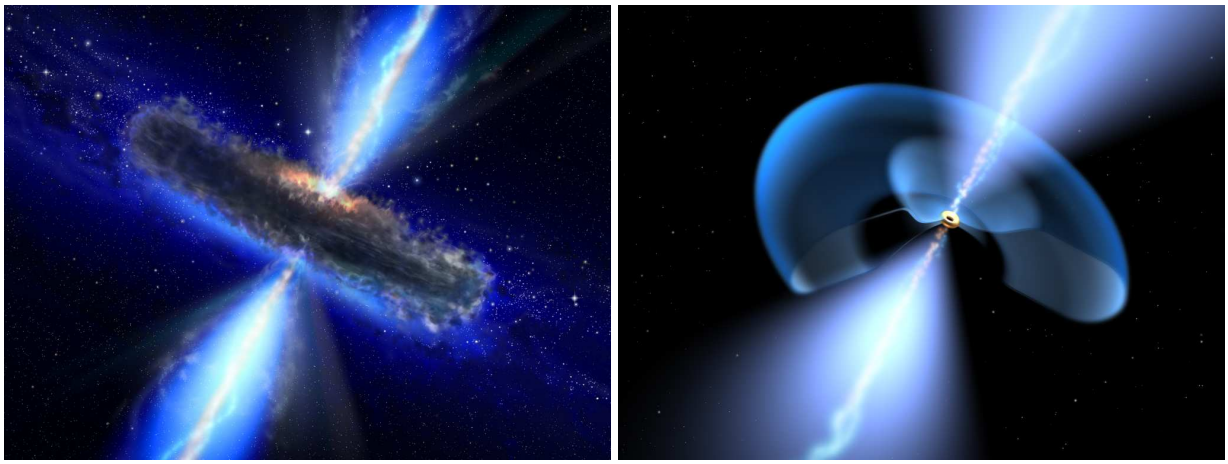

Figure 1.2.: Artistic view of an Active Galactic Nucleus (www-03) with the black hole in the center, the accretion disc (right, yellow), the huge dusty torus and two relativistic jets with shocks. The scale of the images is in the order of one lightyear.

The combination of the processes taking place produce radiation, mostly as non-thermal spectrum. Compared with this a thermal spectrum evolves in local thermal equilibrium, is continuous and has a common shape described by a single variable, its temperature. In astronomy thermal spectra are often called *blackbody* spectra. A blackbody is a theoretical object absorbing all photons, hence appearing black. It emits a thermal spectrum when heated.

The spectrum of AGN, which is not thermal, ranges through orders of magnitude from very low frequency radio to extremely energetic gamma rays (also γ-rays in the following, i.e. $E > 1$ MeV). It consists of synchrotron radiation in the radio to X-ray range and inverse Compton emission in the X-ray to gamma-ray region.

The highest energies seen are presumably produced by acceleration shocks. This mechanism has been suggested by Enrico Fermi, who also worked in Germany at the University of Göttingen in 1922, already in 1949 to explain the origin of high energy cosmic rays. In these shocks charged particles are reflected by a moving magnetic field, e.g. an interstellar magnetic field or the high magnetic field along the jets of an AGN. Depending on the relative direction in which the *magnetic mirror* is approached, the particles either gain or lose energy. Fermi argued, that the probability of a head-on collision is greater than a head-tail collision, so particles would, on average, be accelerated. This random process is nowadays also called *second order* Fermi acceleration, because the mean energy gain per bounce depends on the mirror velocity squared.

Whereas shocks without random motions are more efficient as they take place for example in jets or supernova remnants. In such an environment a charged particle, ahead of the shock front, can pass through the shock and then be scattered by magnetic inhomogeneities upstream the shock. The energy gain is due to the bounce and fly back across the shock, where it can be scattered again by magnetic inhomogeneities ahead of the shock. Repeating this process iteratively high energy gains are possible. This process is called *first order* Fermi acceleration due to its linear dependence on the shock velocity.

The resulting energy spectra in the case of relativistic particles are discussed in section 8.3.2. More about Fermi-acceleration can be found in, for example, Fermi (1949, 1954); Spitzer (1956); Wentzel (1963).

These accelerated charged particles A_{HE} can thus transfer their high energies to photons with lower energies γ_{LE} by inverse Compton scattering (see also figure 1.3):

$$A_{HE} + \gamma_{LE} \longrightarrow \gamma_{HE} + A_{LE} \tag{1.1}$$

Since Fermi-acceleration is independent of the particle mass either electrons or protons can be accelerated. Whereas protons may not produce a reasonable amount of inverse Compton radiation compared to electrons, because the scattering process is highly suppressed due to their higher mass, secondary electrons arising from photo-production through meson-decay may. Such hadronic models are discussed in e.g. Mannheim (1993) or Mücke and Protheroe (2001).

A possible source for these lower energy photons is synchrotron radiation produced by the same population of charged particles (Gould, 1965). Since the source population for the low energetic gammas and the accelerated charged particles are identical, this scenario is called *Synchrotron self-Compton* (SSC) model, e.g. Maraschi et al., 1992. In this case the energy distribution of the synchrotron radiation and the secondary high energy gammas would be identical and also show identical intensity variations.

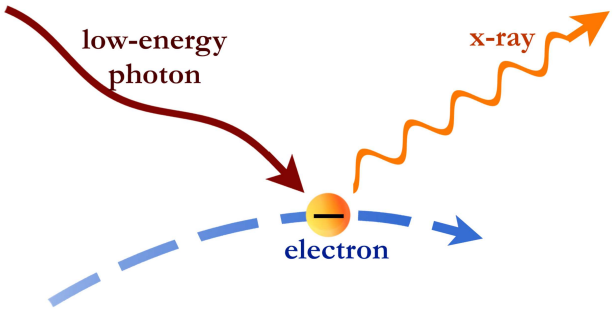

Figure 1.3.: Artistic view of the inverse Compton process. A low energetic photon gains energy by interaction with an electron of higher energy (www-04).

Another possible source for the low energy photon population are infrared to X-ray photons emitted by the jet and reflected back into the jet. In this case the low energy gamma population is independent of the accelerated charged particles and reflected by media beyond the jet. This scenario is called *External Compton* (EC) model, e.g. Dermer and Schlickeiser (1993); Blandford, R. D. (1993); Ghisellini et al. (1996). Possible external media are the accretion disk itself or a torus of dust around the accretion disk extending from the radius where dust sublimation occurs ($T \gtrsim 17.000\,\mathrm{K}$) out to several thousand seconds of arc, with a typical thickness in the order of 30 pc.

Even if often only one of both models is considered as the source of the observed emission, there is no reason why only one of both processes should be responsible for it. The observed emission might be a combination. A more detailed discussion of AGN can be found in the reviews by Antonucci (1993) and Urry and Padovani (1995) and references therein.

To learn more about the details of the acceleration process it is mandatory to measure the spectrum and time evolution of the emitted high energy particles. As emitted charged particles would be deflected by the magnetic field of the surrounding and our own galaxy, their origin cannot be reconstructed. For its correct reconstruction the path between their source and the observer should be unbiased. Therefore neutrons and gammas-rays must be considered as good candidates. Neutrons, because of the absence of any charge, are difficult to detect and thus can be omitted. Consequently the detection of gamma-rays is discussed hereafter.

The gamma-rays emitted by AGN must have a very low flux due to their high energy, because the energy density per unit energy must not be divergent. To be able to measure these low fluxes either a lot of observation time or a huge collection area is necessary. As of their high probability for pair production in the earth's atmosphere a direct measurement at ground level is impossible. Instead direct measurements are performed by satellite experiments, e.g. EGRET (in past), SWIFT (ongoing), and GLAST (in future). As a result of the relatively small workload of todays spacecrafts the collection area of the detectors is limited to the order of one square meter by their weight, which can only partly be compensated by their measurement around-the-clock. The low flux and the small effective area thus limit the maximum energy detectable by previous and running experiments in the order of several GeV.

What is a problem for direct measurement on ground level – the atmosphere – turns out to

be lucky chance for indirect measurements. While the probability of pair production in the atmosphere is too high for the gamma-rays to reach ground level without previous interaction, exactly these interactions forces the initiation of electro-magnetic cascades in the atmosphere. Because of the high energy of the primary particle many of the secondary charged particles still have energies high enough to have a velocity faster than the speed of light in the atmosphere and consequently emit Cherenkov radiation. Exactly this radiation provides the possibility to investigate the properties of the primary particle by measuring the Cherenkov light pool of its secondaries. This cascades take place high in the atmosphere allowing a measurement of its Cherenkov light (e.g. Bretz, 1999) from far away. Having the atmosphere as conversion volume of such a detector an effective collection area after background suppression in the order of one square kilometer can be reached, which corresponds to an area in the order of $\sim$0.1 km^2 after current state-of-the-art analysis (cf. figure 4.20). Since the measurable light yield is directly coupled with the energy of the primary particle, and the quality of the shower reconstruction depends on the measured statistics, this technique is not well suited for energies below $\sim$10 GeV.

A schematic and an artist view of an air shower can be found in figure 1.4.

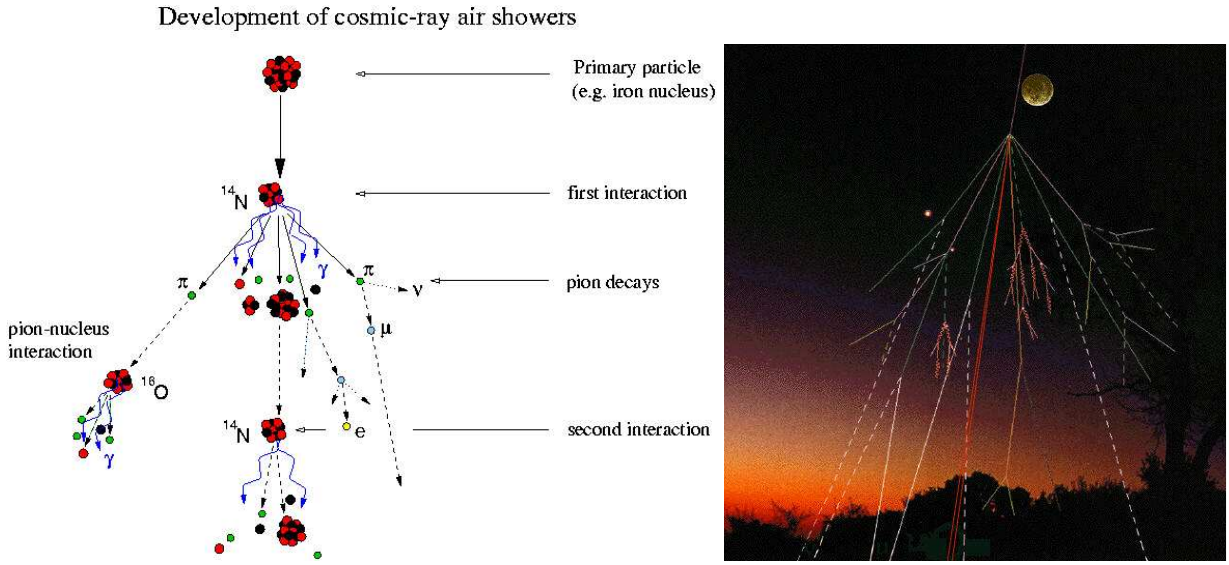

Figure 1.4.: Left: Simplified scheme of the development of a cosmic air shower initiated by the interaction of a nucleus with Nitrogen atom from the atmosphere (www-05).
Right: Artist view of an air shower (www-06).

Measuring the Cherenkov light reaching ground level in an imaging device offers the possibility to reconstruct the main properties of the primary particles: particle type, incident direction and its energy. After the seminal paper by Morrison (1958) it took more than 30 years until Weekes et al. (1989) could finally prove, by a high significant signal from the measurement of the Crab Nebula with the Whipple telescope, that the reconstruction of these properties can be achieved well enough to produce a reasonable physical output. The first measurements of these types of very high energetic showers were done with simple photographic films by Hill and Porter, 1960.

An image recorded by Jelley and Porter (1963) is shown in figure 1.5.

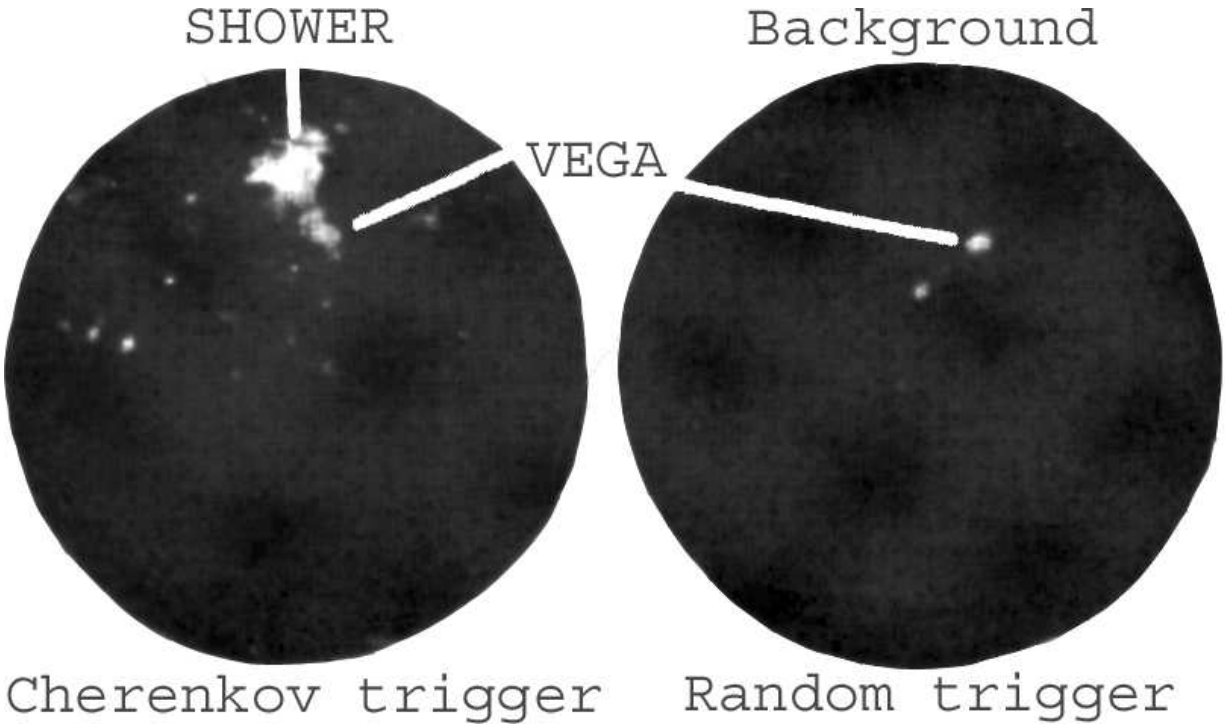

Figure 1.5.: Direct image of Cherenkov light from an extended air shower (left), taken with an image intensifier and an exposure time of $\sim 10\,\mu$s, published by Jelley and Porter, 1963. The right image shows the corresponding randomly triggered background measurement. A star of magnitude ~ 0, Vega, in the field of view, gives some idea of the brightness of the shower image. The scale of the image is in the order of a few degree.

It turned out, that for showers of lower energies a better light collection had to be achieved. Therefore a reflecting surface (mirror) has been used focusing the Cherenkov light onto a detector in the focal plane. Using a high sensitivity detector built of photo multiplier tubes (PMT), images of air showers induced by TeV primaries could be recorded and properly analyzed. This technique nowadays is well known as Imaging Air-Cherenkov Technique, and a lot of Imaging Air-Cherenkov Telescopes (IACT) have been built in the past few years, e.g. HEGRA and Whipple (Bradbury and Rose, 2002). Currently a new generation of IACT is build. These are H.E.S.S. and CANGAROO III (Kubo et al., 2004) in the southern and the successor of Whipple VERITAS (Weekes et al., 2002) and MAGIC (Lorenz, 2004) in the northern hemisphere. H.E.S.S. was the first of these to come online and recent observations have produced a wealth of new discoveries (Aharonian et al., 2005). After the MAGIC-telescope was inaugurated in autumn 2004 now also the first VERITAS telescope starts operation (Holder et al., 2006). A second MAGIC-telescope (Beixeras et al., 2005) for stereoscopic observations, further increasing sensitivity and energy resolution (Pühlhofer et al., 2003), is under construction, see figure 1.6.

Figure 1.6.: Picture of the MAGIC site with the telescope (left) in operation and the second telescope (center), which is currently under construction. The picture was taken by D. Dorner in March 2006 at sunset. On the right the William-Hershel optical telescope (left) and the Swedish solar telescope (right) can be seen.

A review of high and very high energy astronomy can be found in Weekes, 2003.

Whereas the small effective detection area of satellite experiments for gamma-rays limited the highest detectable energies to several GeV, the last generation of Cherenkov telescopes was limited to energies above $\sim$350 GeV by their small light collection area (mirrors).

Furthermore roughly ten times less sources could be detected in total by IACT than by previous satellite missions though their sensitivity in terms of power per unit energy was comparable (Weekes, 2003). Although the EGRET experiment could detect more than 60 discrete extragalactic sources (Hartman et al., 1999) in the MeV to GeV energy range and more than 50 sources in total above 1 GeV (Lamb and Macomb, 1997), but only a handful of sources could be discovered to emit at TeV energies.

This discrepancy can be explained by attenuation along the line of sight (Stecker et al., 1992) or attenuation in the source region itself (Mannheim, 1993). In both cases the most likely cause for this attenuation is pair-production with photons at infrared to ultraviolet frequencies. Due to the energy cutoff by pair-production along the line of sight (Fazio and Stecker, 1979), increasing with

distance and asymptotically reaching ∼50 GeV (Kneiske et al., 2004), a lower energy threshold will allow the discovery and survey of more and more distant sources. This can be visualized in a diagram showing the cut-off energy, which is defined as the energy at which the flux has been attenuated by a factor e, versus distance also known as *Fazio-Stecker relation*. It is shown in figure 1.7.

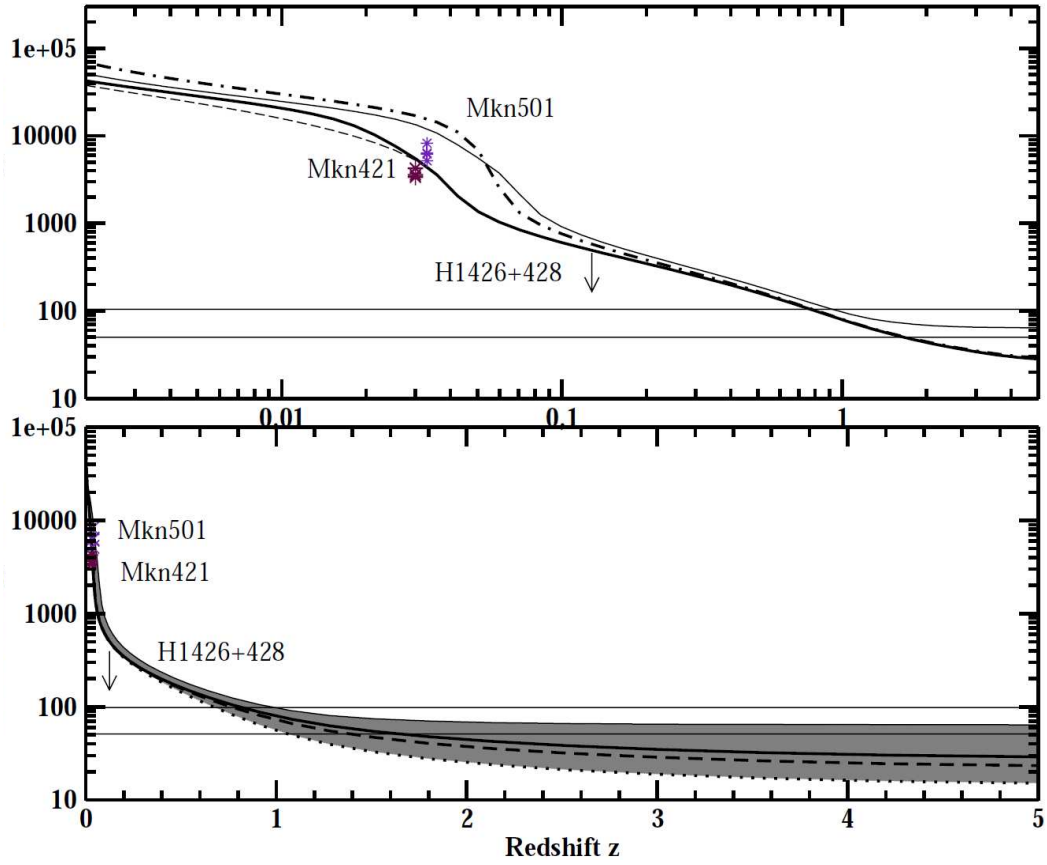

Figure 1.7.: Fazio-Stecker relation from (Kneiske et al., 2004) with logarithmic (top) and linear (bottom) distance-scale. The relation shows the energy at which the flux of a source at distance z (redshift) has been attenuated by a factor e due to pair-production along the line of sight. Sources for which the cut-off energy could be determined are included. The curved lines describe different models. The horizontal lines at 50 GeV and 100 GeV are guide-lines to show the change in distance accessible lowering the energy threshold of todays Cherenkov telescopes to or below 100 GeV.

The following work will discuss one of the new generation ground based Cherenkov detectors, the MAGIC-telescope. It was built to observe in the so far unexplored energy domain between 50 GeV and 350 GeV, e.g. Moralejo et al. (2003); Albert et al. (2005). The discovery of one of the farthest sources known yet to emit gamma-rays in this energy domain and the first one clearly detected at 100 GeV, the Active Galactic Nucleus 1ES 1218+304 (Elvis et al., 1992; Urry et al.,

2000), will be presented. Its measured spectrum and the effect of pair-production along the line of sight are discussed.

The MAGIC-telescope was designed to allow the detection of faint air showers initiated by cosmic gamma-rays at very high energies, which are emitted by the AGN introduced above, but also objects like super nova remnants or Gamma Ray Bursts (GRB). GRB are a violent transient phenomenon, first published in Klebesadel et al., 1973. Only visible for seconds to minutes they can be the brightest extrasolar objects on the sky.

Owing to the large fluctuations of low-energy showers, geomagnetic effects, as well as additional background from electrons and muons, background suppression at low energies is the most challenging task in Cherenkov astronomy.

Therefore novel analysis methods for low-energy events had to be developed. Starting with a conventional analysis, based on image parameters obtained from moments of the light distribution in the camera, a software project coined *Standard Analysis* was started allowing the testing and inclusion of novel analysis tools. Due to the large amount of data recorded by the MAGIC data acquisition system, stability and automation of the analysis chain were essential (Dorner and Bretz, 2005; Dorner et al., 2005). Since the implemented algorithms have to be as robust and failsafe as possible, for example, the number of free parameters in cutting distributions must be kept minimal. Other design goals were simple maintenance and flexibility in order to allow adaption to ongoing development of new analysis methods. The event-based analysis package MARS [1] (www-07) has proven to be a suitable solution for this challenging project. The package is based on a modular concept and internal coherence (Bretz, 2003, 2004; Bretz and Dorner, 2005). The output of the standard analysis serves as a reference for more specialized analyzes on individual data sets.

The complete analysis chain has been implemented. Running the standard analysis delivers a set of plots characterizing data quality, image parameter distributions, signal excesses, energy spectra, etc., i.e. sufficient information to allow a comprehensive first assessment of the scientific content of the data. In the case of tentatively interesting results from standard analysis more advanced and specialized investigations can be launched, all attachable to the MARS framework.

After an outline of the telescope's hardware in the following the main steps relevant for analysis are discussed. The automation of these steps is presented, based on the MARS-framework as described in (Bretz, 2003, 2004; Bretz and Dorner, 2005). With this successful concept two new AGN, namely 1ES 1218+304 (Elvis et al., 1992; Urry et al., 2000) and PG 1553+113 (Green et al. (1986), see also Aharonian et al., 2006), could already be discovered to emit in the TeV energy region. For 1ES 1218+304 a more refined analysis will be presented and discussed. Explaining the analysis steps the time evolution of the data quality for the MAGIC data taken so far will be discussed to show, that the data included in the presented analysis is well suited.

After the results of this analysis are presented, some fundamentals about AGN and the corresponding acceleration and emission processes are outlined. Based on the measurement, conclusions for the currently most popular AGN-models, allowing TeV emission, are drawn.

[1] MAGIC **A**nalysis and **R**econstruction **S**oftware

2. Hardware Framework

The most exciting phrase to hear in science
– the one that heralds new discoveries –
is not "Eureka!" but "That's funny . . . "
— Isaac Asimov.

Figure 2.1.: Bird's-eye view of the MAGIC site. Telescope with the control house (south-east) and the hotel like living rooms (north-west). © Google, 2006 (www-08)

The MAGIC-telescope designed to detect air showers with trigger rates above 250 Hz is located at the Roque de los Muchachos at the Canary island San Miguel de La Palma (28.8° N, 17.8° W, 2200 m above sea level). Figure 2.1 shows a satellite picture of the site.

The main reflector of the MAGIC-telescope is an isochronous, tessellated 17 m dish (Bastieri et al., 2005) controlled by an automatic adjustment system maintaining the parabolic shape during pointing and tracking maneuvers. The triggered events are digitized by a 300 MHz FADC system, providing sufficient time resolution (∼3 ns) to resolve different temporal structures in the air shower images, induced due to their hadronic or gamma-ray origin. See also Cortina et al., 2005. To achieve this, a large data stream must be recorded and archived for the analysis. The signal charge and arrival time is calculated from these samples, see Bartko et al., 2005.

One of the main goals of the MAGIC-telescope project is the potential discovery of gamma-rays from Gamma Ray Bursts (GRB). From observations at other wavelengths it is known, that the typical duration of bursts is below one minute. A distribution of GRB durations measured by the BATSE-experiment (Paciesas et al., 1999), on board the satellite Compton Gamma Ray Observatory, is shown in figure 2.2. Even without any preselection cuts is shows the typical bimodality of GRB durations, assumed to have different physical origins, e.g. Dermer (2002); Janiuk et al. (2006). The most popular explanation for the emission is a relativistic fireball (Waxman, 1995; Meszaros and Rees, 1997).

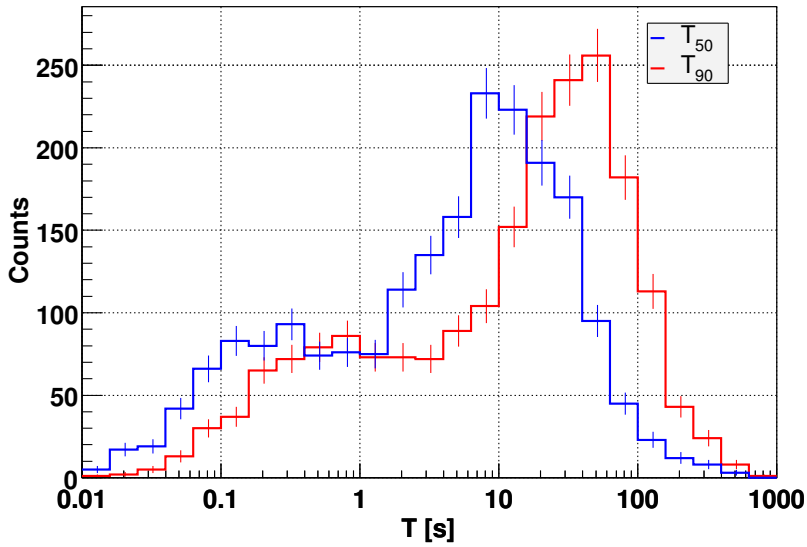

Figure 2.2.: Distribution of GRB durations from all GRB of the fourth BATSE-catalog (Paciesas et al., 1999). T_x is the time duration in which the burst has lost x-percent of its luminosity.

2.1. Tracking system

2.1.1. Requirements

Aiming to reposition the telescope within a time windows allowing to observe the population of long duration GRB (see figure 2.2), it was essential to build a light weight structure and a drive system able to move more than 60 tons fast and accurate enough. To follow the movement of the stars on the sky, it is necessary to have a tracking accuracy small compared to the point-spread function for a point-like source reconstructed in gamma-rays. While for fast repositioning the telescope has to be moved with $\sim 10^\circ/\mathrm{s}$, tracking stars expects velocities in the order of $\sim 10^\circ/\mathrm{h}$. Values of typical point-spread functions, depending on the primary energy of the particle, are between 0.05° and 0.1° demanding a tracking accuracy better than 0.05° ($\simeq 3'$).

With 50% of the possible performance, currently limited to security issues, several gamma-ray burst could already be observed with pointing times well below 25 s. No emission has been detected so far. Two of them could be observed already in the phase of prompt emission with pointing times $\lesssim 10$ s, namely GRB 050713a (Albert et al., 2006) and GRB 050904.

2.1.2. Implementation

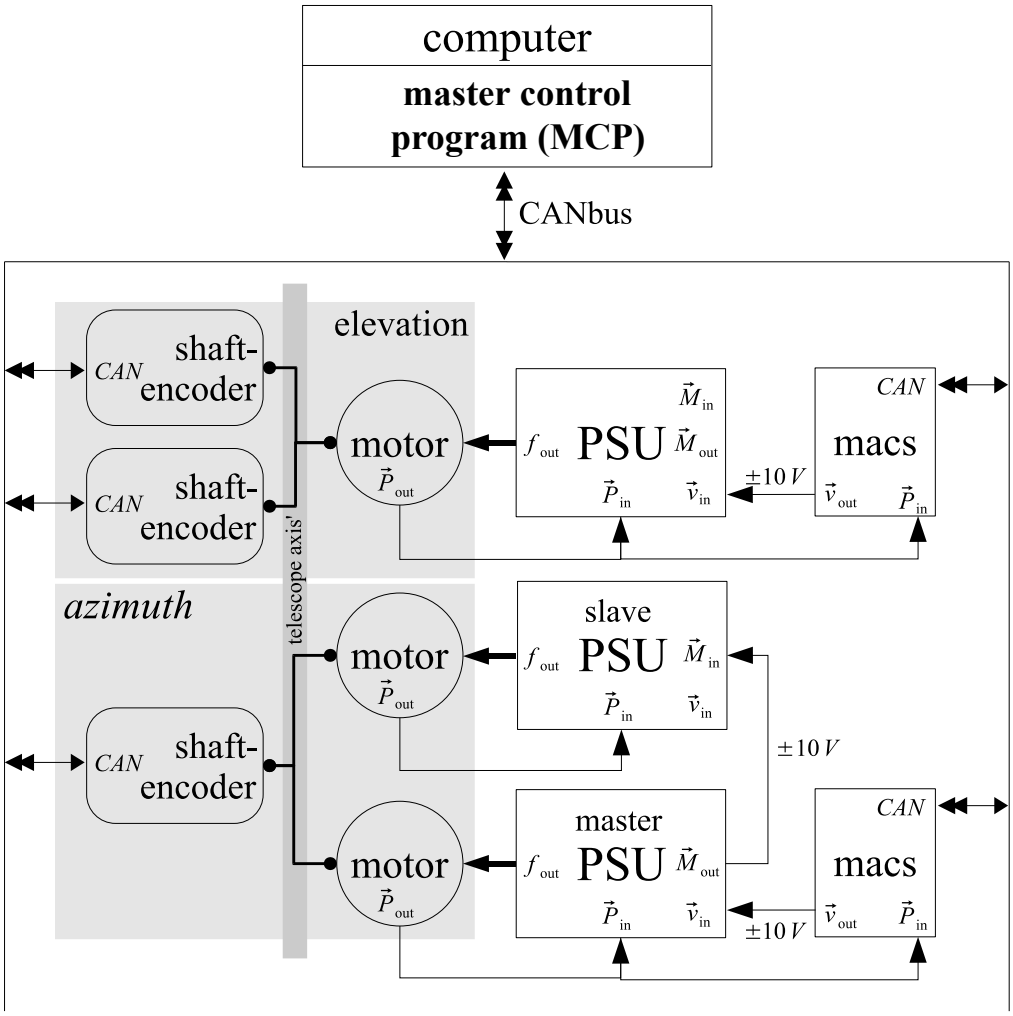

Figure 2.3.: Scheme of the implementation of the drive system of the telescope. A detailed explanation is given in the text.

To achieve this accuracy and the fast movement a drive system based on three 11 kW servo motors has been built. Two motors are necessary for the movement in azimuth, one in elevation. The two motors on the azimuth axis are synchronized in a master/slave mode by their nominal torques. The positions of the three motor are read out by three relative rotary encoders. The

positions of the telescope axes are measured by three 14 bit absolute shaftencoders, i.e. with an accuracy of $\sim 1.3'$, which results in an accuracy of controlling the motion of the telescope in the order of $1'$. The motors are controlled by microprocessor driven power-supplies, to which the signal of the rotary encoder are fed back. The power-supplies, corresponding to the two axes, are controlled themselves by micro-controllers communicating via CANbus with a computer running the master control program (MCP). The nominal speed of the motors calculated by the MCP are converted to a voltage of ± 10 V serving as an input for the power supplies. The calculation takes the shaftencoder positions (read out by CANbus, too) and the motor positions into account.

A scheme of the implementation is given in figure 2.3.

2.1.3. Astrometric corrections

The astrometric corrections necessary pointing any position in the sky are well described in (Dorner, 2003; Riegel, 2005). The implementation is based on the positioning library SLALIB programmed by Patrick Wallace (www-09) and used by several observatories like the KECK-telescopes.

2.1.4. Calibration – Pointing correction

The calibration of the pointing position is done using a pointing model, which is an analytical model describing the differences between an ideal and a real telescope, which differences are due to

- non accurate zero position of the position measurement
- misalignment of the axes
- non perpendicularity of the axes
- bending of the structure
- backlash of parts of the drive system

To calibrate the model, i.e. determine the coefficients, the nominal and the real pointing position are compared. Therefore bright stars are tracked. With a CCD camera the position of the bright star in the camera is measured and hence the real pointing position of the telescope is calculated. For this purpose the reference position in the camera, its center, is determined by investigating the positions of six LED fixed at the border of the PMT camera (Riegel et al., 2005). Having enough of these datasets (nominal, real pointing position) available, a fit of the coefficients of the model can be made to find the best conversion from the nominal into the real positions or vice versa.

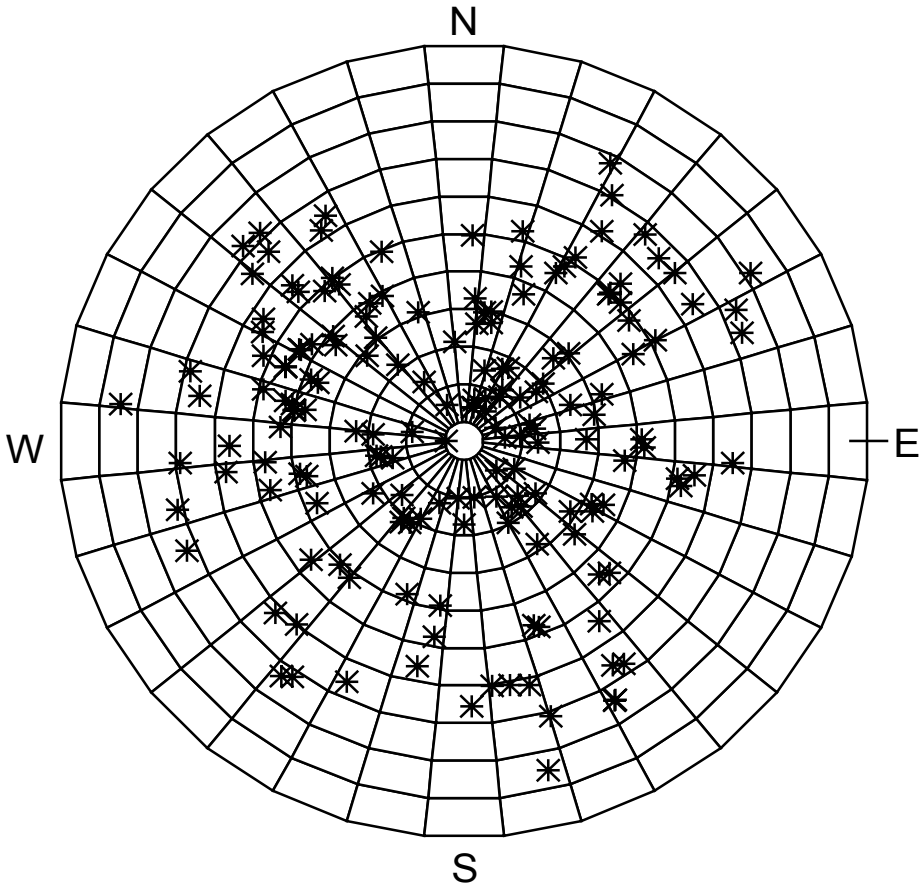

Figure 2.4.: Distribution of datasets taken around August 2005 in local coordinates. The border corresponds to the horizon, the center to the Zenith.

2.1.5. Tracking accuracy

Applying this model to 173 datasets taken around August 2005 (figure 2.4), the systematic tracking accuracy can be improved from (6.0 ± 1.2) arcmin to (1.1 ± 0.7) arcmin by taking into account the effects discussed before. This systematics are in the same order than the motion control can be achieved by the hardware. The distribution of absolute residuals on the sky before (already including an offset correction) and after applying the corrections is shown in figure 2.5.

As each time such a dataset is recorded also the present residual is measured, an overview table with the average systematic tracking uncertainty and its spread for the last two years of observation can be compiled. It is shown in table 2.1. These absolute values give a good estimate of the tracking accuracy achieved but do not serve as an unbiased measurement, because the precise result also depends on the precise positions on the sky which were measured.

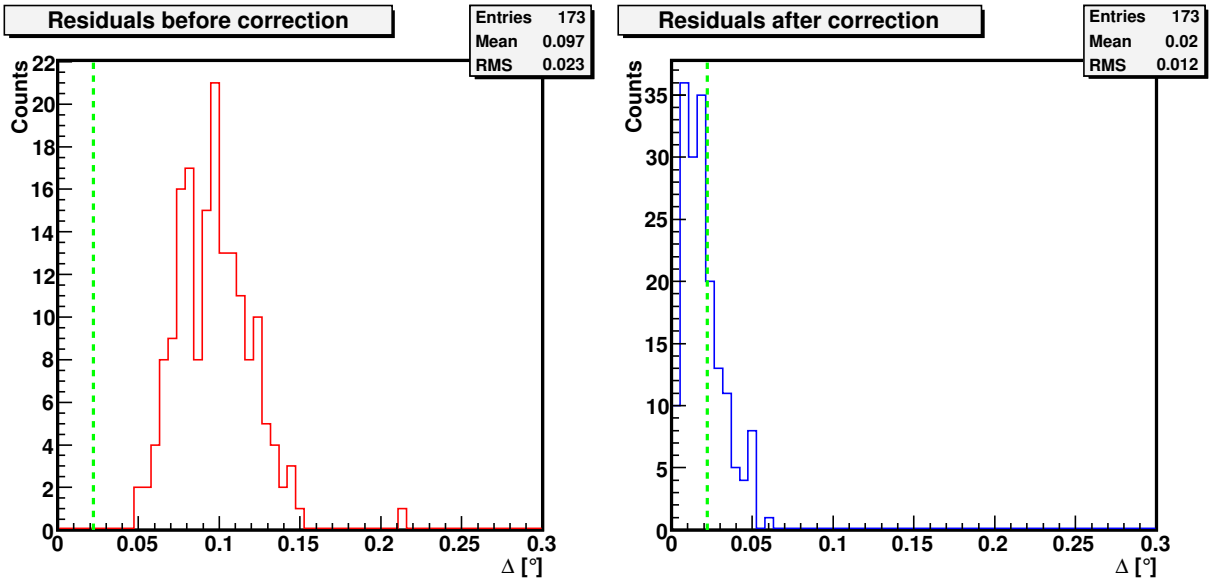

Figure 2.5.: Absolute residuals before (left: red) and after (right: blue) applying the pointing correction. The dashed green line corresponds to one shaftencoder unit. It can be seen, that due to the sophisticated tracking algorithm the mean residual is well below the shaftencoder resolution.

Measurement Period	Number of Datasets	Estimated Systematic Tracking Uncertainty
2004/08	27	$0.015° \pm 0.012°$
2004/09	50	$0.035° \pm 0.026°$
2004/11	62	$0.064° \pm 0.058°$
2005/03	29	$0.032° \pm 0.019°$
2005/04	19	$0.059° \pm 0.025°$
2005/05-1	24	$0.069° \pm 0.038°$
2005/05-2	30	$0.031° \pm 0.028°$
2005/06	26	$0.067° \pm 0.038°$
2005/08	160	$0.044° \pm 0.037°$
2005/09	18	$0.035° \pm 0.018°$
2005/11	139	$0.033° \pm 0.031°$
2005/12	31	$0.019° \pm 0.021°$
2006/01	8	$0.023° \pm 0.010°$
2006/03	394	$0.036° \pm 0.025°$

Table 2.1.: The measurement period, the number of valid datasets taken and an estimate of the average systematic tracking uncertainty with its spread compiled from direct measurements of the tracking accuracy.

2.2. Starguiding system

Unlike optical astronomy, gamma-ray sources are typically too dim in the optical to be used for centering and monitoring the source position. Guiding Cherenkov telescopes therefore relies on the measurement of surrounding stars with their well-known sky positions. A low-prize, off-the-shelf video camera was attached to the center of the main dish of the telescope, monitoring several LED mounted on the PMT-camera frame and stars from the celestial background.

The CCD-camera features a very high sensitivity of 0.0003 lux at the cost of a poor signal to noise ratio. By averaging over 125 frames, corresponding to five seconds integration time, the high noise level can be reduced and full use of the high sensitivity can be made. Example for pictures taken with the camera can be found in Riegel et al., 2005.

In the display monitor with 460×460 pixels (6.6°×6.6°) typically 30-50 stars are visible with a limiting magnitude of 8.6. The brightest ten to thirty with typical magnitudes brighter than 7.2 are readily recognized.

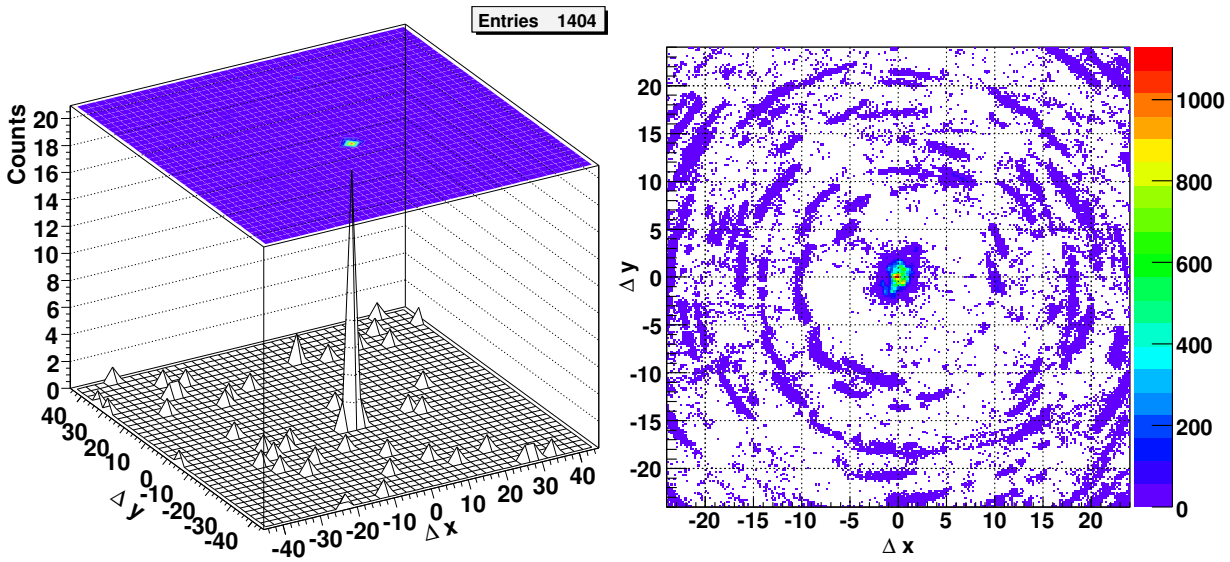

Figure 2.6.: $\Delta x/\Delta y$ distribution for the differences between each star of the nominal star field and each measured star position for a single image (left) and for ∼4000 images of two typical observation nights (right) with each individual image corrected for the determined mispointing position. The peculiar structure around the center is due to single stars moving. The units are CCD-pixels, one corresponding to ∼52″.

By comparing the star field around the pointing position and the cataloged stars the mispointing is determined. This is done by calculating the translation between the nominal star field calculated from the catalog and the measured image. For this purpose a two-dimensional histogram ($\Delta x/\Delta y$) is filled with the differences between the catalog position of each star to all measured star positions. Because of the randomness of the $\Delta x/\Delta y$-distribution for uncorrelated data points a clear maximum can be identified, cf. figure 2.6 (left). The maximum in the histogram

characterizes the mispointing $\Delta x_0/\Delta y_0$ of the telescope.

If the maximum in the histogram is not unique the image is omitted. To account for maxima, misaligned with the binning, the center of gravity of a region around the maximum including the maximum bin and its surrounding bins is calculated. To further improve the calculation, in a second step, the center of gravity is recalculated from all differences withing $3.4\,\sigma$ around the previously calculated center of gravity. Here σ is the width of the statistical spread of the differences for correctly correlated stars. This step is repeated for a cut of $1.7\,\sigma$. Finally roughly seven to thirty stars can be correlated successfully depending on the star-field.

The binning of the histogram has been chosen such, that the size of one square bin matches the area which gives the best background suppression, i.e. a circle with radius $\sim 1.7\sigma$. The width σ of the Gaussian distribution is determined by filling the differences calculated for many images into a single histogram with each image shifted to the mispointing $\Delta x_0/\Delta y_0$ determined. Such a histogram compiled from two typical observation nights ($53803.0 < \mathrm{MJD} < 53804.3$), corresponding to roughly 4000 images, is shown in figure 2.6 (right). It yields a width of the distribution of $\sigma \simeq 0.8\,\mathrm{pixel}$, which corresponds to $\sim 41''$, and consequently a bin-width of $1.7 \cdot \sqrt{\pi} \cdot 41'' \simeq 2.1'$.

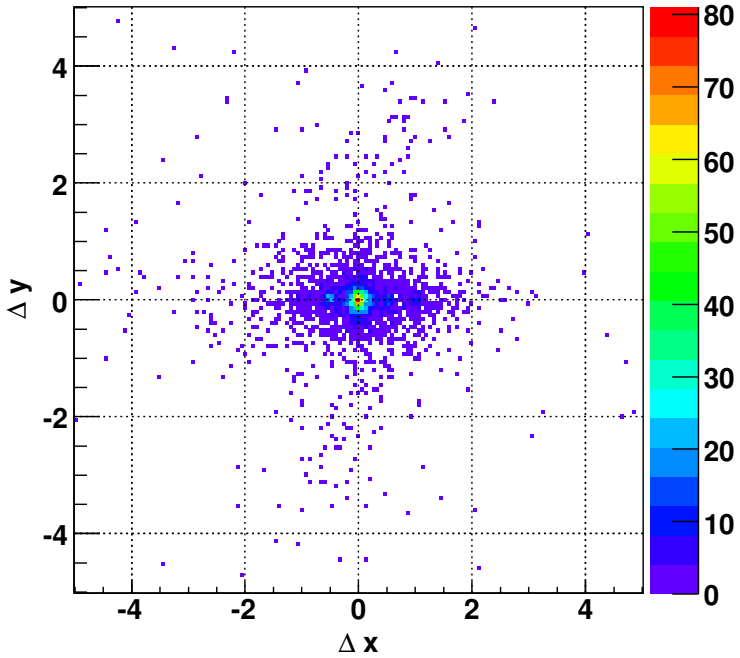

Figure 2.7.: $\Delta x/\Delta y$ distribution for the mispointing calculated from each image compared to the average of the previous and following one. The units are CCD-pixels, one corresponding to $\sim 52''$.

To determine the accuracy of the mispointing measurement each mispointing position is compared to the average of the previous and following one. Assuming that the mispointing does not change much from one frame to the next one, this gives a first order approximation of the accuracy. The result in the $\Delta x/\Delta y$-plane is shown in figure 2.7. Fitting a Gaussian to the distribution

yields a statistical accuracy of $\sigma \simeq 8''$, assuming that the deviation from the Gaussian further out $\sim 20''$ is due to changes in the mispointing with a time-scale in the order of or faster than image acquisition.

Correlating also the magnitudes of the stars with the apparent brightness in the image the algorithm can be improved further. The mispointing is reported to the run control system for on-site inspection and is recorded to the data-stream.

An absolute calibration of the starguiding system can be done similar to the calibration of the tracking system and is currently under investigation. It yields an average systematic accuracy in the same order than for the tracking system.

2.3. Data acquisition

The MAGIC-telescope aims to study the gamma ray emission from high energy phenomena and violent physics processes in the universe at the lowest energy threshold possible (Albert et al., 2005) with present IACT.

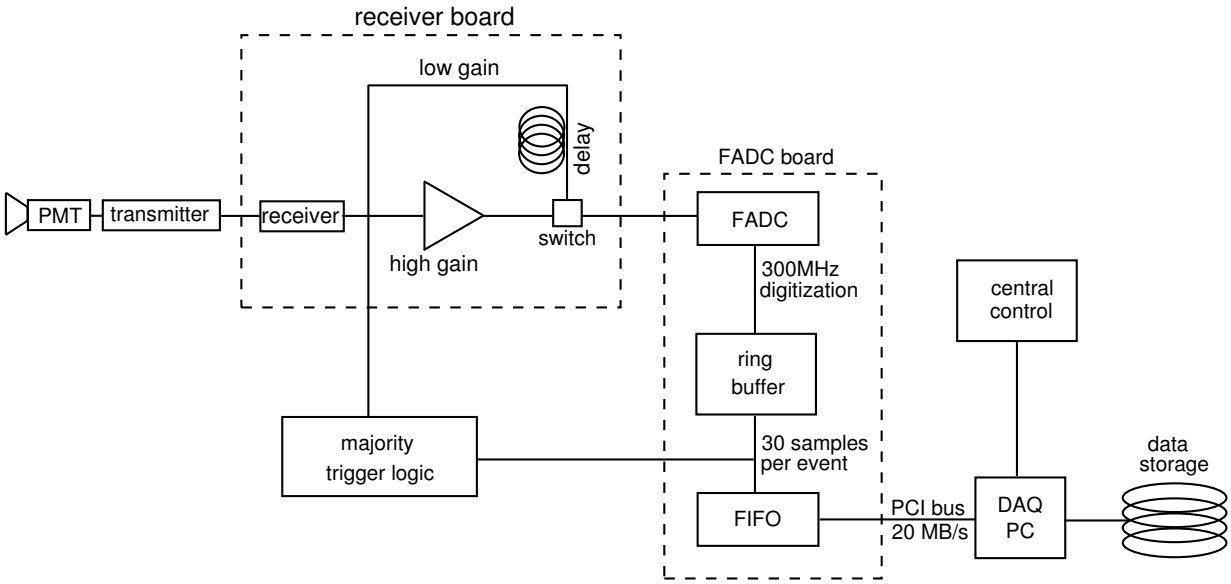

Figure 2.8.: Current MAGIC read-out scheme: the analog PMT signals are transferred via an analog optical link to the counting house where – after the trigger decision – the signals are digitized by a 300 MHz FADC system and written to the hard disk of a data acquisition PC.

Figure 2.8 shows a sketch of the MAGIC read-out scheme, including the camera made of 577 photomultiplier tubes (PMT), the analog-optical link, the majority trigger logic and flash analog-to-digital converters (FADC). The used PMT provide a very fast response to the input light signal. For sub-nanosecond input light pulses it shows a FWHM of 1.0 ns to 1.2 ns with rise times of 600 ps and fall times of 700 ps. By modulating vertical-cavity surface-emitting laser (VCSEL)

type laser diodes in amplitude, the fast analog signals from the PMT are transferred via 162 m long, 125 μm diameter optical fibers to the counting house. After transforming the light back to an electrical signal, the original PMT pulse has a FWHM of about 2.2 ns and rise and fall times of about 1 ns.

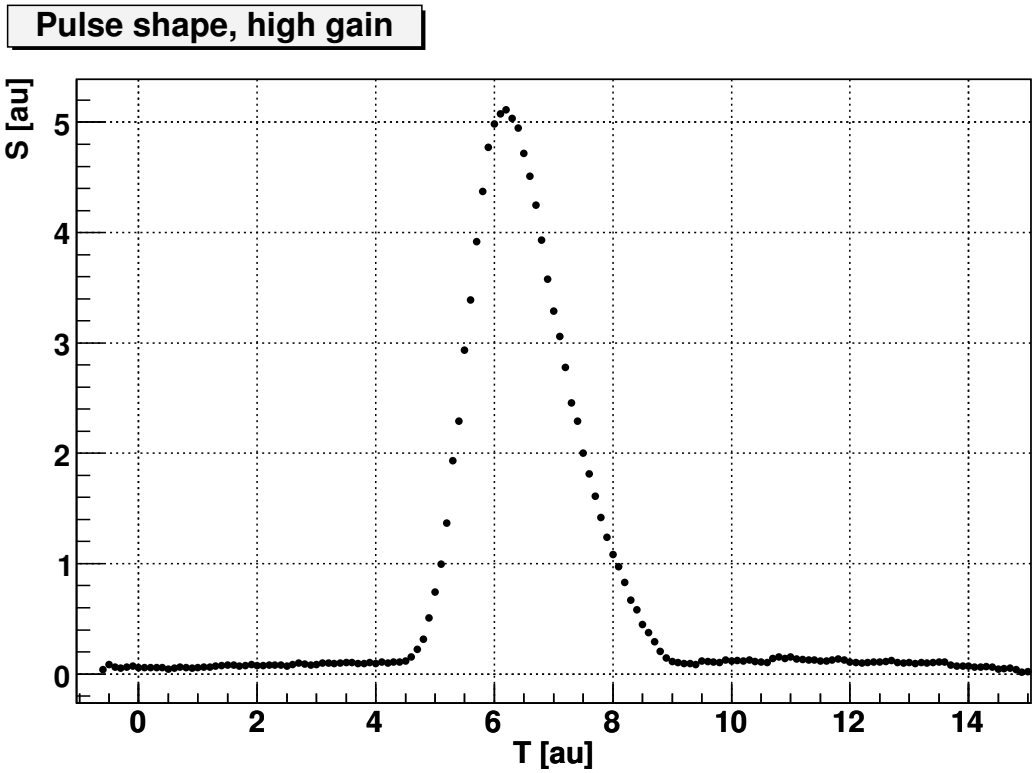

Figure 2.9.: Pulse shape of high gain pulse for cosmic events.

In order to sample this pulse shape with the 300 MHz FADC system, the original pulse is folded with a stretching function of 6 ns leading to a FWHM greater than 6 ns. As the MAGIC FADC have a resolution of 8 bit only, the signals are split into two branches with gains differing by a factor ten. One branch is delayed by 55 ns and then both branches are multiplexed and consecutively read-out by one FADC. For each trigger 15 time slices per branch are read out and recorded. Figure 2.9 shows a typical average of identical high gain signals.

Reading out the full camera, the DAQ has to cope with the data from 577 pixels delivering 30 time slices with 1 Byte each. This yields an event size of $\sim$17 kiB corresponds to a total storage rate of more than 17 GiB per hour proceeding on the assumption of a trigger rate of 300 Hz. Even if todays industrial hardware can handle such data rates, the subsequent analysis software and the executing hardware must be well prepared to be able to analyze the data in time. The complexity of modern analysis techniques demands a stable, flexible, easy maintainable and user friendly software framework.

3. Software Framework

. . . it is simplicity that is difficult to make.
— Berthold Brecht.

For the large amount of data delivered by the current generation of Cherenkov telescopes an improved concept for handling their data had to be developed.

3.1. Requirements

Such a framework, unknown from previous IACT experiments, was essential to keep pace with the constantly increasing data-rates allowing lower thresholds and higher sensitivities. To ensure that changing observation conditions are taken into account and the data is analyzed close to its recording an automatic data processing without human interaction is mandatory.

For this aim a framework which allows easy development and implementation of new analysis techniques and algorithms is essential. To support the development a collection of tools for debugging and for quick-look data access was programmed. An interface for easy setting up any analysis by a macro language or changing parameters and algorithms inside a well defined analysis task had been developed, allowing easy automation of the analysis.

A unified data-processing scheme is also part of the concept to allow a simple restructuring of the analysis chain. This scheme also allows synchronization of several independent data stream as delivered by different asynchronous subsystems.

It could be shown, that by omitting execution of as many conditionals as possible and using the advanced techniques of todays programming languages a framework could be developed which does not slow down a running analysis too much by keeping the executed code-overhead at runtime low.

Keeping the setup of the analysis chain as flexible as possible the framework allows to implement future, e.g. hardware, changes or extensions easily. This allows a simple adaption of the existing analysis algorithms to future experiments. For an IACT analysis this is achieved by the possibility of exchanging the camera and mirror geometry without further software changes.

A crucial point in many event based analysis environments is the development of background suppression methods. Allowing an easy implementation of new methods and exchange of the existing ones, fast test and application of them becomes possible. If this is achieved by the framework and the need for individual programs for each algorithm can be abandoned. Instead parts of the programs, e.g. background suppression, can be exchanged at runtime (Plug-ins).

In the case of IACT analysis the benefit is the simplification of implementation and testing new algorithms for image parameter calculation and background suppression.

Therefore basic layers implementing the foundation for any analysis must be made such, that any further implementation of specialized analysis algorithms do not need to influence lower layers.

3.2. Implementation

Brillante Ideen sind organisierbar.
— Julius Robert Oppenheimer, 1904-1967.

As for this kind of implementation an object oriented approach was practical, it was implemented on top of C++ and CERN's analysis package root (www-10). For the precise implementation a multi layer approach was chosen as shown in figure 3.1.

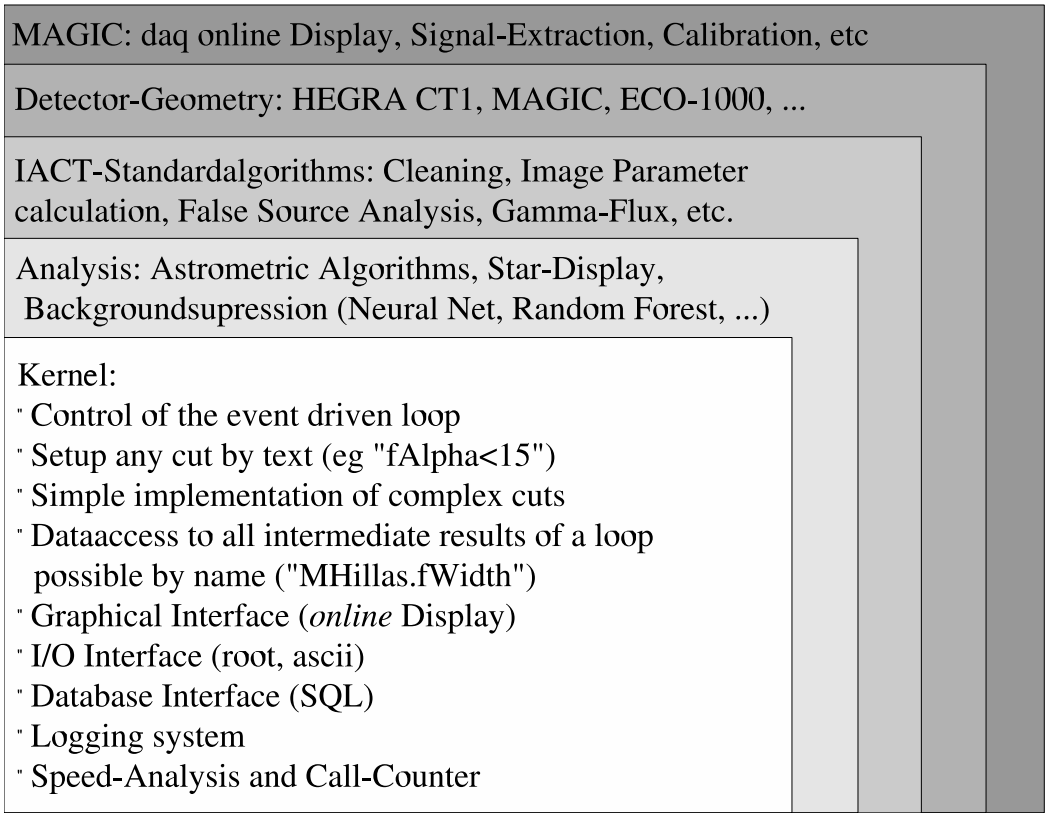

Figure 3.1.: A sketch of the multi layer architecture of the MAGIC Analysis and Reconstruction Software framework. More details can be found in section 3.2.

In the following the single layers are described in more detail. A basic knowledge of object oriented programming is mandatory. A more detailed documentation automatically created from the program sources is available at (www-11).

3.2.1. Layer 0: Kernel

The main and most important part of the package is the architecture of the Kernel, which serves as an interface between the automatic run-control, the input/output (I/O) and the user. Its complete independence of the final analysis task executed allows the package to be used in wide range of different experiments and environments.

While the most basic part of the package can be assumed a collection of several development tools, the eventloop described in the following is mainly useful for event based applications.

Eventloop

The main part of the Kernel is the so called Eventloop[1]. An eventloop is the interface between the data, the algorithms and the user. Data members (e.g. numbers) are typically stored in special structures (classes called *parameter containers*) and collected in a list[2]. Algorithms processing these data are called *tasks*[3]. To compile a full analysis (called *job*) several tasks are collected and ordered in a tasklist[4]. The eventloop takes care of processing such a job.

For each task a basic interface was defined in the common base class of all tasks, MTask, which is made out of four parts, which will now be described in detail:

Before the data processing is started, the **PreProcess** function of all tasks is executed in the same order as data processing takes place. In this step the connection between the data and the algorithms is established through the parameter list; the user setup can be converted and processing time saving precalculation can be performed.

For reexecution some of the calculations done in the preprocessing step a **ReInit** function is called on demand by the executed tasks. This normally happens, if in a chain of files to be processed a new file is opened and after the new file-headers have been read. ReInit is done for all tasks in the same order than the data is processed. However the precise context in which ReInit is executed may depend on the calling task. In principal each task can trigger the ReInit process.

The main step in data processing is the treatment of the data itself, which takes place in the **Process** function. The Process of all tasks is executed in the order defined in the tasklist. Whether a task is executed or not is controlled by filters[5], which allow the implementation of any cut as complex as necessary. This Processing step is repeated until it is stopped by any task.

When the data processing has been completed, a **PostProcess** function is executed. This step allows memory clean-up, the calculation of final results and storage of results. Also the last step is executed in the same order than all previous steps.

After making the eventloop aware of the necessary parameters and task list, it takes care of executing this structure correctly. In addition it provides an interface to a logging facility[6], a run

[1] class MEvtLoop
[2] a class called MParList
[3] Based on the class MTask
[4] class MTaskList
[5] Based on class MFilter
[6] class MLog

display[7] and offers the user a statistical analysis of the accumulated run time of all tasks and a call counter.

As tasklists are tasks themselves, both are parameter containers by construction. This offers a wide range of powerful capabilities especially for debugging.

This flexible structure allows to setup almost any event based jobs and is not only suitable to analyze data taken by an experiment, but can also produce and process simulated data.

Logging facility

The handle to the logging stream is automatically distributed to all tasks and parameter containers available, when an eventloop is invoked. The logging stream is based on the C++ streaming classes and offers the possibility of synchronous redirection of the stream to different outputs (e.g. console, file, graphical user interface, HTML, etc.). It provides several debug levels of text output which are indicated by different output colors. The user can control the output by defining the output level. An example is shown in figure 3.2.

Status Display

In addition to the logging stream a handle to a status display is distributed automatically. In many circumstances it is useful to be able to monitor the result of a running job at run time. This tool offers the possibility to recognize errors and problems in the analysis as early as possible. Especially developing of new tools can thus be simplified and accelerated. The contents of the display can be stored in various file formats[8]. Its storage in the proprietary format of the root package allows to fully restore the contents of the display and its full functionality (e.g. zooming into a plot). This feature can be used to create a lot of data check and control plots simultaneously running the automatic data analysis. An example is shown in figure 3.3.

Setup of a job

If a job is well defined and has been established, it becomes more and more important to compile a running, simple to use, program out of it. In this case it is convenient, if the full setup can be done from a setup/resource file[9]. Before an eventloop is invoked by this program or the user, the contents of a resource file can be distributed to all parameter containers and tasks collected in the corresponding lists. This offers the possibility to make any parameter modifiable.

Furthermore, implementing corresponding generalized tasks[10] and filters allow a high level of control of the executed job. It makes it even possible to exchange algorithms embedded in a task, for which it was foreseen by the author, completely at run-time with a new algorithm. In such an environment the surrounding program structure can stay exactly the same while single algorithms (e.g. for background suppression) can be replaced easily.

[7] class MStatusDisplay
[8] as root, gif, png, eps, ps, pdf, jpg, xpm and root-macro
[9] Implemented by an interface to class TEnv
[10] class MTaskEnv

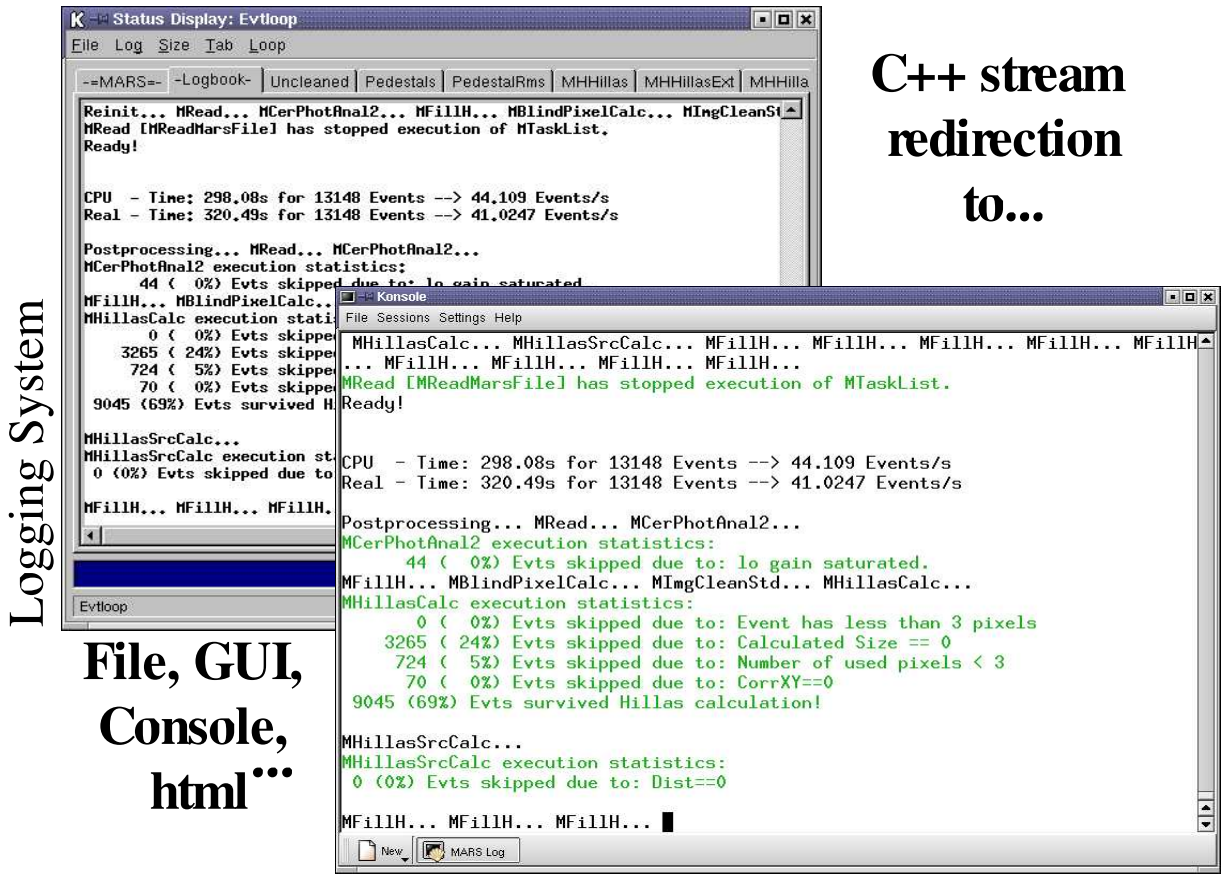

Figure 3.2.: Example of a the logging stream. Left: Logging stream redirected to a graphical user interface. Right: Colored logging stream displayed in the console window. Black output is output always shown, the green color means a informal output which might be suppressed. Orange would correspond to a warning about a possible problem, red would mark a fatal error resulting in a program abort.

Example

An example of an eventloop is sketched in figure 3.4. In a first step the user has to define the job to be done. Therefore the necessary tasks are instantiated and placed in the tasklist. In this example we assume that the first task (Read data) will read events from a file. The second task (Algorithm 1) calculates a correction of this data based on *read data* and a setup container stored by the user. A third task (Algorithm 2) fills a histogram from this data, which is stored by the fourth task (Write data). After the user has setup the eventloop, setup files can be distributed to each task changing their behavior. When the eventloop is invoked, the preprocessing is executed for all tasks which may open the files, create the histograms, etc. After it the tasks Process the data as long as data is available or an error occurs. The histogram filled by the tasks is displayed on-line. After the processing loop has finished, the postprocessing is started, which might close the file, fit the histogram, etc.

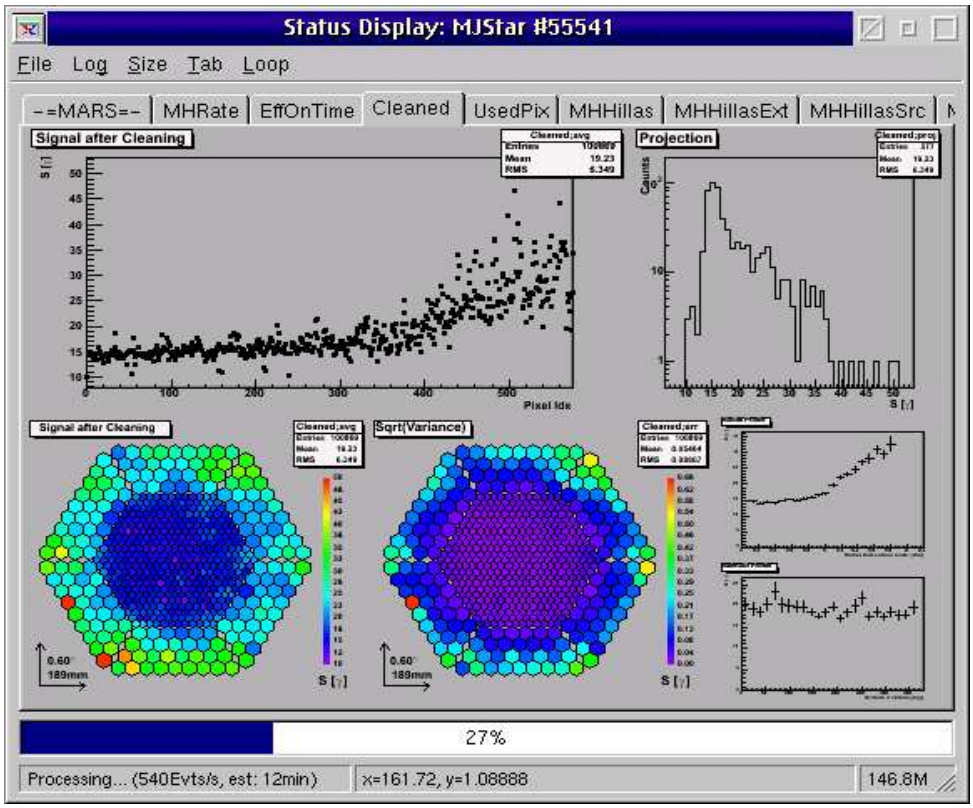

Figure 3.3.: Example of a status display. It shows the mean signal surviving image cleaning after processing 27% of the data of Sequence No. 55541.

Eventloop tools for development, debugging and run time

Also a lot of tools are part of the kernel simplifying the development, debugging and implementation of new analysis methods. The following description will list the most important ones:

MPrint: Task calling the Print member function of a parameter container in its Process allowing to monitor the contents of a container event by event.

MContinue: Task to signal the eventloop to skip all pending task and start a new processing step. In association with a filter it is a powerful instrument to control the task execution.

MClone: Task cloning an object which might be changed by the following tasks. This allows storing an intermediate result permanently.

MF: A generalized filter which can be setup by a text string (e.g. ”MHillas.fWidth<0.5“). Being able to access almost any intermediate result in a filter, which in addition can be setup from outside, offers the possibility to implement very flexible programs.

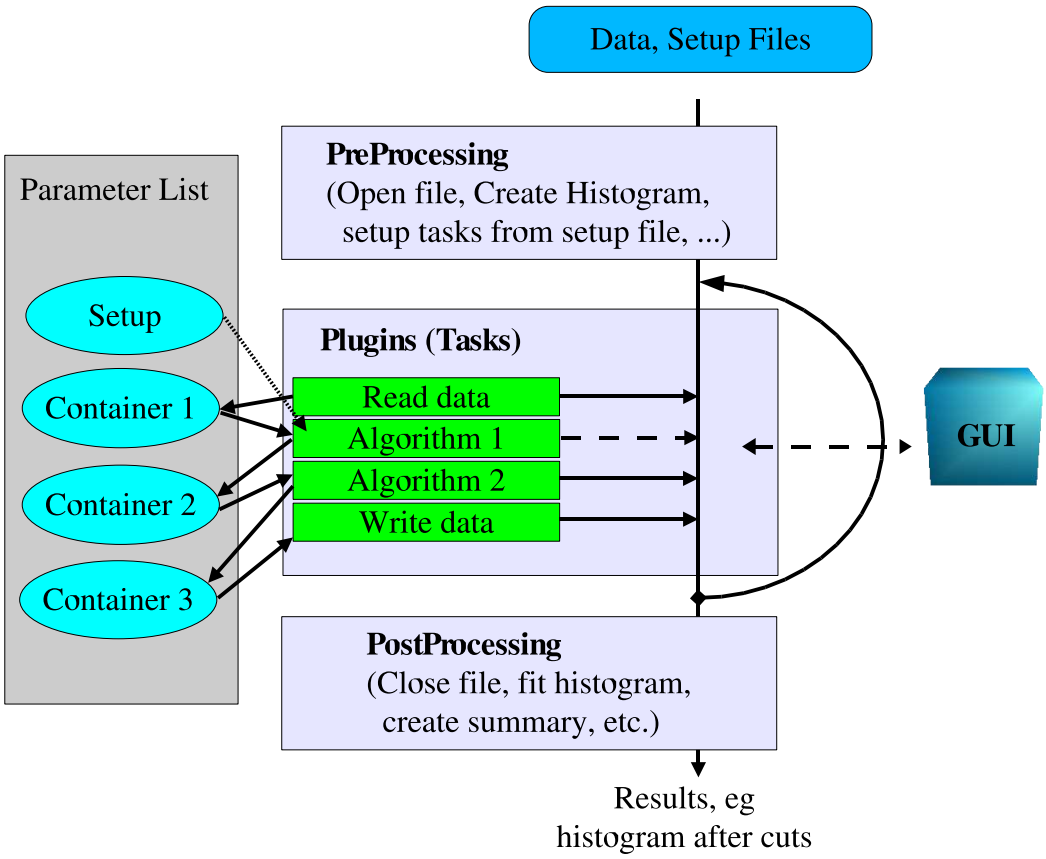

Figure 3.4.: An example of an eventloop. It is described in details in section 3.2.1.

MMatrixLoop: This task was especially designed for optimization jobs. Instead of reading the data on which the optimization should be based from a file, it is directly accessed in memory, accelerating the optimization a lot.

MParameterCalc: This task allows to perform calculations based on intermediate results kept in other containers. The algorithm to be evaluated is configured by a text string as done in MF, e.g. "MHillas.fWidth*MHillas.fLength". This way of setup offers a high level of flexibility in parameterizing any quantity (e.g. reconstruct the energy of an event from its image parameters), especially due to the possibility to be configured from outside precompiled programs as from resource files.

MFillH, MH: Task to fill histograms[11] based on a generalized histogram class[12]. Its main duty is the interfacing to the display, especially important for histograms.

MH3: A generalized histogram capable of accessing any intermediate result. This offers the

[11] class MFillH
[12] class MH

possibility of doing a lot of analysis jobs in one loop and is a powerful debugging tool for a quick-look into the data. It is setup by text string for as many axis as necessary.

MHVsTime: A generalized graph showing the evolution of any intermediate result either versus an existing time stamp or its event number. It is setup by text strings, too.

MHMatrix: A matrix object implemented as histogram class filled by MFillH. It offers the possibility to store a lot of data in memory for fast access mainly in optimization jobs. The columns are described by text string as for MParameterCalc.

MReadTree: Task to read all contents from a tree in one or more root files event by event. All necessary parameter container are created and linked automatically.

MReadMarsFile: Task to read all contents from a tree in one or more root files event by event. In addition a run headers tree is evaluated any time a new file is opened. All necessary parameter container are created and linked automatically.

MReadReports: Task to read all contents of more than one tree from one or more root files event by event. The reading of the different trees is synchronized by a time stamp stored for each event. In addition a run headers tree is evaluated any time a new file is opened. All necessary parameter container are created and linked automatically.

MWriteRootFile: Task to write any parameter container event by event into a tree. A tree entry is only written, if at least one container is flagged to be stored.

Environment tools

In addition to the eventloop based tools there are a lot of environmental tools as:

MMath: A collection of mathematical algorithms such as calculations of significance.

MDirIter: A class for easy access of files by wildcards.

MProgressBar: A simple progress bar to show the progress of an eventloop graphically without the overhead of the full display.

MTime: A general high precision time stamp for a lot of different purposes.

MAstro: An implementation of length scales and conversion routines used in astronomy.

3.2.2. Layer 1: Analysis Methods, Tools

Layer 1 implements several general analysis methods useful in principal for a couple of experiments. These are mainly background suppression algorithms, for example statistical learning methods as Neural Nets, Random Forest or Composite Probabilities. In addition a lot of astronomy tools are provided, which includes coordinate transformation and a display for the contents of a star catalog with grid line for sky and local coordinates. An example is shown in figure 3.5

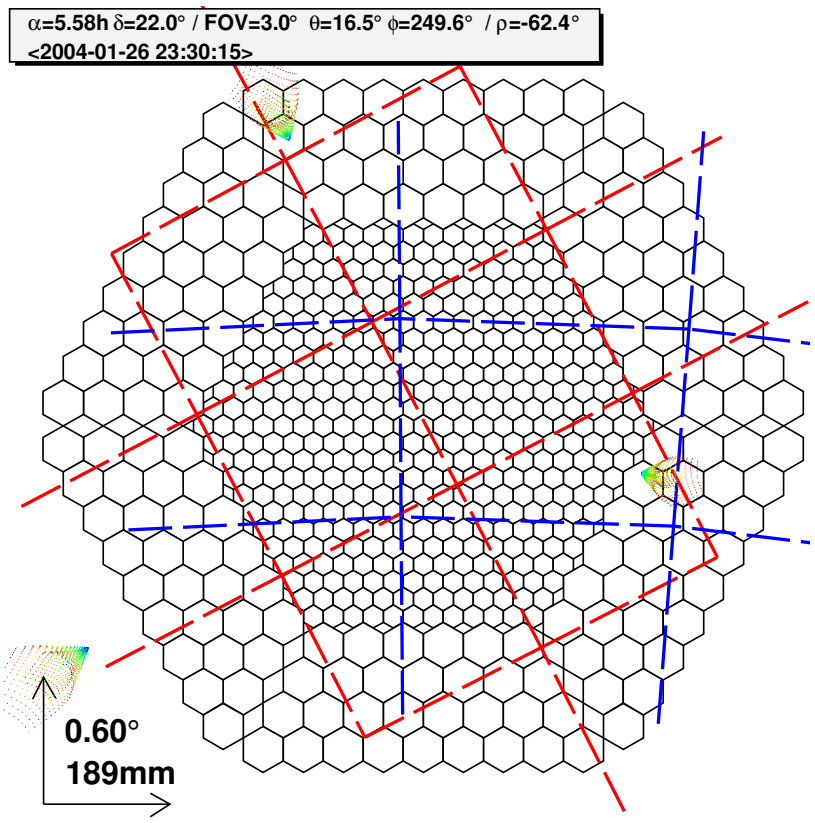

Figure 3.5.: Example for displaying stars in the camera. Here the star catalog is super-positioned on the camera. The colored dots represent the position of the reflection of all individual mirrors, while the reflection of the inner mirrors is coded in blue and the outer mirrors in red. The Crab starfield is shown, the blue lines correspond to the local coordinate system, the red lines to the celestial grid.

3.2.3. Layer 2: IACT standard algorithms

On top of this data structures, histograms and algorithms are implemented which are especially useful in Cherenkov astronomy. This includes well known analysis techniques as image cleaning, noise suppression in the recorded images due to night sky background light; the calculation of image parameters, including the momenta of the light distribution, Hillas parameters (Hillas, 1983), and newly developed parameters; a software trigger suppressing images triggered due to accidental coincidences; algorithms for false source analysis and gamma flux determination.

All this algorithms are designed to be independent of the detector geometry, e.g. the camera pixel layout in the case of image parameters.

Different analysis techniques for background suppression (e.g. classical parameter cuts, statistical learning methods), signal determination (e.g. α-plot, ϑ^2-plot), false source methods (e.g. based on α or Disp), observation mode (e.g. on/off, wobble) and energy reconstruction methods (e.g. classical formulas, statistical learning methods) could be implemented as Plug-ins. Plug-

ins are algorithms with a unified interface, traced back to a single base-class. This technology allows unified programs taking care of the whole analysis which are independent of the precise algorithms used. The advantages are easy implementation of new algorithms and the certainty that the remaining parts of the analysis remain untouched.

3.2.4. Layer 3: Detector Geometry

To adapt the general IACT analysis, implemented in Layer 2, to a precise detector, information specific to it has to be implemented in Layer 3. For IACT analysis this mainly concerns the camera geometry (pixel layout and distance to mirror) and the mirror geometry. Examples for different implemented camera geometries are shown in figure 3.6. By exchanging the geometry container the full analysis can immediately be used another detector.

3.2.5. Layer 4: MAGIC specific part

In addition to the adaption to a specific class of experiments, parts of the analysis software must be specialized for the telescope. In the case of the MAGIC-telescope this concerns the data calibration which is adapted well to the read out electronics. These algorithms can not be used easily for other detectors.

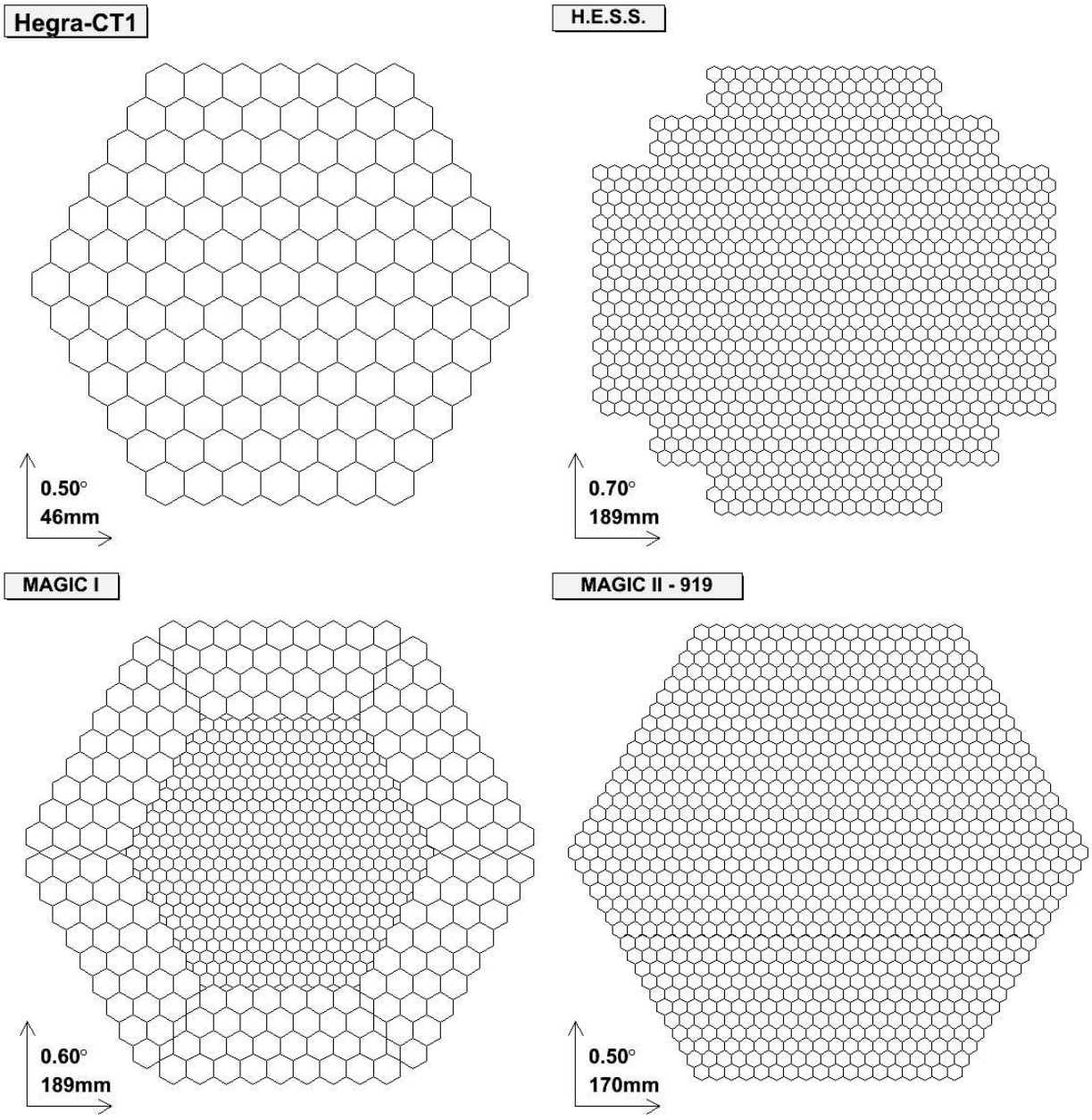

Figure 3.6.: Examples of different camera geometries already implemented in MARS. The HEGRA CT1 geometry (Mirzoyan et al., 1994) has been used extensively in the development phase of most of the algorithms. The MAGIC geometry is currently the base of the data analysis for the MAGIC-telescope. The MAGIC II geometry is currently under investigation as a possible geometry for the future MAGIC II experiment. And the H.E.S.S. geometry (Aharonian et al., 2004a) is implemented to show the flexibility of the package.

4. Analysis

Die Physik ist ihrem Wesen nach eine
konkrete und anschauliche Wissenschaft.
Die Mathematik gibt uns nur die Mittel
in die Hand, um die Gesetze auszudrücken,
wonach die Erscheinungen sich vollziehen.
— Albert Einstein.

The following chapter will describe the analysis algorithms in more detail, which are mainly implemented in Layer 2 (see also Bretz, 2005). They are also used for the presented analysis and obtained results. Everything is based on the previously described and developed analysis package. The calibration discussed hereafter belongs to the MAGIC specific part (Layer 4), the MAGIC-geometry is given by the detector setup (Layer 3). All other algorithms implemented are of general use and belong to Layer 1, e.g. Random Forest, and to Layer 2, e.g. Image Cleaning.

4.1. Calibration

The intention of the calibration is to convert the measured FADC signal into an absolute number of photo electrons (units phe) produced by the photo-effect inside the PMT. Therefore a signal must be extracted from the high- and low-gain branch of the electronics chain. Both must be compiled together and converted correctly into absolute units. A more detailed description of the calibration can be found in Gaug et al. (2005) and Doro (2004).

The time evolution of the conversion factor over the whole observation time up to now is shown in figure 4.1. The two different levels originate from two different extraction methods chosen.

For the data, which analysis is discussed in more details later, the conversion factor remained stable and agrees well within the statistical error as shown in table 4.1.

	Conversion factor	
	Inner Pixels	Outer pixels
on-data	0.354 ± 0.005	1.48 ± 0.08
off-data	0.349 ± 0.008	1.44 ± 0.06

Table 4.1.: The mean conversion factor for analyzed on- and off-data agree well within the statistical and systematic errors.

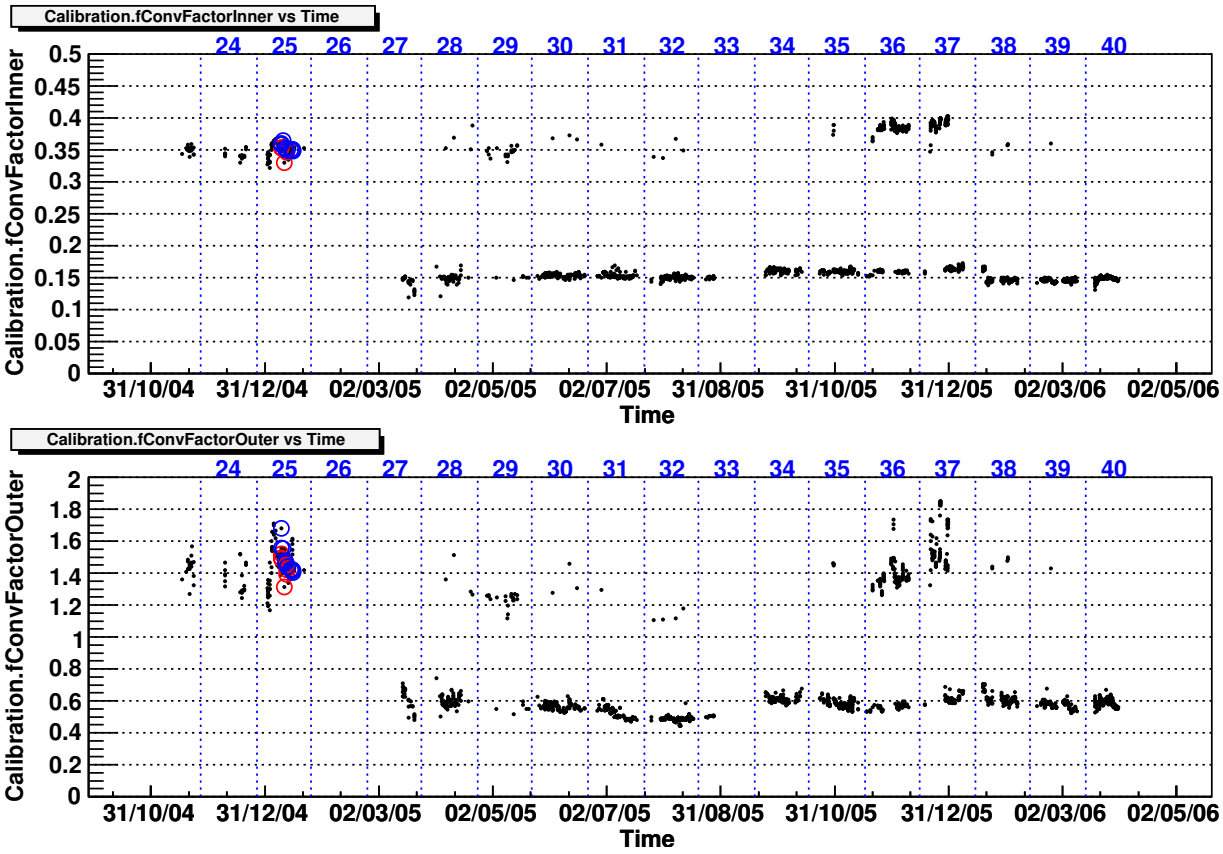

Figure 4.1.: Time evolution of the mean conversion factor of the small (top) and large pixels (bottom). Different levels are due to different extraction methods. The blue numbers above correspond to the observation periods. One black dot corresponds to one observation sequence. Data of 1ES 1218+304 is marked with blue (on-data) and red (off-data) circles.

4.1.1. Signal Extraction

The signal is reconstructed in a fixed window smaller than the full digitized information. Decreasing the window size further allows better noise suppression, because less background fluctuations enter the reconstruction algorithm.

The signal and arrival time extraction is done using two different methods a spline-approximation (spline) and a method called *digital filter*.

To extract the signal height from the spline, it is integrated over 1.5 time-slices at its maximum.

The digital filter is an analytical fit to the data assuming that the background autocorrelation and pulse shape of the signal is well known and changes only in amplitude and arrival time. A complete discussion of this method can be found in Bartko et al., 2005.

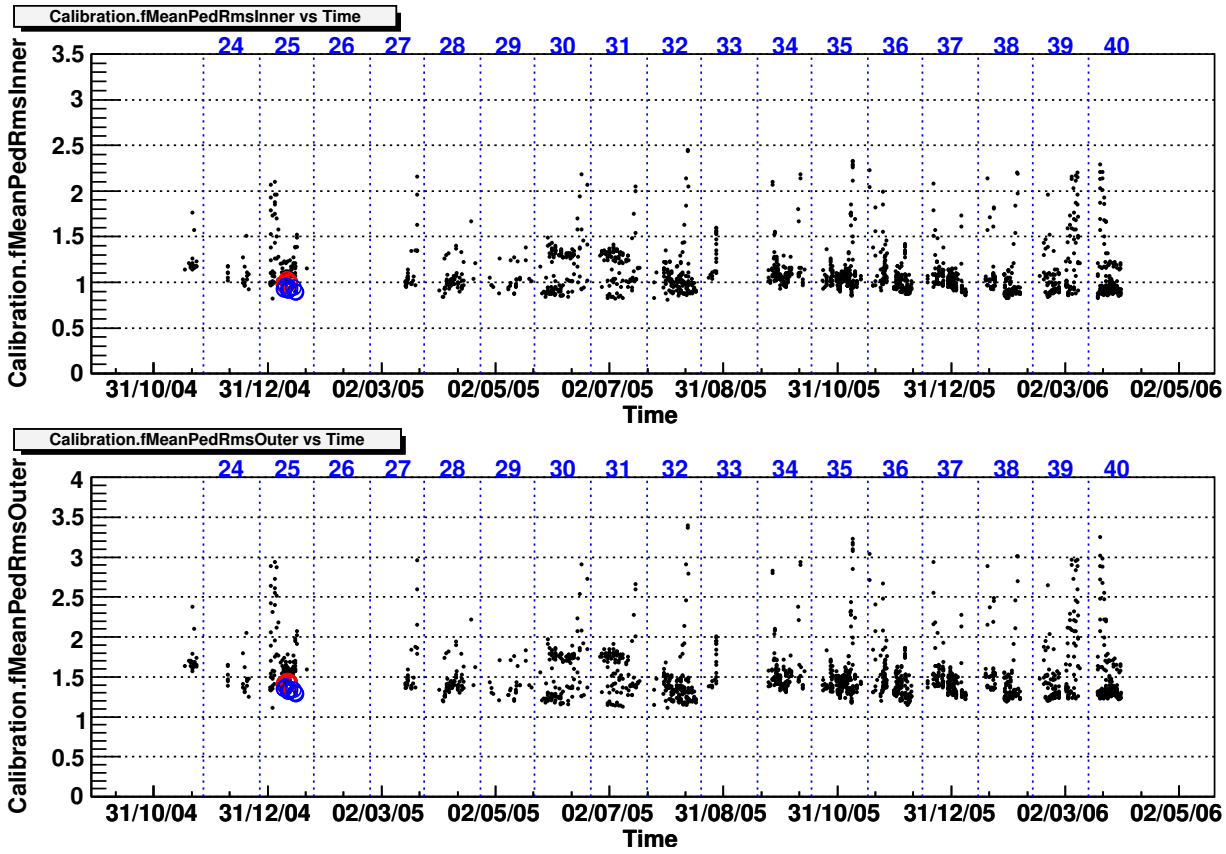

Figure 4.2.: Time evolution of the pedestal fluctuation of the small (top) and large pixels (bottom). Higher values are due to higher background brightness. The blue numbers above correspond to the observation periods. One black dot corresponds to one observation sequence. Data of 1ES 1218+304 is marked with blue (on-data) and red (off-data) circles.

4.1.2. Pedestal Treatment

The pedestal, the offset of the FADC measurement, can be extracted from the low-gain branch of the signal. If the amplitude of the signal is below a certain limit, the high-/low-gain switch is not triggered. As a result the low-gain branch of the signal still contains digitized subsequent high-gain data unbiased by any signal. The pedestal, which will be subtracted from the extracted signal, is now calculated as the average of many pedestals extracted from empty low-gain samples using the same extractor than used for the signal.

If the used extractor is a peak searching extractor like the digital filter, the extracted pedestal would show a bias due to the peak searching characteristic of the algorithm and the pedestal fluctuation might be influenced, too. Therefore the pedestal and its fluctuation are extracted from random samples in the allowed range, if the extraction algorithm is a peak search algorithm. While in this case the pedestal and its fluctuation still describe the measured offset and the sta-

tistical fluctuations of the signal correctly, another special pedestal (bias) is calculated using the peak search capability of the algorithm. This bias and its fluctuation is a measurement for the lowest signal which can be extracted by this algorithm, which is important to separate the signal from the background.

The information of the signal offset and its fluctuation can be used to determine the probability of a measured signal to be a real signal rather than a fluctuation.

Due to the AC-coupling of the PMT the pedestal fluctuation is influenced by the brightness of the diffuse night-sky background. This brightness depends on human light sources as car-light or far away street-lights, but also on natural sources as moon-light and the pointing direction (e.g. star density in the milky-way, zodiacal light, calima). As the probability of a fluctuation to be detected as a signal is directly correlated to the level of fluctuation, the stability of the pedestal fluctuations is mandatory and its level should agree well for all data used in the same analysis.

The time evolution of the pedestal fluctuation for all data taken so far is shown in figure 4.2.

For the data, which analysis is discussed in more detail later, the fluctuation is stable and agrees well for on- and off-data within the statistical error, taking into account that a small difference for different pointing positions on the sky is conclusive. Numbers are given in table 4.2.

	Pedestal fluctuation	
	Inner Pixels	Outer pixels
on-data	0.919 ± 0.021	1.329 ± 0.028
off-data	0.997 ± 0.016	1.422 ± 0.015

Table 4.2.: The mean pedestal fluctuation for analyzed on- and off-data agrees well within the statistical and systematic errors.

4.1.3. Camera Inhomogeneity

Due to hardware problems the readout could not be triggered such, that the main shower signal was always at the readout position. Figure 4.3 shows the mean peak position averaged over all pixels in units of the sampling-slice number (FADC-slice) versus observation date. It can be seen that the peak moves from a value, which is pre-adjusted to $\sim$5 to values well below ($\sim$3) and above ($\sim$10).

To prevent the peak from leaving the signal extraction window an automatic procedure to adjust the window position and the real pulse position is part of the calibration.

It turned out, that for most data the pulse position depends on the part of the camera in which the shower has triggered. Different peak positions from one event to another event, having a too small extraction window, result in losing the part of the signal information which is outside the extraction window. This behavior can be visualized by plotting the root mean square of the pulse position as shown in figure 4.3. By losing part of the shower image because of this effect, showers which only trigger in some part of the camera become smaller. Removing the smallest shower from the analysis, because they do not carry enough information for further

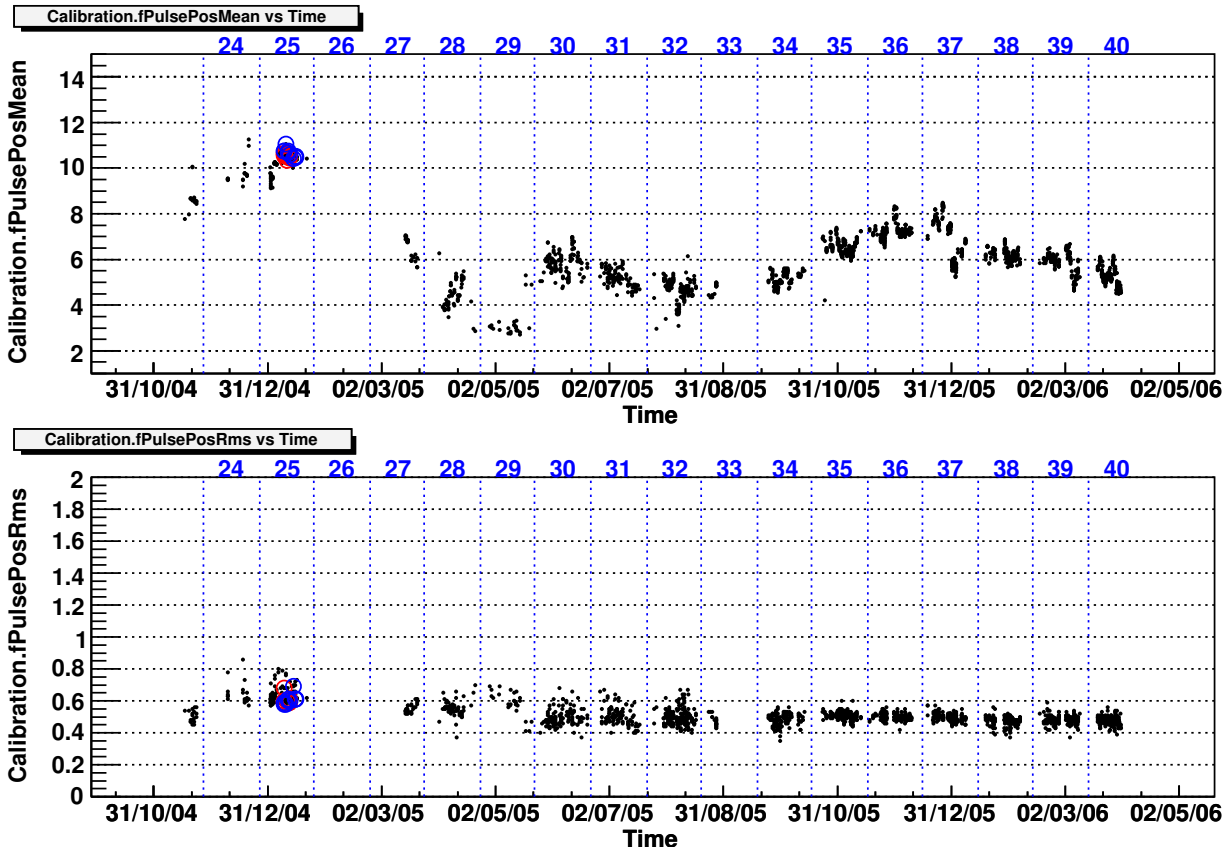

Figure 4.3.: Time evolution of the mean calibrated pulse position and its fluctuation for pulses above 15 phe in units of FADC-slices. The blue numbers above correspond to the observation periods. One black dot corresponds to one observation sequence. Data of 1ES 1218+304 is marked with blue (on-data) and red (off-data) circles.

analysis, the number of showers reconstructed in different parts of the camera is not identical. Consequently the acceptance of the camera becomes inhomogeneous. As this means, that the acceptance in some parts of the camera is smaller as expected, the efficiency of the detector will be overestimated.

To check this effect a new parameter has been included into the analysis called *Inhomogeneity* being the variance of the number of showers reconstructed in the six camera sectors. While in a correctly working environment numbers around and below 10%-15% are typical due to unavoidable fluctuations, some data gave values above 30%. The time evolution of this new parameter is shown in figure 4.4.

To explore this effect a study on the dependence of the Inhomogeneity from the extraction window has been carried out. Adjusting the width of the window to the observation conditions, the Inhomogeneity of most data could be decreased to $\lesssim 15\%$. The time evolution of the Inhomogeneity after adaption of the extraction window is shown in figure 4.4.

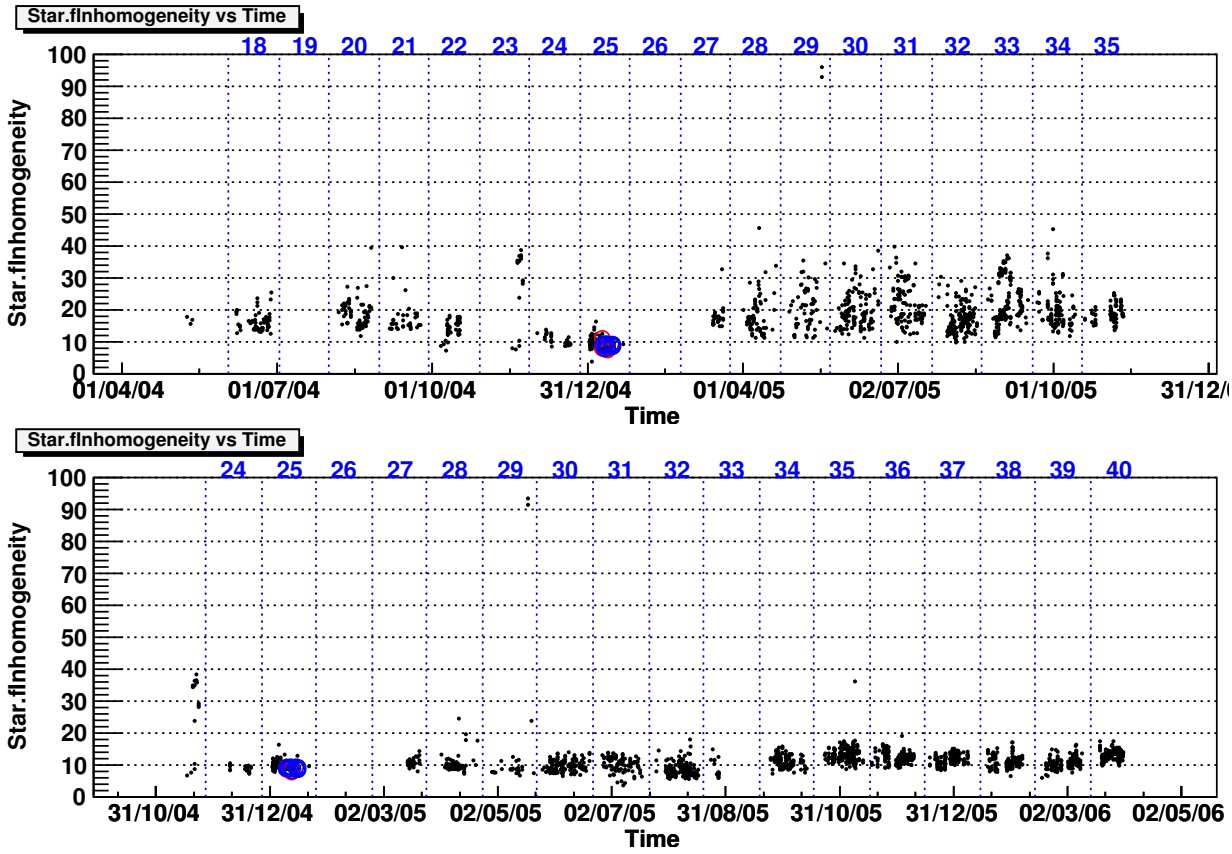

Figure 4.4.: Time evolution of the camera inhomogeneity with the standard calibration setup in arbitrary units, before (top) and after (bottom) enhancement of the extraction window as discussed in the text. The data before period 24 have not been reprocessed. The data of period 35 was the last one processed with the old setup. The blue numbers above correspond to the observation periods. One black dot corresponds to one observation sequence. Data of 1ES 1218+304 is marked with blue (on-data) and red (off-data) circles.

4.2. Bad pixel treatment

Bright stars illuminating PMT in the field-of-view can alter their response leading to an increase of fluctuation of their signal. Owing to the ALT-AZ mount of the MAGIC-telescope, the images of stars rotate across the camera during tracking, and thus the fluctuations affect different pixels.

Values of pixels affected by fluctuations larger than five standard deviations from the average fluctuation are replaced. This also happened for other *bad* pixels, e.g. pixels which could not be calibrated or the missing central pixel. For the substitution the surrounding pixels are interpolated. Due to the fact that peak search signal extractors, as used in the analysis, extract a signal greater than zero, even if no signal is present, simple interpolation will result in the extracted small signals being slightly overestimated. Consequently such pixels would be assigned to showers by mistake too often. To avoid this unintentional behavior an additional algorithm has been implemented correlating the contents of one pixel with its neighbors. With that the probability, that the pixel does contain no signal at all is determined. In this case the content of the bad pixel is replaced by a random number distributed as the mean background fluctuation of pixels of the same size. Typically less than 3% of all pixels are affected. A more detailed description of the algorithm can be found in Rügamer, 2006.

4.3. Artificial triggers

Additionally the used trigger logic might not be calibrated perfectly, which might result in artificial triggers. To understand the artificial triggers in more details the trigger logic will be explained in the following:

4.3.1. Trigger logic

The logic currently used to trigger the detector read out is a three level logic:

Level 0: A simple signal-above-threshold discriminator (in the order of 40 μA) giving a binary signal whether the signal of an individual pixel is above the threshold or not.

Level 1: A logical trigger investigating coincidences of neighboring pixels surviving trigger Level 0. Observations are currently carried out with a four-fold coincidence, demanding four neighboring pixels above threshold in a closed package configuration.

Level 2: A trigger-logic which is programmable (currently not in use)

This trigger logic has several free parameters. The individual trigger rate of a pixel can be controlled by the discriminator threshold. Typically this threshold is similar but not equal for all pixels due to small differences in the performance of the PMT and the electronics chain. For the coincidence trigger a well adjusted delay for each pixel is necessary. This delay is known to be unequal for all pixel due to dissimilar signal runtimes based on small differences in the PMT, the electronics or the cable lengths. On top of this the number of required coincident neighboring pixels can be chosen.

4.3.2. Software trigger

Taking into account that the environment is changing all the time, the performance of the trigger is slightly affected by small variations of gains or delays in the trigger logic. Mainly gain fluctuations and differences in the arrival time, for example because of changing temperatures of the PMT, are responsible for an increased artificial trigger rate due to random coincidences generated by fluctuations induced by the NSB.

After having the signals of all pixels correctly calibrated, i.e. corrected for these small variations, the trigger logic can be rebuild in the software to suppress these artificial coincidences. Therefore a software trigger has been programmed[1] requiring at least four neighboring pixels with a signal above 5 phe and an arrival time inside a coincidence window of ± 0.5 FADC-samples. Only events containing such a cluster survive the software trigger. A study about the precise trigger condition can be found in Höhne, 2005.

The main advantage is, that events which clearly originate in background fluctuations are suppressed early in the analysis. This decreases the further processing time and allows to calculate the trigger-rate of showers unbiased by random coincidences. This rate is a good quality measurement of the atmospheric conditions. A stable rate is mandatory for the successful fit (see section 4.8) determining the effective observation time and is achieved hereby.

4.4. Image Cleaning

As a statistical analysis of the intensity distribution of the shower image is done, the result can be improved taking only signals belonging to the shower into account. For this purpose an algorithm removing noise is applied to the data, called *Image Cleaning*.

There are different image cleaning algorithms available. The most common ones can be unified into a single algorithm[2] if fed with different signal properties as input, so-called cleaning values, e.g. the relative signal-to-noise ratio or the absolute signal.

This algorithm first searches for all pixels with cleaning values above a first cleaning level, hereafter called *core*-pixels. In addition, all pixels above a second cleaning level neighboring a core-pixel, hereafter called *used*-pixels, survive cleaning. Finally, all solitary core-pixels are removed.

If an image cleaning based on the signal-to-noise ratio, called relative image cleaning, would be applied, changing fluctuations would influence the shape of the images. Not to suffer from this an image absolute image cleaning is applied with a first cleaning level of 8.5 phe and second cleaning level of 4.0 phe. A study about the precise cleaning values can be found in Höhne, 2005. An example of the image cleaning for showers from an observation of the Crab Nebula is shown in figure 4.5.

[1] class MFSoftwareTrigger
[2] class MImgCleanStd

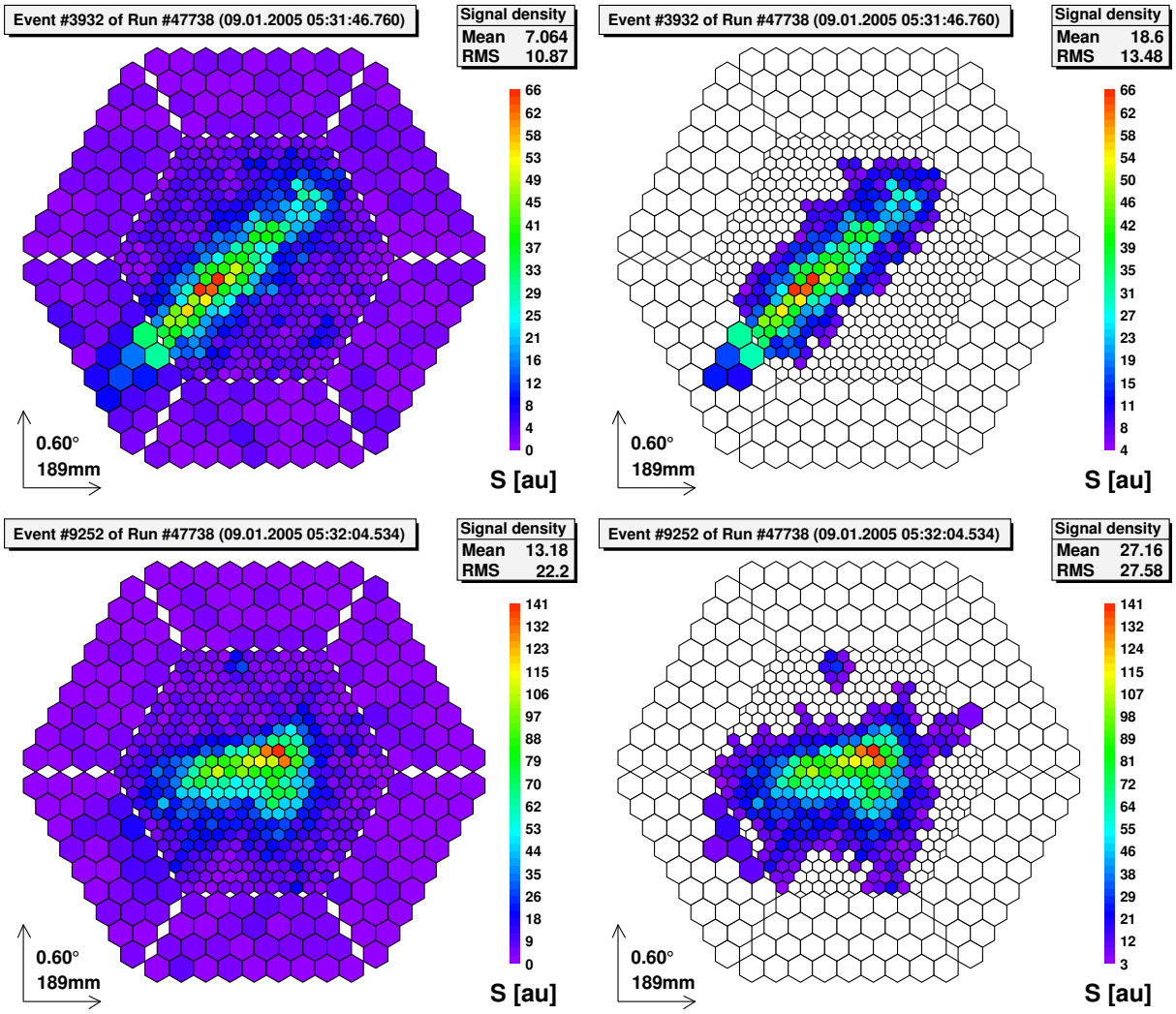

Figure 4.5.: Two events from run 47738 before (left) and after (right) image cleaning. Displayed is the color-coded photo electron density.

4.5. Image Parameters

4.5.1. Classical statistic-parameters

From the intensity distribution of the cleaned image several image parameters[3] are computed as introduced by Hillas (1985):

- center of gravity (COG $< \vec{p} >$)
- standard deviation along the major axis (Length l)
- standard deviation along the minor axis (Width w)
- distance of COG from the position of the target source in the camera (Dist d)
- angle between the major axis of the shower image and the line between COG and the target source position (Alpha, α)
- total number of measured photo electrons in the image (Size S)
- third moment of the distribution along the major axis (m_l)

In addition to these *standard* parameters a lot of quality parameters, discussed in the next section, are computed.

To calculate these parameters from n used pixels with position p_i and signal s_i and the position $\vec{S_0}$ of the source in the camera, the following variables are defined (events with $n < 3$ are skipped):

$$\text{Size:} \quad S = \textstyle\sum_{i<n} s_i \tag{4.1}$$

$$\hat{M} := \sum_{i<n} s_i \cdot \vec{u_i}^T \cdot \vec{u_i} \qquad \text{with} \qquad \vec{u_i} := \vec{p_i} - <\vec{p}> \quad \text{and} \quad <\vec{p}> := \frac{\sum_{i<n} s_i \vec{p_i}}{S} \tag{4.2}$$

$$\tan\delta := \frac{k}{2M_{xy}} \qquad \text{with} \qquad k := \sqrt{(M_{yy} - M_{xx})^2 + (2M_{xy})^2} + (M_{yy} - M_{xx}) \tag{4.3}$$

$$\vec{r} := \hat{R} \cdot \vec{v} \qquad \text{with} \qquad \hat{R} = \begin{pmatrix} \cos\delta & \sin\delta \\ -\sin\delta & \cos\delta \end{pmatrix} \quad \text{and} \quad \vec{v} := <\vec{p}> - \vec{S_0} \tag{4.4}$$

$$\vec{m_i} := (z_{i,x}^3, z_{i,y}^3) \qquad \text{with} \qquad z_i := \hat{R} \cdot \vec{u_i} \tag{4.5}$$

From these quantities the image parameters are calculated:

$$\text{Width, Length:} \quad w = \sqrt{\frac{M_{xx} \cdot \tan^2\delta - k + M_{yy}}{(\tan^2\delta + 1) \cdot S}} \qquad l = \sqrt{\frac{M_{yy} \cdot \tan^2\delta + k + M_{xx}}{(\tan^2\delta + 1) \cdot S}} \tag{4.6}$$

$$\text{Dist, Alpha:} \quad d = |\vec{v}| \qquad \alpha = \arcsin\left(r_y/d\right) \tag{4.7}$$

$$<\vec{m}> := \frac{\sum_{i<n} \sum_i \cdot \vec{m_i}}{S} \tag{4.8}$$

$$3^{rd}\text{ moment :} \quad m_l := \sqrt[3]{|<\vec{m}>_x|} \cdot \text{sign}(<\vec{m}>_x) \cdot \text{sign}(r_x/d) \tag{4.9}$$

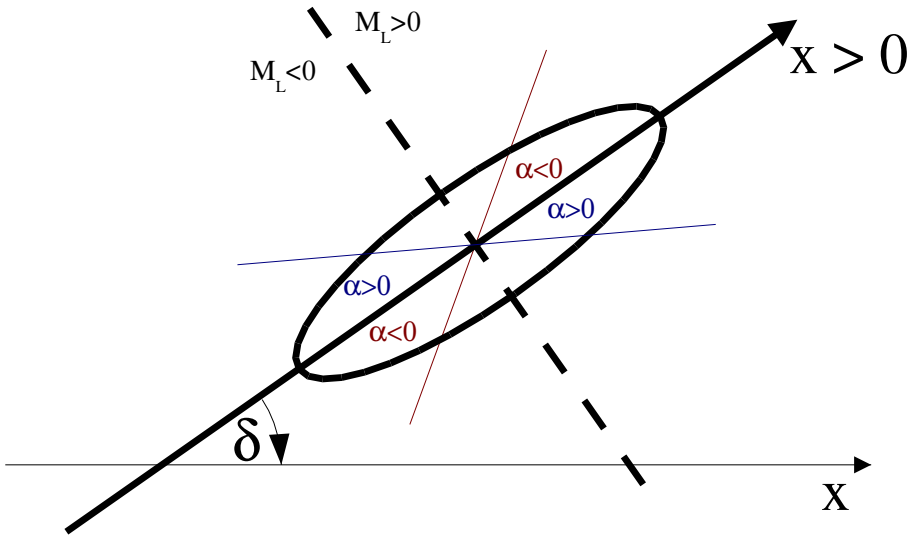

Figure 4.6.: The scheme shows the definition of the sign of the image parameters alpha α and the third moments along the major axis M_L. A more detailed description is given in the text.

The definition of the sign of α and the source-position independent third moment is shown in figure 4.6.

The shower length axis is defined to point towards positive x-values $x > 0$. Therefrom the angle $\delta = [0°, 360°[$ between the shower axis and the x-axis can be derived. The sign of the source-position independent third moment along the length axis is defined w.r.t. the COG of the shower.

The source-position dependent sign of the third moment is calculated by multiplying the source independent third moment with the sign of the projection of the line between COG and the source position onto the length axis.

The sign of $\alpha =]-90°, 90°]$ depends on the position of the source w.r.t. the longitudinal shower axis as shown in figure 4.6. The absolute value of α is defined to be the smallest angle between the line from the COG to the source position and the length axis. Its sign is defined by multiplication of the two signs of the projections of the line from the COG to the source position onto the length and width axis.

For the visualization of the standard deviations, Length and Width, typically an ellipse with them being its major and minor axis respectively is applied.

4.5.2. Additional parameters

For quality checks and energy reconstruction additional parameters are computed:

[3] class MHillas, MHillasExt and MHillasSrc

- N_h: the number of pixels saturating the high-gain
- N_l: the number of pixels saturating the low-gain
- N_u: the number of pixels surviving image cleaning, called *used* pixels.
- N_c: the number of pixels surviving the higher image cleaning level, called *core* pixels.
- A_u: used area, total area of all used pixels.
- A_c: core area, total area of all core pixels.
- L: Leakage, accumulated size of pixels surviving image cleaning in the outermost ring of pixels relative to the size of the event.
- L_2: Leakage2, accumulated size of pixels surviving image cleaning in the two outermost rings of pixels relative to the size of the event.
- C_1: concentration Conc1, the signal density of the pixel with the highest signal density of all used pixels divided by the image Size, i.e. the brightness of the brightest point of the image compared to the total brightness of the image.
- C_2: concentration Conc2, the sum of the signal density of the two used pixels with the highest signal density divided by the image Size.
- N_i number of islands, i.e. isolated pixels, surviving image cleaning

Quality cuts based on these parameters are discussed in section 4.6.5.

4.5.3. Semi classical parameters

For this work additional semi classical parameters have been used. The first parameter has been derived from Width and Length and is called *Area* A. The motivation for its introduction is given in Riegel and Bretz (2005):

$$A = \pi \cdot w \cdot l \tag{4.10}$$

The second parameter is based on the Disp parameter p introduced by the Whipple collaboration (Lessard et al., 2001). It is used to reconstruct the shower origin along the major axis of the shower. For a better reconstruction of shower images, which are not completely contained in the camera a Leakage L dependence of the constant of proportionality has been introduced.

$$p = \xi \cdot (1 - \frac{w}{l}) \qquad \text{with} \qquad \xi = c_0 + c_1 \cdot L^{c_2} \tag{4.11}$$

This small adjustment of ξ describes showers which partly reach out of the camera better. The free parameters c_i are determined with simulated data. The ambiguity of the reconstructed shower origin along the major axis is resolved using the third moment along this axis.

From the reconstructed shower origin the absolute distance ϑ between this incident point and the source position is calculated as:

$$\vartheta^2 := d^2 + p^2 - 2 \cdot d \cdot p \cdot \cos(\alpha) \tag{4.12}$$

4.5.4. Muon Parameters

In addition to the parameters for background suppression and quality assurance discussed before, so-called *Muon Parameters* are calculated. The Cherenkov light of muons, which have an incident point inside the mirror area, is reflected as ring image on the focal plane. The opening angle of the ring, its width and the position of its center depends on the incident angle, the incident position and the energy of the muon. Because of the well known energy distribution of muons and the corresponding distributions of parameters describing their images, muons provide a continuous control over the optical point-spread-function (PSF), the reflectivity and the absolute light calibration of the photo-multipliers. Furthermore, the muon rate can be measured. Due to the well-known muon flux, the measured muon rate provides a useful monitor of the quality of the observation, e.g. the weather conditions. See also Goebel et al., 2005.

To get a high-quality data check only muon images with a well defined morphology are selected. For this selection new parameters are calculated for muon pre-candidates from the cleaned image, i.e. events with a total signal greater than 150 phe.

For this purpose the circle giving the smallest RMS for the deviation of the signal from a circle is fitted using the simplex algorithm (www-10). From the resulting circle the following new parameters can be deduced:

Center: the coordinates of the center of the circle

Mean: the mean deviation from the center, the radius of the circle.

RMS: the mean deviation of the signal from the circle

Events with a radius between 0.6° and 1.35° and a RMS of less than 0.12° are considered good muon candidates. For this events further investigations are performed on the raw image to avoid a bias from the cleaning algorithm. The radial and azimuthal distribution of the signal is evaluated.

For the azimuthal distribution only signals are considered of pixels being closer than 0.2° to the circle, defining a ring, and obeying an arrival time condition:

$$t < 2 \cdot \sigma_t \tag{4.13}$$

with the arrival time t of the signal and the width σ_t of a Gaussian fitted to the arrival-time distribution of signals of all pixels inside the ring.

The so-called *arclength* can be defined as angular region in which the azimuthal profile is above an absolute threshold. The arclength is used to select muon images of which more than a semicircle is visible, which is necessary for quality assurance. The radial profile is fitted using a Gaussian plus a constant giving a good measurement of the width of the light distribution, called *arcwidth*. The constant is necessary because the mean measured signal need not be zero due to the bias of the peak search methods used for signal extraction. After further selection of well measured muon images by

$$\text{arclength} > 190^\circ \tag{4.14}$$

$$0.04^\circ < \text{arcwidth} < 0.20^\circ \tag{4.15}$$

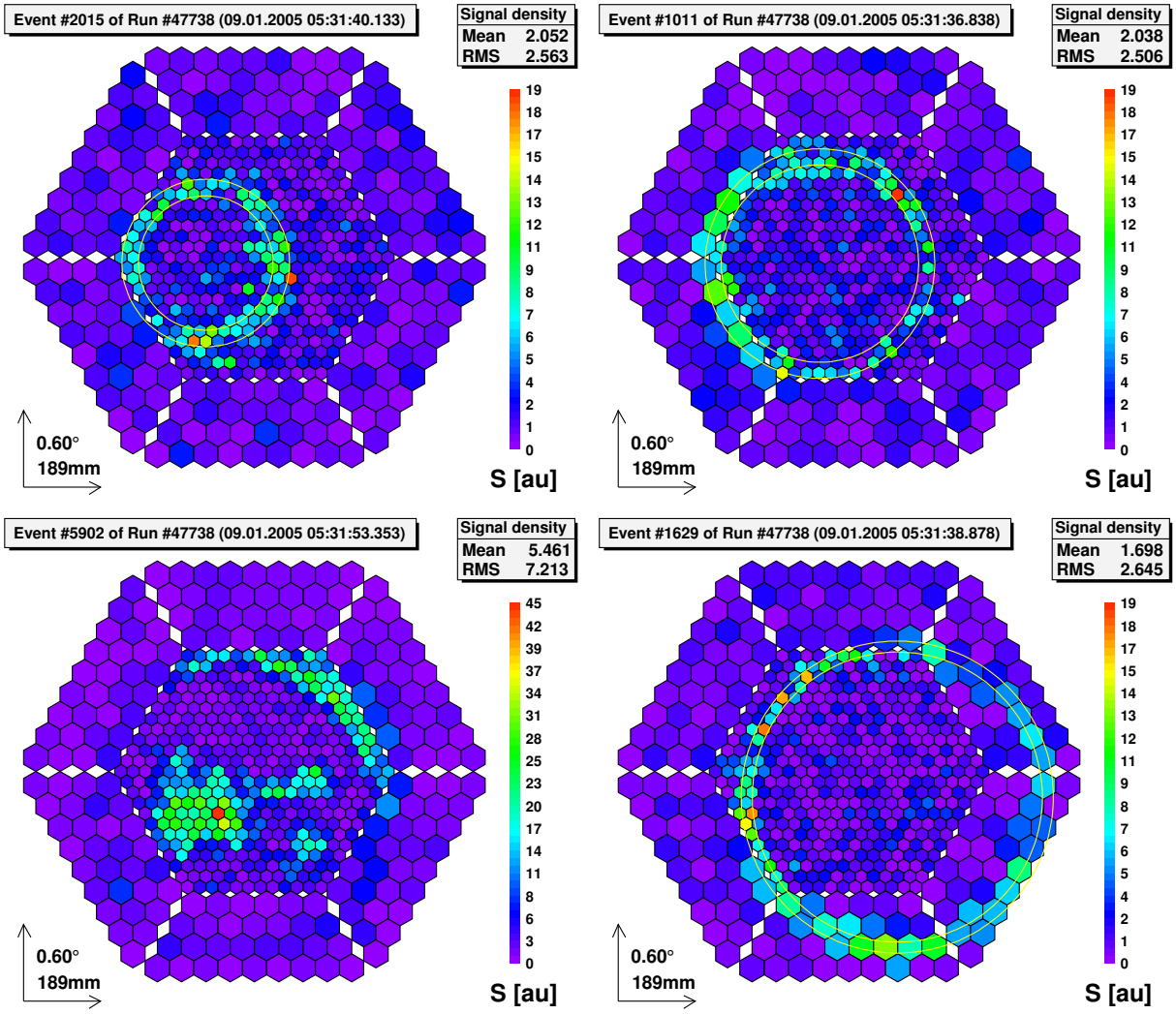

Figure 4.7.: Example of real muon events from run 47738. Three full muon rings with different energies (radius) and an incident point inside the mirror are shown, together with their reconstructed ring (yellow lines). The fourth muon (bottom, left) has an incident point outside the mirror and is visible together with its hadronic source shower.

non-muonic background is suppressed completely ($< 10^{-4}$). The surviving *good* muons have a well defined morphology to draw further conclusions.

With the measured arcwidth, which is a combination of the intrinsic arcwidth of the muon light and the optical point-spread function of the mirror, the latter can be determined. Therefore the arcwidth distribution of simulated muons is fitted to the measured distribution changing the PSF in the simulation. This procedure allows a continuous monitoring of the optical quality of the reflector.

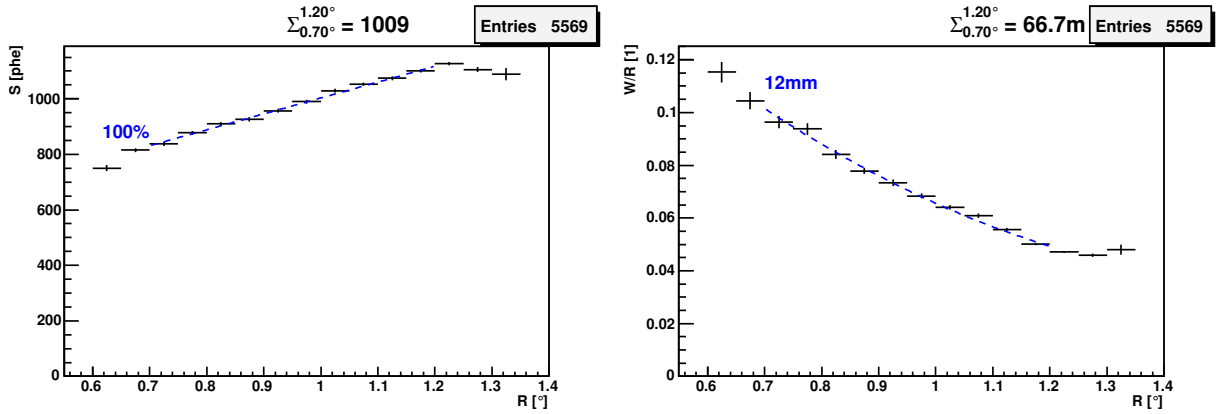

Figure 4.8.: The references for the calibration and PSF produced from simulated muon data calibrated with the signal extractor *digital filter*. Left: Calibration reference, profile of muon $size$ versus $radius$. Right: PSF reference, profile of $arcwidth/radius$ versus $radius$. The blue dashed lines are the fitted references. The number for the weighted sum on top of the histograms is the reference number used to calculate the calibration ratio and the PSF.

By comparing the distribution of muon size, i.e. the integrated intensity, to a simulated distribution, the quality of the conversion from the light yields hitting the mirror into the measured quantity (calibration) can be monitored. This information allows an absolute calibration of the light yield taking the optical quality of the atmosphere and the detector performance into account. This correction is necessary on a time scale in the order of months to correct for losses due to degradation in the performance of the mirror, the plexi-glass window in front of the PMT or the aging of the PMT.

An example for the absolute calibration reference and a PSF of 12 mm determined from a simulated muon sample is shown in figure 4.8.

For the absolute calibration correction coefficients are determined such that the mean muon size of simulated events match the mean muon size of the data. Typically the mean of one to three months in which the telescope performance was known to be stable is taken. The correction coefficients applied are shown in figure 4.9 versus observation period.

If no correction is applied, data taken with different environmental conditions cannot be analyzed together due to different absolute light yield after calibration. By applying this correction

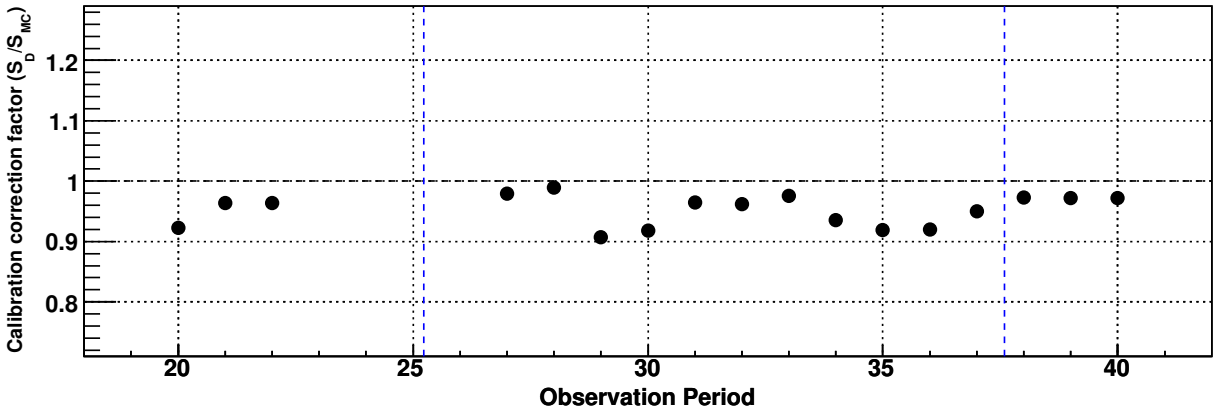

Figure 4.9.: The calibration correction factor for the *digital filter* calibration, i.e. the average size of simulated muons divided by the average size of measured muons. versus the observation period. The two blue dashed lines are New Year 2005 and 2006.

to the data this can be solved, allowing to use identical parameterization of the background suppression methods for all data.

Figure 4.10 shows the time evolution of the absolute conversion factor, i.e. the ratio of real muon events to Monte Carlo muon events after applying the previously determined correction factor. Thus s stable absolute calibration with time is possible and could be achieved.

For the data, which analysis is presented later, the light yield of measured muons is stable and agrees well with simulated data within the statistical and systematical error. An average of $(101.7 \pm 1.0 \pm 1.0)\%$ (on) and $(101.0 \pm 0.8 \pm 1.0)\%$ (off) could be achieved.

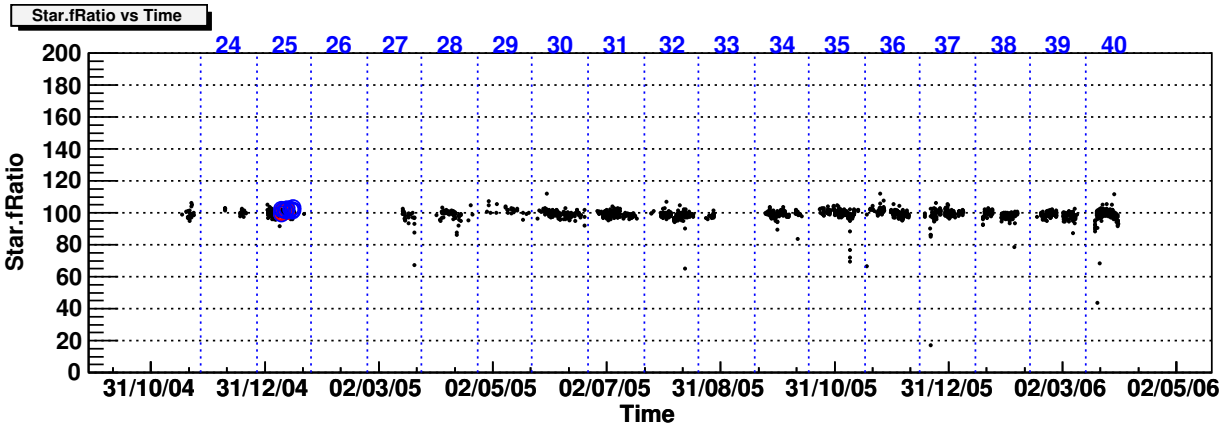

Figure 4.10.: Time evolution of the ratio between Monte Carlo and data calibration after applying the muon correction factors. The blue numbers above correspond to the observation periods. One black dot corresponds to one observation sequence. Data of 1ES 1218+304 is marked with blue (on-data) and red (off-data) circles.

Figure 4.11 shows the quality of the mirror focusing, the measured PSF, versus observation period.

For the data, which analysis is presented later, the measured optical point-spread function is stable and agrees well for on- $(18.2 \pm 0.5 \pm 1.0)$ mm and off-data $(18.0 \pm 0.5 \pm 1.0)$ mm within the statistical and systematical errors. Furthermore this denotes a good agreement between the optical PSF used for simulated (17 mm) and real data, which could be verified by another method. Details about the simulation can be found in section 4.9.

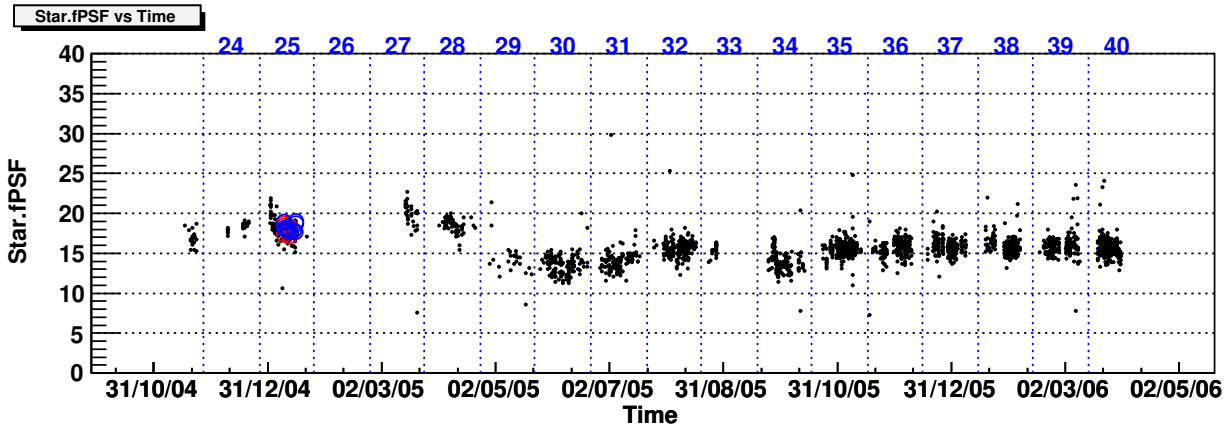

Figure 4.11.: Time evolution of the total optical point-spread-function in units of mm. The blue numbers above correspond to the observation periods. One black dot corresponds to one observation sequence. Data of 1ES 1218+304 is marked with blue (on-data) and red (off-data) circles.

Altering conditions, e.g. changes in the atmosphere or in the detector performance, directly influence the light-yield measured. Consequently the number of muon events, which are just fulfilling the hard- and software trigger condition, changes. Thus a good measurement of the observation quality can be achieved by calculating the muon rate.

For the data set analyzed in this thesis the muon rate is stable and agrees well for on- (0.066 ± 0.04) Hz and off-data (0.67 ± 0.04) Hz within the statistical and systematical errors. A single outlier, corresponding to a $\sim$5 min sequence of data, has been rejected from the analysis.

4.6. Determination of the source position

For the determination of the image parameters (Dist, Alpha, Third Moment, Disp) depending on the source position it is evident, that the source position must be well known. While in on-/off-mode the source position should, in the ideal case, be the camera center, in Wobble mode the source position must be calculated. Both observation modes are explained hereafter.

4.6.1. On-/off-observation mode

In on-/off-observation mode the source is located in the camera center as shown in figure 4.12.

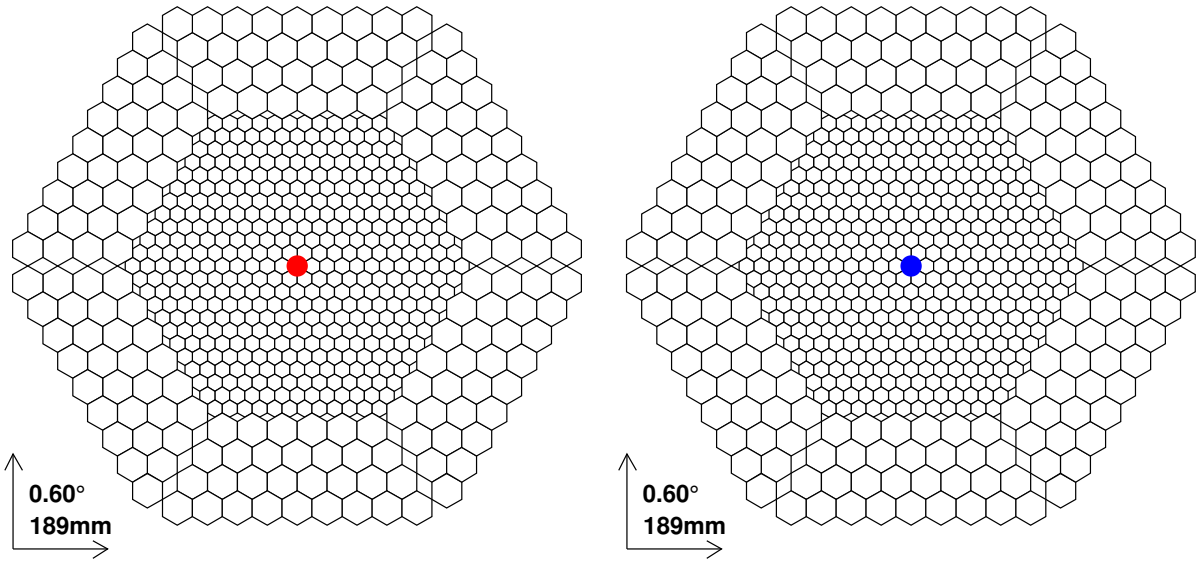

Figure 4.12.: Scheme of the source position in the camera in case of on-source (red, left) and off-source (blue, right) observations the latter used for background determination.

For background determination the signal of the source can obviously not be switched off. Therefore a similar sky region without a source must be observed. As it cannot be done simultaneously with the same instrument, it is done under different conditions (observation length, weather, night-sky-background, etc.). Thus scaling of the background measurement is necessary to achieve an agreement of the background levels of the on- and off-source observations. This scaling factor can only be determined by comparing parts of the data not influenced by the signal, e.g. events which have their origin not at the source position. Having good statistics this scaling factor can be determined accurately enough to get plausible results, however still introducing an additional systematic error.

If a source has been detected, studies on its spectrum are essential to extract the interesting physics about the source. For this purpose the data sample is divided into subsamples of different energy as determined by an energy reconstruction algorithm. To be able to calculate the gamma ray flux for each of these energy bins independently it is necessary, that the scaling of the background in all bins produces reasonable results. Having slightly different conditions for signal and background measurements, e.g. a little higher humidity or the different star light at another sky region, the scale factor for all energy bins might not be unique anymore.

Furthermore the design of MAGIC's camera makes the center of the camera a privileged position. Due to the gap between the outer sectors of the camera (a sketch is shown in figure 4.12) and as only the fine-pixel part of the camera triggers the readout, events are aligned towards the center.

4.6.2. Wobble observation mode

In wobble observations a position symmetric to the source position w.r.t. the camera center is available for background determination, as the source is shifted out of the center. A sketch is shown in figure 4.13.

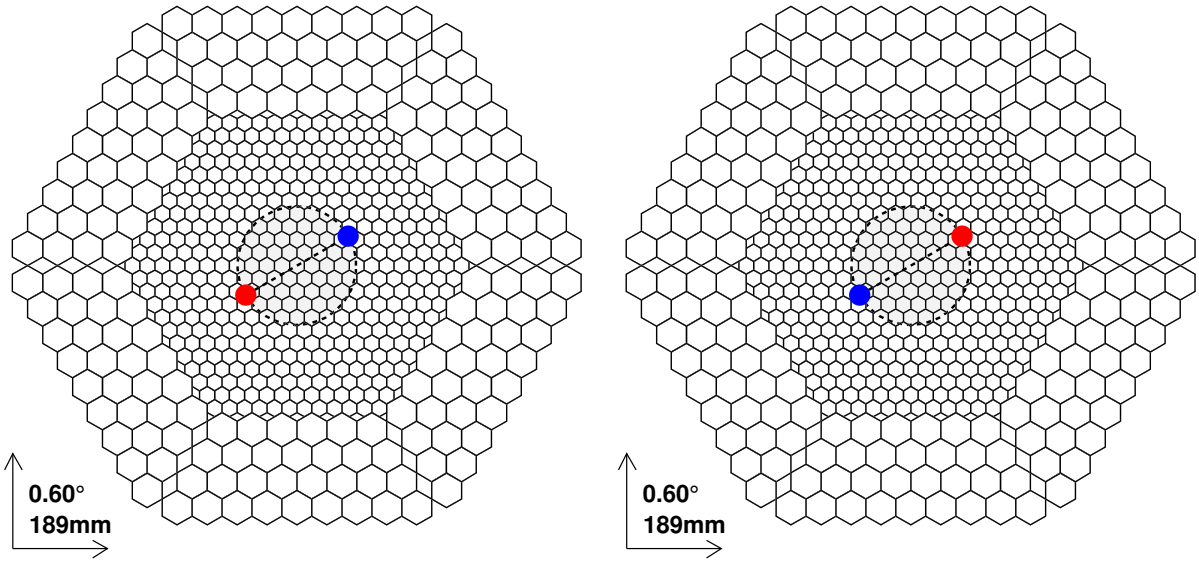

Figure 4.13.: Scheme of the source position in the camera (blue) and the anti-source position (red) used for background determination. To decrease possible systematic effects two sky positions are observed such, that the source position is equally distributed on both sides of the camera (right and left).

This anti-source position is used to determine the background to be subtracted from the signal. This offers the possibility of continuous monitoring of a source without having to interrupt the observations for taking off data. For reasons of symmetry almost identical conditions for both, signal- and background-observation, are given. Consequently in the first order no scaling has to be applied to the background measurement. Due to inhomogeneities (e.g. single broken PMT) in the camera acceptance it might be necessary to apply a small correction. The rotation of the source around the camera center smears out possible inhomogeneities and further decreases a necessary small correction factor. It also improves the quality of the background measurement, because it does not correspond to a unique sky position anymore. However, there is some danger, that the background measurement is not statistically independent from the signal of a strong source. Therefore a special anti-source cut has to be applied, i.e. any event analyzed can not be assigned to both positions. Already simple technique (classical α method) suppress this bias well. More advanced analyses, assigning a single source position to each shower image like Whipple's Disp-method (Lessard et al., 2001), suppress this bias almost completely. This is done by applying source-position dependent cuts also as a veto to the anti-source position and vice versa. Figure 4.14 shows two ϑ^2 signal- and background-plots (Riegel and Bretz, 2005) for different Size ranges taken from wobble mode Crab observations without applying any scaling.

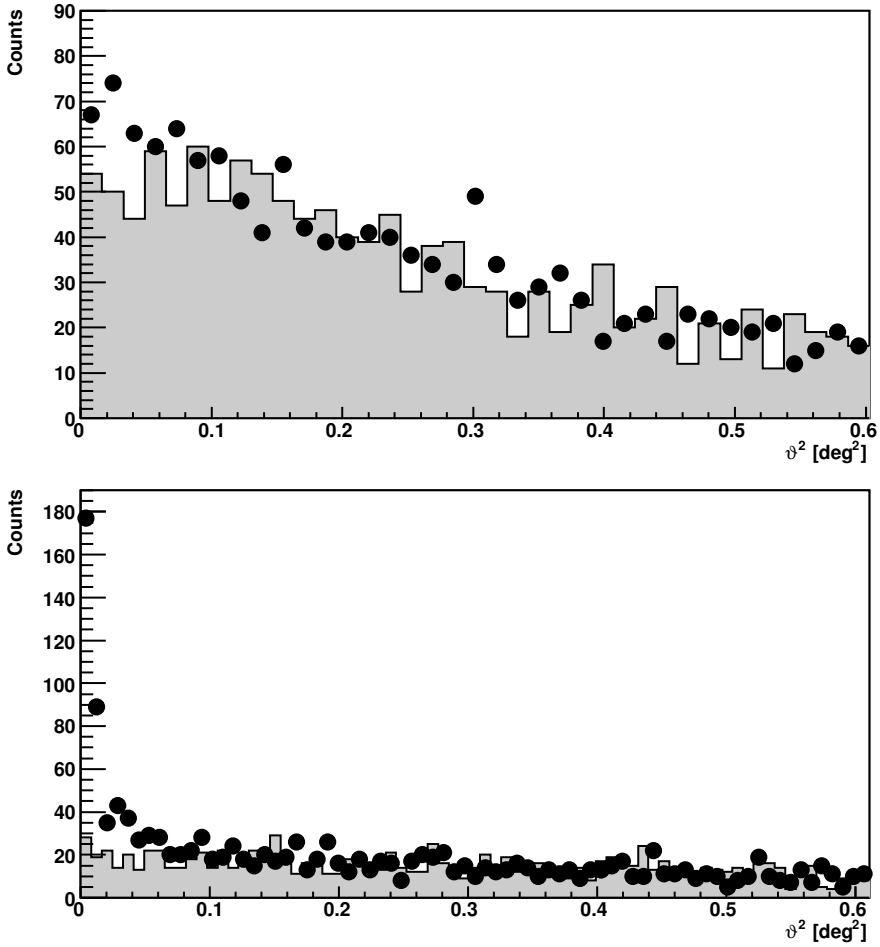

Figure 4.14.: Signal (black dots) and background (gray shaded) as taken from wobble mode Crab observations (loose cuts) and without applying any scaling. Top: low size bin (around 90 GeV). Bottom: medium size bin (around 600 GeV).

4.6.3. Nominal source position calculation

Knowing the observatory location, the exact time of the event and the target position in sky coordinates the nominal position of the camera center can be calculated by a simple matrix operation (rotation). The same operation must be applied to calculate the nominal position of the observation target if – as in wobble mode – it does not coincide with the camera center. This simple matrix operation obviously does not take all tracking relevant effects as aberration or nutation into account. Since all these effects are small compared to the gamma-PSF of a Cherenkov telescope, and have comparable absolute value for the camera center and the target position, they can be neglected.

The conversion between sky coordinates and local coordinates is done by a rotation matrix. The rotation matrix is defined by a unit matrix rotated

1. along z-axis by current time plus longitude of the observatory. With this operation the current time and the deviation of the observatory from the null meridian it taken into account.

2. along y-axis by the latitude of the observatory minus pi half. This rotation corrects the coordinate system for the deviation of the observatory from the pole.

3. along z-axis by pi. This rotation corrects the counting direction which is contrary for right ascension and azimuth angle.

Applying the resulting matrix to a vector in sky coordinates converts the base of the sky coordinate system (right ascension, declination) coordinate system correctly into an ideal local coordinate system (zenith distance, azimuth) for the observation time and observatory location.

The calculation of the source position in the camera plane is done by

1. rotating the vector of the nominal source position such that the camera center becomes the origin of the coordinate system.

2. projecting this vector onto the camera plane in a distance of 17 m.

4.6.4. Source position correction

Having calculated the nominal source position in the camera plane a correction for tracking inaccuracies must be done. Therefore the deviation measured by the starguider is used. While the relative measurement of tracking inaccuracies by the starguider is well done an absolute calibration is missing until now. As a first order approximation the calibration constant of both axis (x- and y-axis in the camera/CCD-frame) is assumed to be constant. However, a wrong calibration of the starguider would result in a constant fake mispointing but it would still give better results due to the correct relative corrections. The calibration constants have been determined as $dx = 7\,\text{mm}$ and $dy = -16\,\text{mm}$. For this purpose offsets measured by the starguider during two month of data taking are plotted and it is assumed, that the largest part of this data was taken without any noticeable tracking offset. The plots are shown in figure 4.15. As the current starguider implementation delivers the pointing deviation in local coordinates (Zd, Az), it first must be converted into a deviation in the camera plane. Therefore the same algorithm as for the nominal source position is used, i.e. setting the camera center to the nominal camera center and the source position to the nominal camera center plus the measured deviation. The resulting deviation in the camera plane plus the calibration offset are then added to the calculated nominal source position.

4.6.5. Quality cuts

After the source position is correctly calculated and corrected all necessary parameters are available. Before beginning to identify gammas from the target source out of the cocktail of measured showers some quality cuts are performed in

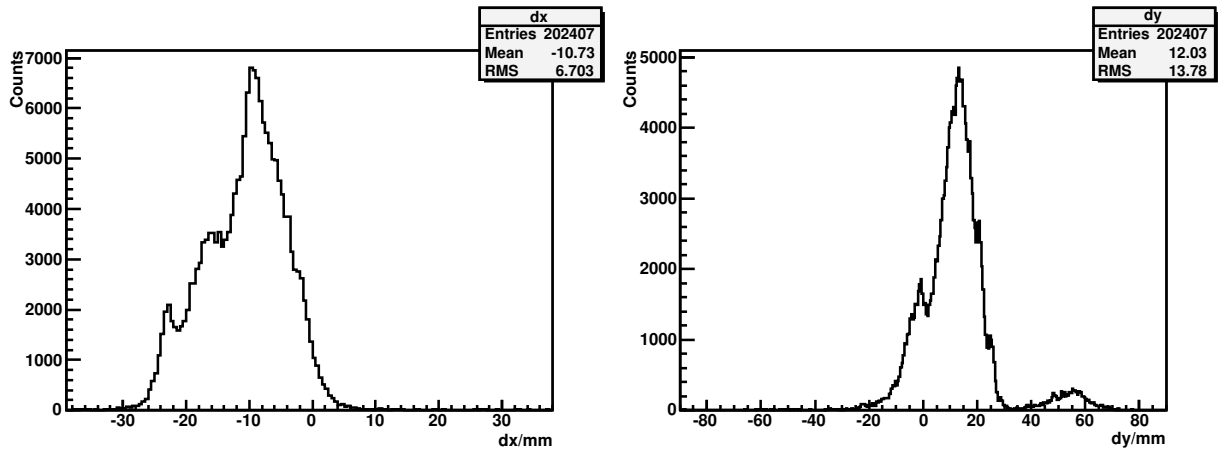

Figure 4.15.: The dx- and dy-distribution of the deviation measured by the starguider for all observations between March and July 2005. The small peak at $dy \simeq 55\,\mathrm{mm}$ is coming from a backlash problem of the tracking system. The origin of the small side peaks visible is not yet understood. They might be due to a mispointing at high zenith angles correctly detected by the starguider.

- the number of saturating hi-gain pixels N_h and the image parameter *Area* A:

$$N_h > 1 \qquad \text{and} \qquad A > 0.0014 \cdot N_h + 0.02 \tag{4.16}$$

- the number of saturating lo-gain pixels N_l:

$$N_l < 2 \tag{4.17}$$

- the number of pixels which survived image cleaning N_u:

$$N_u > 5 \tag{4.18}$$

- the ratio of the signal in the outer pixels to the parameter Size, Leakage L:

$$L < 0.3 \tag{4.19}$$

- the number of islands N_i of the cleaned image:

$$N_i < 3 \tag{4.20}$$

All these cuts remove non-gamma like events induced by very high energetic showers, artificial triggers due to environmental influences (e.g. car light) or detector malfunctions.

4.7. Background suppression

For the standard analysis of MAGIC data cuts in the distributions of image parameters were searched, which are most robust w.r.t. possible variation of the external environment (weather conditions, night-sky-background, etc.) and which can be universally used for comparative and quick-look analyses. A wide range of possible cuts optimized for these purposes were investigated systematically in Riegel and Bretz, 2005.

For completeness they are listed here:

$$\vartheta^2 < c_0^2 \tag{4.21}$$

$$A(S) < c_3 \cdot (1 - c_4 \cdot (\log_{10}(S) - c_5)^2 \tag{4.22}$$

The main advantage of this parameterization is a high robustness due to the limited amount of free parameters c_i without loss in separation power.

4.8. Effective observation time

The effective observation time T_{eff} is defined as the time range, within which the recorded number of cosmic events N would be obtained under ideal conditions (omitting dead-time).

T_{eff} can be determined from the distribution of time differences Δt between consecutive cosmic events. The exponential slope λ of this distribution is the event rate for cosmic events in the ideal case. If N is the total number of recorded cosmic events, T_{eff} is obtained by

$$T_{eff} = \frac{N}{\lambda} \tag{4.23}$$

In the case of a finite dead time T_d the distribution (for $\Delta t > T_d$) is exponential with the same slope λ, fitted in a region of Δt, which is not affected by the dead time.

An example for such a distribution and the corresponding fit is shown in figure 4.16.

4.9. Monte Carlo

After an appropriate background suppression the energy of the gamma-ray candidates must be reconstructed to compile their energy distribution. For this purpose the spectrum of the primary particles annihilating in the atmosphere is calculated by correcting for the detector's and analysis' efficiency, dividing by the maximum collection area and the effective observation time. The resulting spectrum might still be improved by an appropriate unfolding which corrects for asymmetric spill-over originating from uncertainties in the energy reconstruction when steep spectra are reconstructed.

For both, energy reconstruction, with or without further unfolding, and the determination of the efficiencies Monte Carlo simulation must be used. Due to the fact that no current accelerator is able to generate the necessary energies to produce an extended air shower as measured by

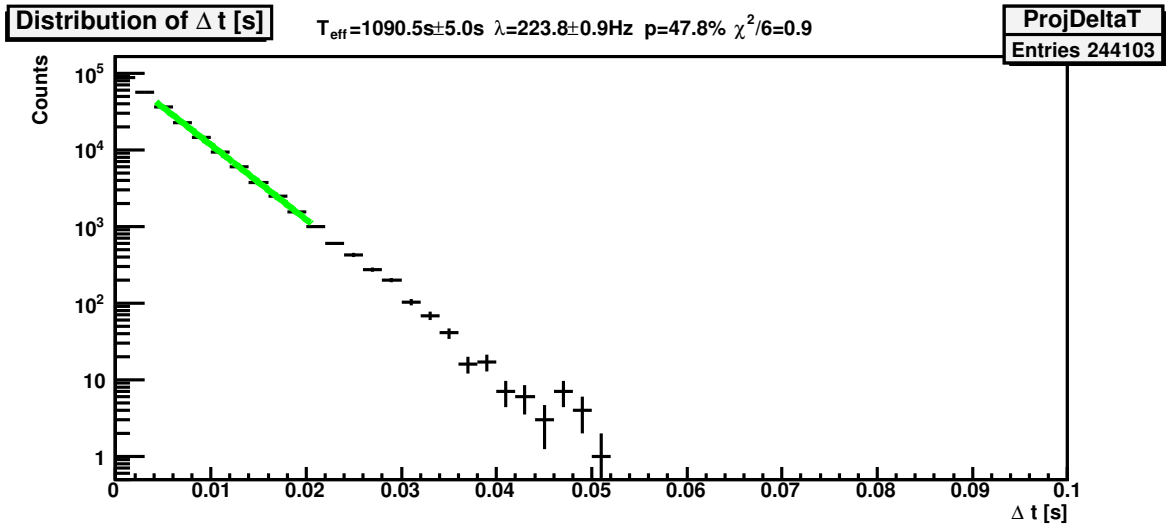

Figure 4.16.: The effective on time is determined by an exponential fit to the distribution Δt of the arrival times of two consecutive events. The fit region has been chosen to be independent of the dead-time and statistical fluctuations. The determined effective on time T_{eff} and its error determined from the fit is displayed, the event rate in the ideal case λ, the fit probability p and χ^2/N (N being the number of degrees of freedom). The fit is shown in green. The shown plot was made for the Sequence 47736.

IACT and no direct measurement of the primary's energy is possible (which would make the IACT-technique obsolete anyhow) energy calibration can only be done through Monte Carlo simulations. For air shower simulation a version of CORSIKA V6.023 (Heck et al., 1998) is used. The detector simulation, including reflector, camera and digitization, is outlined in Majumdar et al., 2005.

Simulated gamma-showers were produced for energies between $E_0 = 10\,\text{GeV}$ and $E_1 = 30\,\text{TeV}$, following a power law with a spectral slope $f_0(E) = dN/dE \propto E^{-2.6}$.

Since all quantities calculated from the Monte Carlo data (e.g. collection area, unfolding coefficients) depend on the shape of the differential Monte Carlo spectrum, it is essential that the Monte Carlo input-spectrum f_1 and the resulting spectrum f_0 of the analysis agree. This can be ensured by iteratively redoing the analysis with different input spectra until input and output spectra agree.

To fit the differential spectrum $f_1(E)$ of the observed source each Monte Carlo event with energy E is weighted by

$$w = n \cdot \frac{f_1(E)}{f_0(E)} \qquad \text{with} \qquad n = \frac{\int_{E_0}^{E_1} f_0(E)dE}{\int_{E_0}^{E_1} f_1(E)dE} \tag{4.24}$$

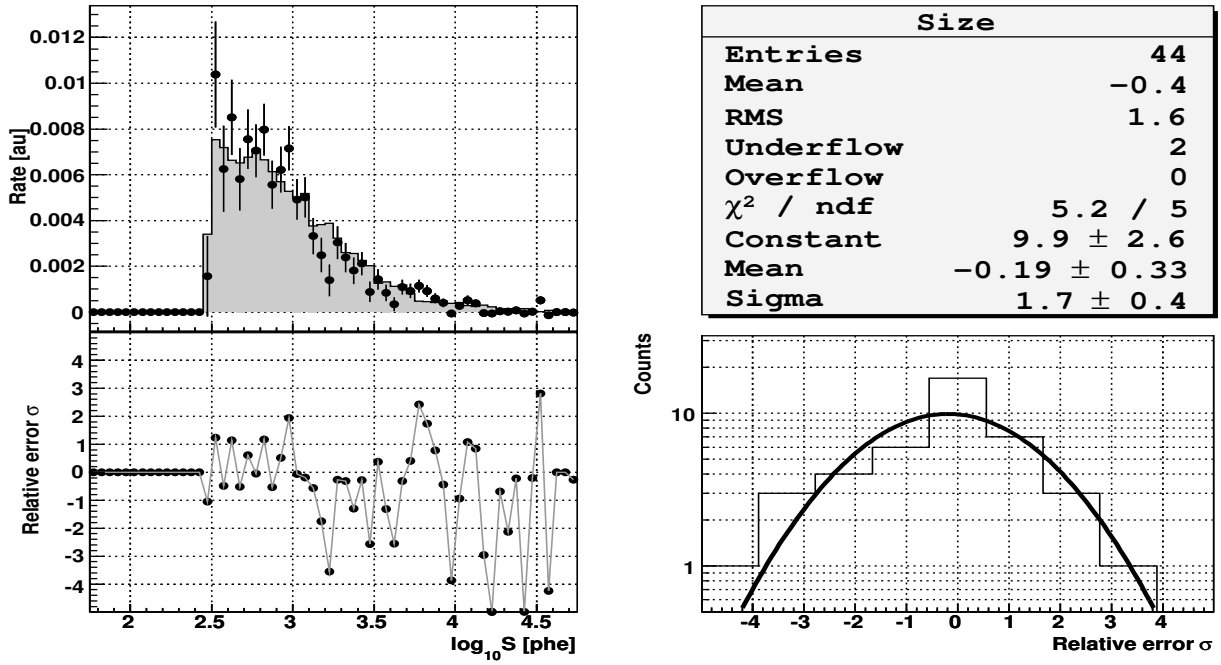

Figure 4.17.: Comparison of the distribution of the Size-Parameter (top left) between Monte Carlo simulations (gray shaded) and the gamma signal (small dots) extracted from a strong source with a very loose background-suppression cut and a lower size cut of 300 phe. The deviation between both is expressed in units of the error of the measurement (bottom left). Its distribution (bottom right) shows a Gaussian shape. The result of a fit of a Gaussian function is shown top right.

The normalization n is calculated such, that the total number of events do not change. In the special case the differential spectrum of the source can be expressed as a pure power-law $f_1(E) = dN/dE \propto E^{-\alpha}$ this yields

$$w = \frac{E_1^{-1.6} - E_0^{-1.6}}{E_1^{1-\alpha} - E_0^{1-\alpha}} E^{-\alpha+2.6} \tag{4.25}$$

For the energy calibration of the analysis the simulation is the only calibration source, which always leads to systematic errors in the energy reconstruction of the spectrum. To keep these systematic effects as small as possible the quality of the Monte Carlo simulation is essential.

Due to the good background determination in Wobble-Mode observations it is possible to extract the distribution of image parameters for electromagnetic showers coming from an observed strong source just by subtracting the measured off- from the measured on-distribution. If this distribution does not fit well, this could indicate a problem in the shower simulation or the environment (atmosphere, detector performance, etc).

To get a data sample as unbiased as possible no background suppression cuts should be made. To suppress signals coming from non-shower events (such as car-light, etc.) loose quality cuts might be applied.

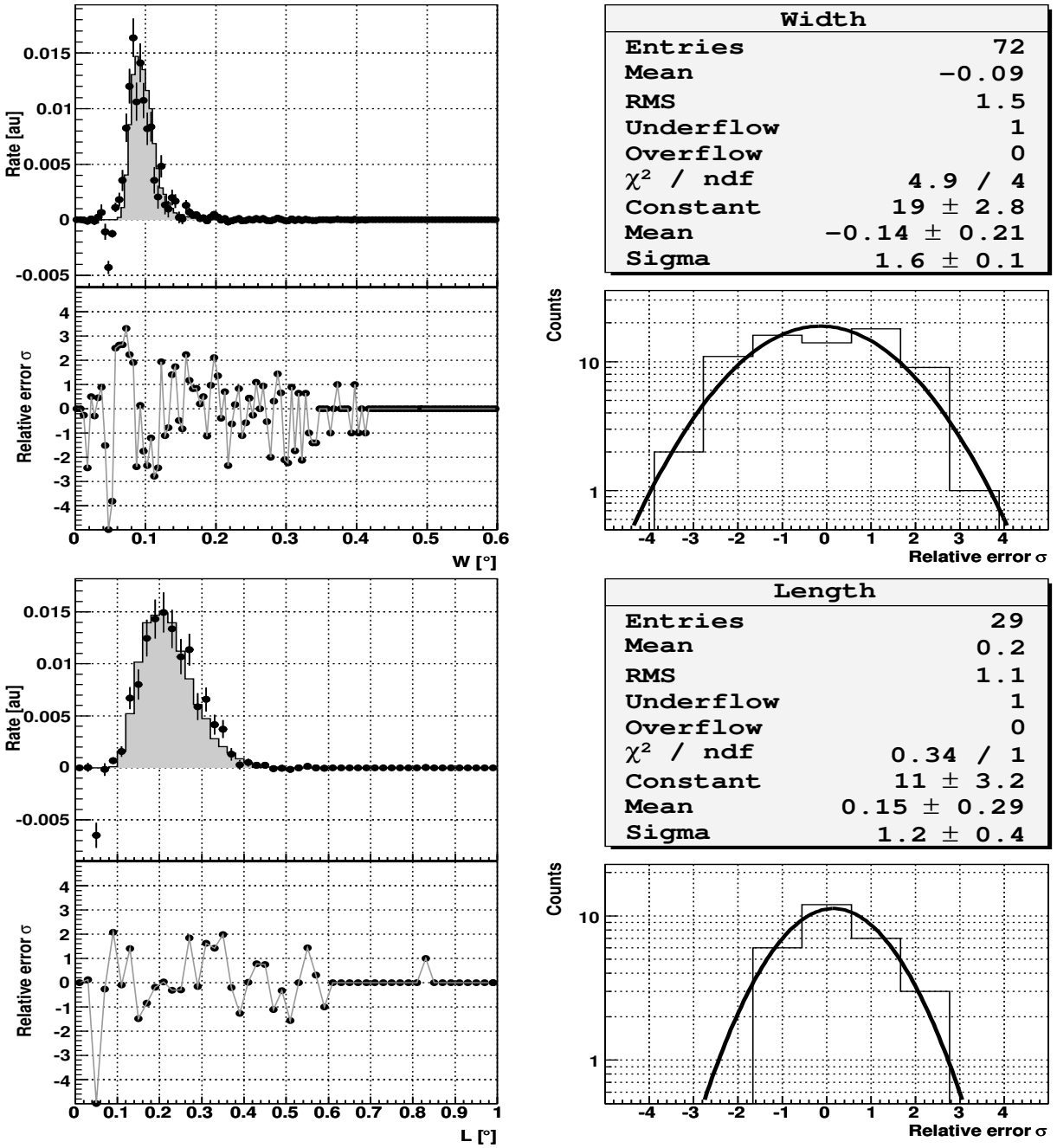

Figure 4.18.: Comparison of the distribution (top left) of the Width- (top) and Length-Parameter (bottom) between Monte Carlo simulations (gray shaded) and the gamma signal (small dots) extracted from a strong source with a very loose background-suppression cut and a lower size cut of 300 phe. The deviation between both is expressed in units of the error of the measurement (bottom left). Its distribution (bottom right) shows a Gaussian shape. The result of Gaussian-fit is shown (right).

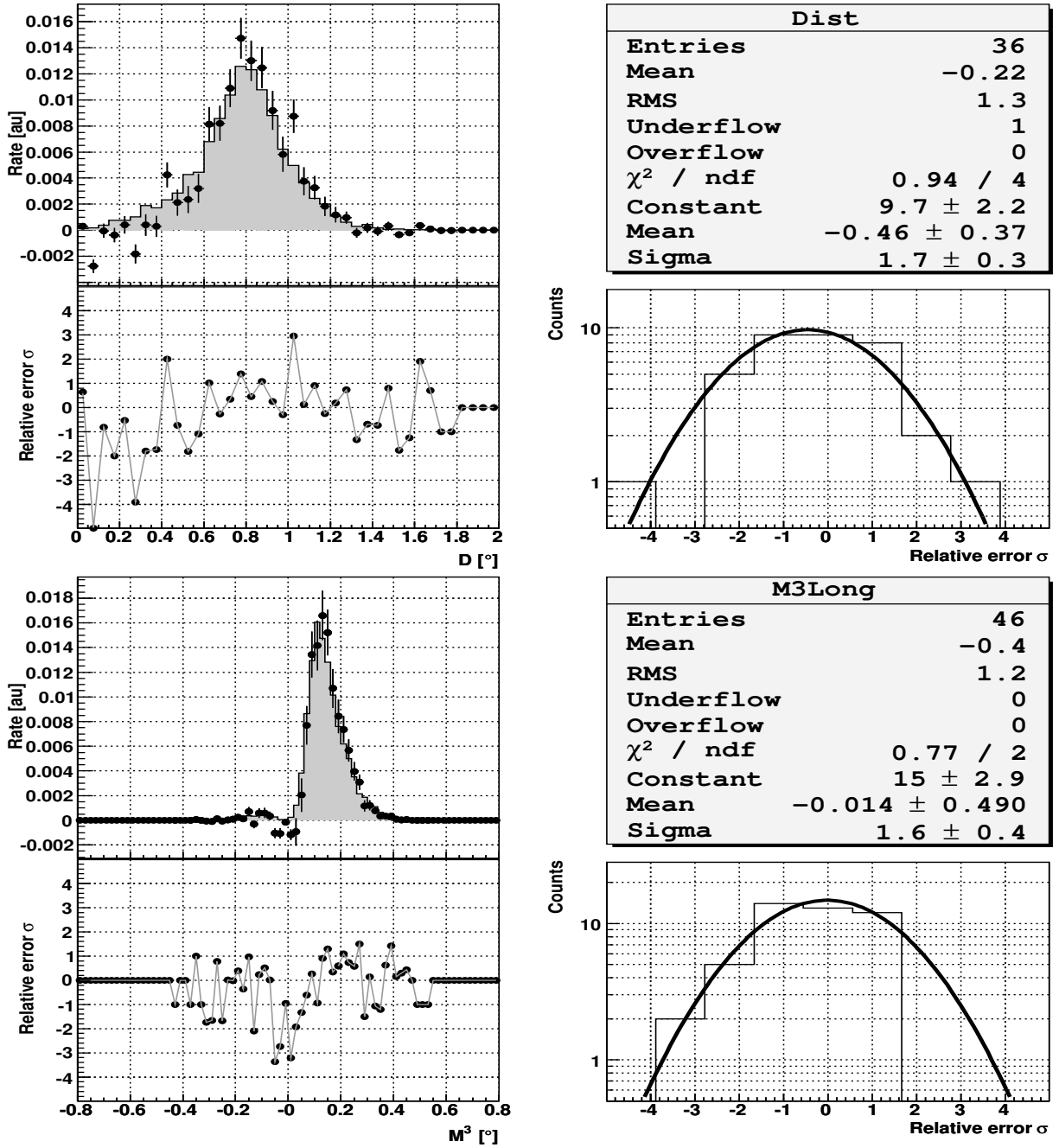

Figure 4.19.: Comparison of the distribution (top left) of the Dist- (top) and M3Long-Parameter (bottom) between Monte Carlo simulations (gray shaded) and the gamma signal (small dots) extracted from a strong source with a very loose background-suppression cut and a lower size cut of 300 phe. The deviation between both is expressed in units of the error of the measurement (bottom left). Its distribution (bottom right) shows a Gaussian shape. The result of Gaussian-fit is shown (right).

For this cross-check observations of the strongest steady source known in the energy range accessible by IACT, the Crab-Nebula (Weekes et al., 1989), have taken place contemporarily.

The Crab-Nebula has been observed in wobble mode three nights around the 10^{th} January 2005, which is just a few days before the observations of 1ES 1218+304.

From the data recorded the image parameter distributions for gamma induced showers could be extracted. In figures 4.17, 4.18 and 4.19 a comparison between this extracted signal and the distribution of image parameters calculated for Monte Carlo simulated gammas is shown. The plots are restricted to the image parameters used in the data analysis. The top-left plot shows the parameter distribution with small dots and errors. The distribution for Monte Carlo data is shown as gray shaded histogram. The bottom-left plot shows the deviation between both distributions in units of the error of the measurement versus the image parameter. The bottom-right plots show the distribution of the deviation from the bottom-left plot with the fit of a Gaussian. Only non-empty bins, i.e. bins with at least one event in either the Monte Carlo or data, have been considered. The properties of the histogram and the fit parameters are shown in the top-right pad.

All plots show that both distributions fit well enough, that no systematic error greater than the statistical one need to be expected from the usage of simulations for energy calibration and efficiency determination discussed hereafter.

Special attention must be given to the zenith angle distribution of the used Monte Carlo sample. Since showers observed at different zenith angles have different distances from the observer thus the morphology of a shower image will change with zenith angle. To account for this the events in the Monte Carlo sample are always weighted to match the zenith angle distribution of the effective observation time.

4.9.1. Effective collection area

The effective collection area $A_{eff}(E)$ has been calculated from the number of events N_0 produced in a well defined area A_0 around the telescope by the simulation and the number of events N surviving the cuts:

$$A_{eff}(E) = A_0 \cdot \frac{N(E)}{N_0(E)} \tag{4.26}$$

The effective collection which was used for the source analysis hereafter is shown in figure 4.20.

4.9.2. Energy reconstruction

The energy of the primary gamma rays can be reconstructed from the correlation between several image parameters. To reconstruct the energy of each individual shower a statistical learning method called *Random Forest Regression* method is used in this analysis. A more detailed description of the method is found in Breiman, 2001.

The Random Forest is trained with the image parameters Size S, Dist D, Zenith Angle θ, Area A, Used Area A_u, Core Area A_c, Leakage L, Leakage2 L_2, Conc1 C_1, and Conc2 C_2 of an

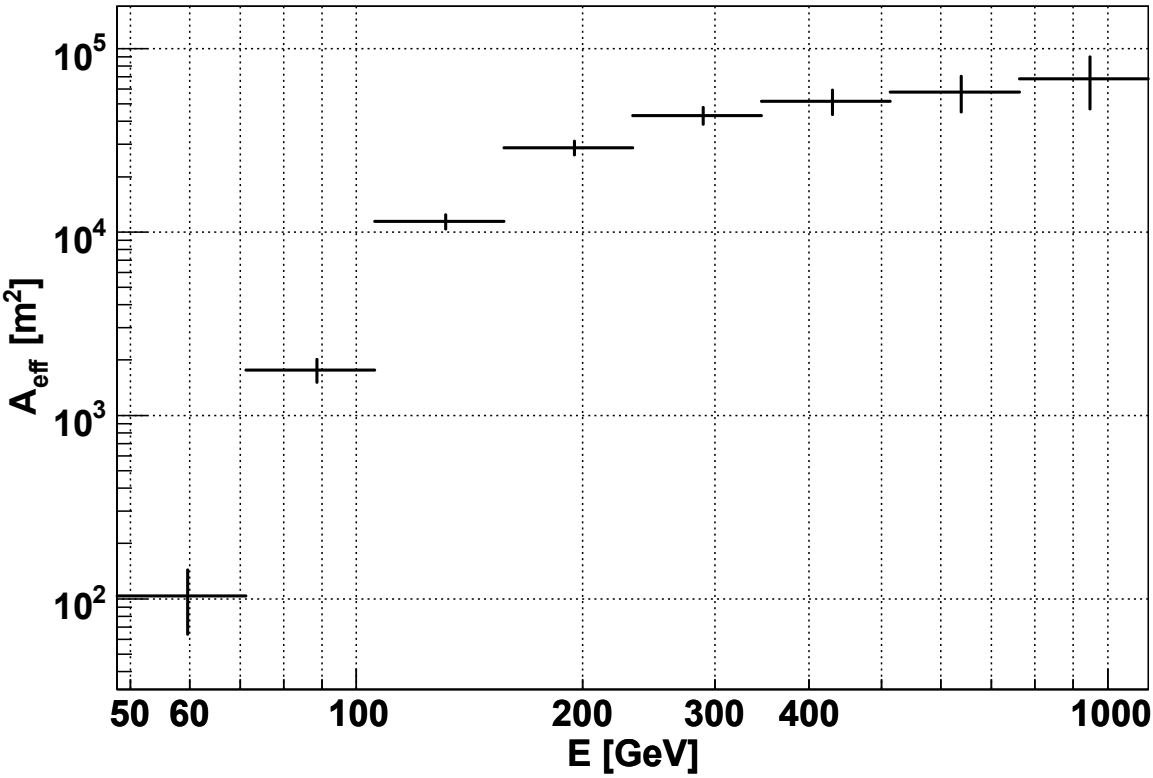

Figure 4.20.: Effective collection area in units of m^2 versus energy determined from a Monte Carlo sample with a spectral slope of $\alpha = 3.0$ (corresponding to the resulting spectrum of 1ES 1218+304) for a zenith angle distribution weighted to match the observations discussed later.

unweighted Monte Carlo sample. The far most important parameter for energy reconstruction is the Size-parameter comparable with the total brightness of the image, giving an average energy resolution of $\sim$33% if used alone. The parameters Dist D and Zenith Angle θ contain some additional geometry information and improve the energy resolution to $\sim$27%. All other parameters further support the energy reconstruction but do not show a clear or simple correlation with the primary energy. In total an average energy resolution of less than 25% can be obtained.

To determine the energy resolution a two-dimensional histogram of $r = (E_{est} - E_{mc})/E_{mc}$ versus E_{est} is filled for a Monte Carlo test-sample and each projection in r is fitted by a Gaussian. The mean of the Gaussian is called *bias* and should be small compared to the resolution. It includes under- and overestimation resulting in spill-over from one bin of E_{est} into neighboring bins. For a good energy estimator the bias versus E_{mc} must vanish. In the case of IACT this normally can not be achieved for the lowest energies. This is due to the fact, that the lowest energy showers surviving background suppression necessarily are the largest showers of this energies looking like higher energy showers. The *resolution* is defined as the width σ of the Gaussian. Since the real energy of the events is not known in a data analysis, the resolution is

determined as a function of the estimated energy instead. If the systematic over-estimation of the energy for low energies is taken into account the resolution of events below 100 GeV can be more than two times worse than the average energy resolution.

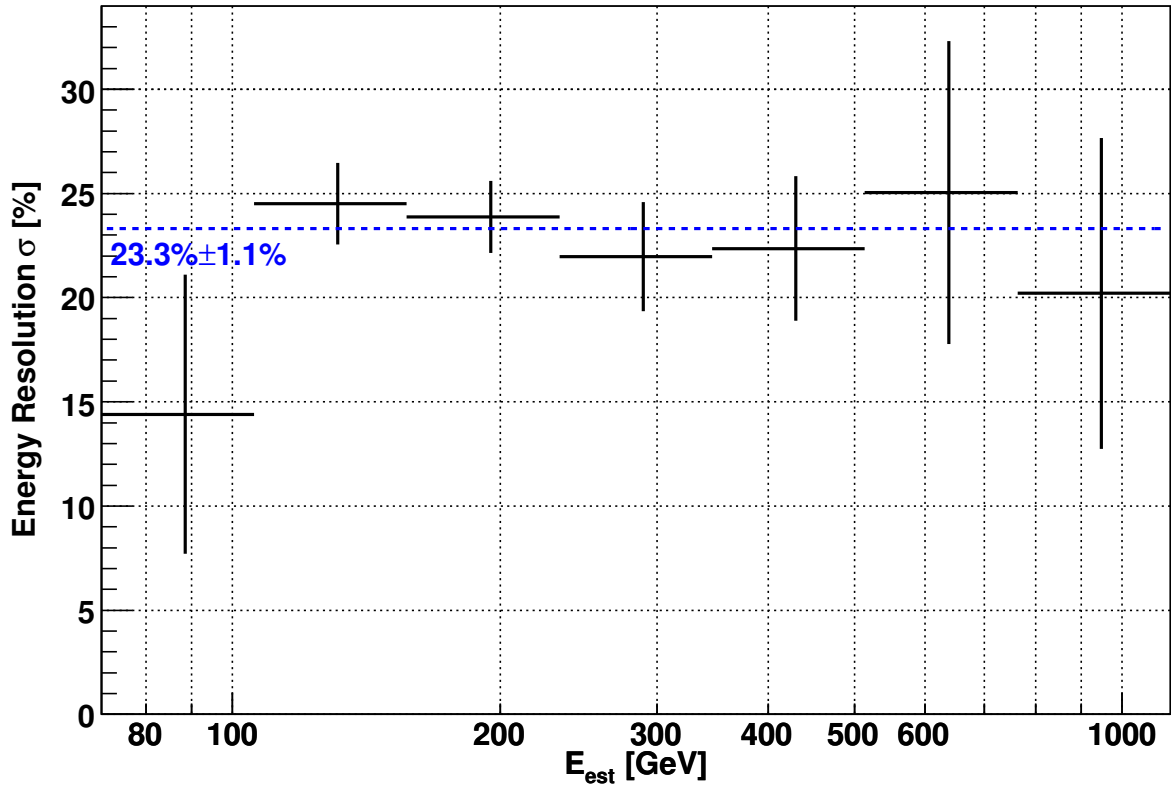

Figure 4.21.: Energy resolution, determined as described in the text, versus estimated energy. The resolution is stable in the energy range between 100 GeV and 1 TeV, slightly decreasing to higher energies. The blue line corresponds to the average. The smaller resolution in the first energy bin is an artifact from low statistics.

The average energy resolution for the source analysis shown hereafter yields $23.3\% \pm 1.1\%$, slightly decreasing from $\sim$25% at 100 GeV to $\sim$20% at 1 TeV. Its dependence from the estimated energy is shown in figure 4.21.

4.9.3. Spill-over correction coefficients

The distribution of the reconstructed energy for mono energetic showers is nearly Gaussian. If the measured differential spectrum is steep much more events are erroneously classified in a higher energy bin than vice versa. To correct for this asymmetric spill-over, correction-coefficients are calculated from the number of events $N(E_{mc})$ before energy estimation and after $N(E_{est})$ energy estimation.

$$f(E_{est}) = \frac{N(E_{mc})}{N(E_{est})} \tag{4.27}$$

Discussion The advantage of using the correction coefficient method for spill-over corrections is its robustness against numerical uncertainties and its simplicity. The disadvantage is its dependence on the Monte Carlo spectrum used to determine the correction coefficients.

For high energies the energy resolution is roughly energy independent. Therefrom spill-over from one energy bin into a neighboring bin also becomes independent of the energy.

If c_i is the contents of one bin and r the constant spill-over factor dependent mainly on the energy resolution, the contents of one bin after spill-over can be written as

$$c_i' = c_i + r \cdot c_{i-1} - r \cdot c_i = c_i + r \cdot (c_{i-1} + c_i) \tag{4.28}$$

A scheme of this spill-over is shown in figure 4.22.

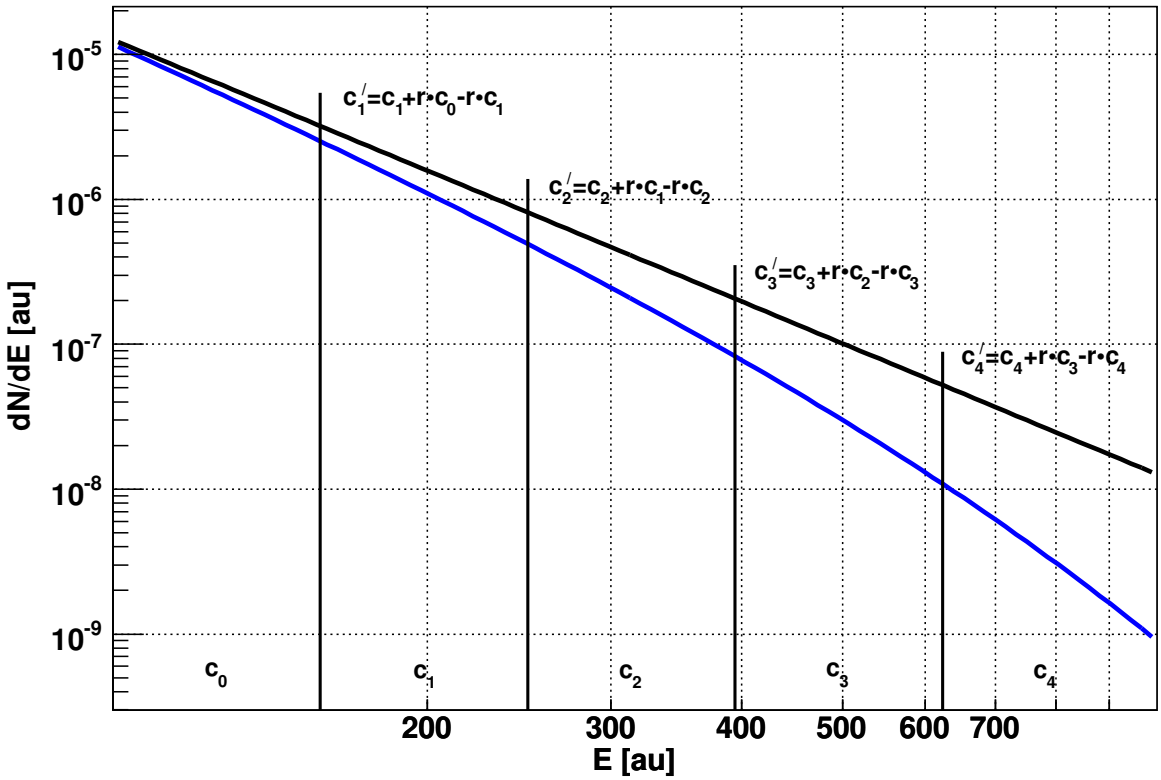

Figure 4.22.: Scheme of the spill-over. c_i denote the bin contents, the black line corresponds to a pure power-law, the blue-line to a power-law with cutoff. The formulas give a simplified version calculating the spill-over, if it is assumed that the spill-over factor r is independent of the energy.

The correction coefficient f in this case (cf. equation 4.27) yields

$$f = \frac{c_i}{c_i'} = \frac{c_i}{c_i + r \cdot (c_{i-1} - c_i)} = \left(1 + r \cdot (\frac{c_{i-1}}{c_i} - 1)\right)^{-1} \tag{4.29}$$

In the case of a pure power-law describing the number of events per bin $c \propto E^{-\alpha+1}$ and a logarithmic binning ($E_i = k \cdot E_{i-1}$) the quotient c_{i-1}/c_i and consequently the correction coefficient f becomes energy independent as expected

$$\frac{c_i}{c_{i-1}} \propto \frac{E^{-\alpha+1}}{(\frac{E}{k})^{-\alpha+1}} = k^{-\alpha+1} \propto 1 \tag{4.30}$$

In case of a power-law with cutoff $c \propto E^{-\alpha+1}e^{-E}$, as expected from the attenuation due to the MRF, the ratio c_i/c_{i-1} is calculated as

$$\frac{c_i}{c_{i-1}} \propto \frac{E^{-\alpha+1}e^{-E}}{(\frac{E}{k})^{-\alpha+1}e^{-\frac{E}{k}}} = k^{-\alpha+1} \cdot e^{-E(1-\frac{1}{k})} \propto e^{-w \cdot E} \qquad \text{with} \qquad w > 0 \tag{4.31}$$

Consequently in the case of a power-law with cutoff the ratio $c_i/c_{i-1} \propto e^{w \cdot E} > 1$ is greater than in the case of a pure power-law and increases with energy. Accordingly this leads to a smaller correction coefficient, decreasing with energy. Hence, if the correction coefficient is calculated for a pure power-law and applied to data corresponding to a power-law with cutoff, the true number of events per energy bin is overestimated. This effect becomes important around the cutoff energy and increases with energy, thus favoring the reproduction of a power-law spectrum also in the case of a power-law with cutoff.

If the measurement yields enough statistics that the shape of the spectrum can be well determined, this deviation is compensated by ensuring good agreement between the Monte Carlo spectrum, used to determine the correction coefficients, and the resulting spectrum. If low statistics prevents the determination of the shape of the resulting spectrum an additional systematic uncertainty mainly in the low energy bins is introduced. The low statistics in the highest energy bins are unavoidable and a consequence of the steep spectrum. The situation can be worsened by overall low statistics and a cutoff energy near the highest energy bins, which further complicates the determination of the spectral shape. In the case of a power-law spectrum with cutoff and an assumed power-law this leads to a systematic overestimation of the highest energy bins increasing with energy.

4.10. Spectrum calculation

The energy spectrum is now calculated as:

$$N(E_{mc}) = \frac{N_{exc}(E_{est}) \cdot f(E_{est})}{A_{eff} \cdot T_{eff}} \tag{4.32}$$

To make sure that the resulting spectrum is consistent with the originally produced Monte Carlo spectrum, the result is fed into the algorithm and the Monte Carlo events are weighted accordingly, cf. equation 4.25. This procedure is followed iteratively until the weighted spectrum and the resulting one agree. In this case also a good agreement between the size distribution of Monte Carlo gammas and excess events is expected and can be checked. Therefore the distribution of Monte Carlo gammas is normalized to the effective observation time by a factor f:

$$f = \int_{E_0}^{E_1} E^{-\alpha} dE \cdot \frac{A_0 \cdot T_{eff}}{N_0} \tag{4.33}$$

The resulting distribution is equivalent to a Monte Carlo distribution measured in the observation time T_{eff} from a source spectrum with spectral index $-\alpha$.

The statistical errors are calculated according to Li and Ma (1983) equation 5.

5. Automatic analysis

The first rule of any technology used in a business is that automation applied to an efficient operation will magnify the efficiency. The second is that automation applied to an inefficient operation will magnify the inefficiency.

— Bill Gates.

With all systems working and continuously good weather the readout system of the MAGIC-telescope can record more than 2 TB per month corresponding to more than 120 h of data taking and more than 10^8 events. Due to a limitation of the file-size to less than 2 GB this corresponds to more than 3000 files (a.k.a. runs), which have to be grouped together by their observation target and analyzed. In addition more than twice the number of data files is stored by subsystems of the telescope, e.g. the measured PMT currents and the tracking position. See also Dorner and Bretz, 2005; Dorner et al., 2005.

Handling such a huge number of files, corresponding to a wide variety of different targets, must be done failsafe. Only an automatic procedure grouping these files to final datasets of different targets and an adequate automatic analysis ensures, that all data can be analyzed shortly after the data is available for analysis, either locally after data taking or at a secondary datacenter after transfer. Consequently discoveries of new sources can be cross-checked immediately manually and considered in the running observation schedule.

Furthermore each improvement of the analysis software in any aspect demands repeating the analysis of old data getting the best currently possible physics result out of it.

The development and implementation of such an automatic and robust procedure, including the previously discussed software package MARS, was a core part of this work.

To make an automatic procedure handling so many files failsafe the interaction with a database is mandatory. For the database server MySQL (www-12) was chosen. A database delivers the possibility to keep track of any step of the analysis. Having an appropriate Web Interface available the status of any step of the analysis chain can thus be monitored directly by the end-user.

The working automation turned out to be essential to be able pre-analyzing this huge amount of data and get hints about which of the data should be analyzed more carefully or at least cross-checked. Not only the presented source 1ES 1218+304 but also the detection of the second new AGN PG 1553+113 has been carried out the first time by the automatic analysis. Thus automatic data processing emerged to be an important basis of todays IACT experiments.

The single steps of the automatic analysis chain will be presented in the following paragraphs:

5.1. Data selection

An example for the data grouping scheme as described hereafter is shown in figure 5.1.

Run Information Information about each run is stored into ASCII files by the *Central Control* steering the full telescope system. These files are transfered automatically each day to the datacenter, where the information is filled into a run database.

Exclusions and Sequences Based on the preliminary information some runs are previously excluded from the analysis (e.g. runs flagged as test-runs). Taking into account the order of the runs, data files are grouped together with pedestal and calibration runs to *Sequences*. For a successful grouping the same environmental condition are required. With this new information a sequence database is filled.

Datasets As soon as the first analysis steps discussed afterward are finished, all sequences are checked for their quality parameters determined. Sequences of good quality which belong to the same observation target are grouped together to so-called *Datasets*. Since this is the main step ensuring the quality of the final analysis, it is always cross-checked manually. In the case of on-/off-observations off-data has to be selected, which can be done by a semi-automatic procedure suggesting the sequences best matching the requirements and cross-checked manually. Based on this datasets final results are calculated. Datasets need not be exclusive, i.e. the same sequence can belong to more than one dataset.

Automation To group the sequences together only run information from the data acquisition system is used. Thus this step can be done without the data itself being physically available. As soon as the data has arrived in the datacenter the analysis chain is invoked without any further interaction.

This analysis chain is outlined in the following.

5.2. Analysis chain

Calibration In a first step sequences are calibrated with a program called CALLISTO. While in a first loop the calibration constants are calculated, in a second step the data files are calibrated applying these constants. The success and further results of the calibration (e.g. mean calibration constants, number of bad pixels, etc.) are filled into a database. This information can be used for further excluding sequences from the following analysis or as a source of information about each sequence for the end user.

Image parameters Having successfully calibrated the data the calculation of image parameters by a program called STAR is started. In this step important parameters as the mean rate after cleaning or the muon rate is computed.

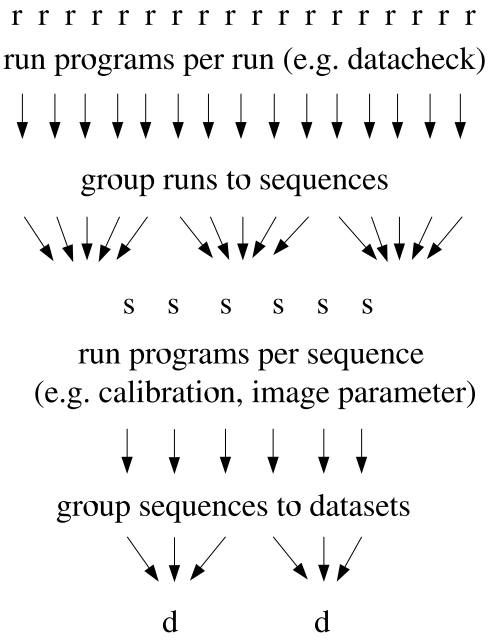

Figure 5.1.: Sketch of grouping runs to sequences and sequences to datasets, representing the final set of data analyzed.

The results and possible error codes are stored in the database.

Background Suppression Having created the image parameters successfully, the background suppression is done with a program called GANYMED fed by the datasets. The final result (significance, excess events, etc.) is now available together with the corresponding plot and can be checked by the end user. In addition these results and possible error codes are stored in the database, allowing everybody to check for possible new detections easily.

5.3. Database

The database can be queried from root-macros or optionally from a web-interface. Already the simple web-interface makes it possible to restrict the result to a given time-interval, sort the result by a single column or group data of equal parameters together. Grouping data together allows to get numbers as the total observation time for one observed source position and given time interval. Each column is requested on-demand, which grants compiling a table with the relevant information only.

Cross-links allow the direct access, for example, of the sequence a run is assigned to. Special interfaces permit to request run-specific information of all runs belonging to one sequence and the corresponding data-check plots produced in each analysis step. With these plots it is easy to judge the data quality in case of uncertainties.

Having a huge set of parameters describing the quality of the data and the quality of the result of each analysis step, e.g. the calibration, allows easy judging the usability of all data. Especially the selection of suitable off-data for a set of on-data is simplified by another specialized web-interface, which makes it possible to restrict the range of values allowed for several quality parameters.

In three tables the all quality parameters available for the sequences used for the analysis discussed hereafter are given in appendix A.

In addition to the quality parameters the database contains at any time a snapshot of the current processing status of all data, which is also the initiator of each processing step. Thus the steering of the automation is completely done through the database, e.g. reprocessing some particular data is done be resetting their corresponding database entries. This makes control of the automation and processing simple and robust enough, that an undefined number of clones of this system can be used for test purposes. Such the behavior of new developments, as new analysis algorithms, can be tested on all available data easily and independent from the production. This is of great advantage judging the quality of new algorithms and improves the speed and reliability of new developments.

By monitoring the processing status, including possible error codes, problems in the automation or the precessing itself can easily be identified. If all data or parts of the data shall be reprocessed it allows keeping track of the processing and the software version used for each processing step.

6. Results

It doesn't matter how beautiful your theory is,
it doesn't matter how smart you are.
If it doesn't agree with experiment,
it's wrong.

— Richard Feynman.

After the signal has been discovered by the automatic analysis with preliminary off-data a more refined analysis has been done and a spectrum has been calculated. Therefore especially the matching of the off-data sample has been improved.

6.1. Dataset

In table 6.2 (at the end of the chapter) a list of the sequences used for the final analysis of the 1ES 1218+304 observation is shown. All available on-data is listed, discarded data is marked with parentheses. The off-data was chosen taking all available quality parameters into account. The main criteria were comparable mean Pedestal-RMS, mean Arrival-Time-RMS, the PSF, the absolute muon calibration and the muon rate as derived from the muon analysis and the weather conditions.

6.2. Significance of the detection

The analysis performed on the dataset as explained in the previous chapters leads to a significance of 6.4 standard deviations, according to Li and Ma 1983 (equation 17), for emission from the position of 1ES 1218+304. In an effective observation time of 8.2 h a total of 560 excess events on top of 3308 background events have been detected. The data was taken between 9^{th} and 15^{th} January 2004 at zenith angles between 1° and 13°. The off-data has been scaled with a factor of 1.2 to match the on-data in the off-source region. The corresponding ϑ^2-plot for an analysis threshold, of $\sim$140 GeV, defined as the peak-energy of the event-distribution after all cuts, is shown in figure 6.1.

6.3. Sky map

For background subtraction a histogram of reconstructed shower origins is filled in camera coordinates from the off-data. The resulting distribution is equivalent to a measurement of the camera acceptance.

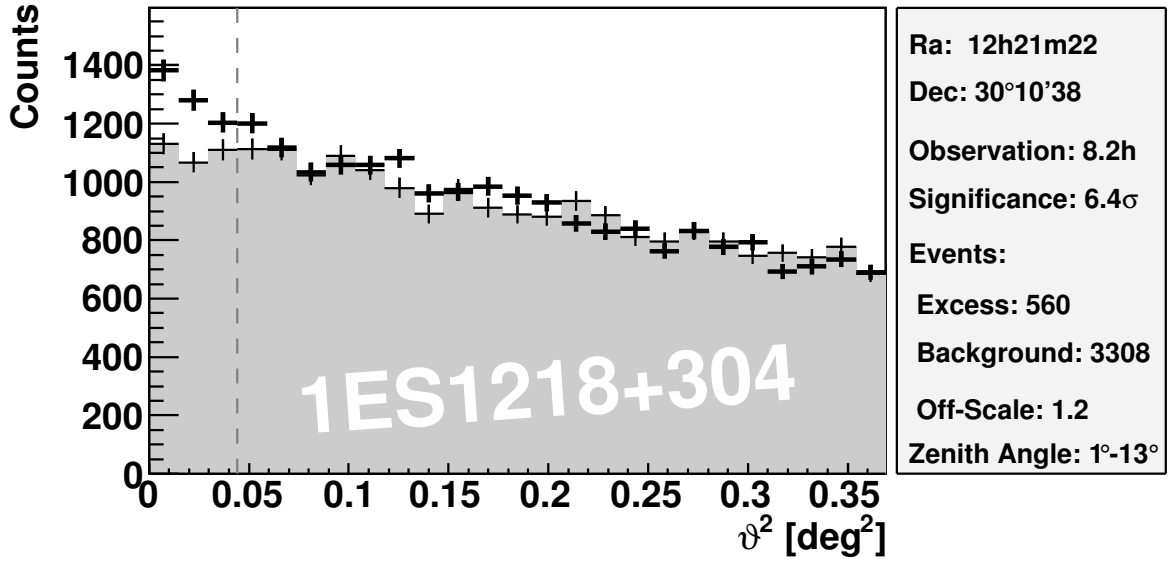

Figure 6.1.: ϑ^2-plot for the detection of the source 1ES 1218+304 yielding a significance of 6.4 standard deviations with 560 excess events on top of 3308 background events for an on-observation of 8.2 h. The dashed line shows the ϑ^2-cut. The off-data (gray shaded) has been scaled with a factor of 1.2 to match the on-data in the off-source region.

For the on-data the reconstructed shower origins are projected into a celestial coordinate system. An additional histogram is now filled with the camera acceptance determined from the off-data projected into the same celestial grid. The result is equivalent to the telescope acceptance on the sky. With an appropriate scaling it can no be subtracted as off measurement from the on-data. For this purpose it is scaled to match the on-data by the number of events between 0.325° and 0.475°. For convenience each event filled into the histograms is replaced by a two dimensional Gaussian with a width of 0.06° corresponding to half of the point spread function, with which a point-like gamma-ray source would be reconstructed. The result for the sky region around 1ES 1218+304 is shown in figure 6.2 (left). The position of its maximum is well within the systematic tracking accuracy in January 2004 as reported in section 2.1.5. Figure 6.2 (right) shows the distribution of entries in the sky map for an analysis threshold of $\sim$140 GeV. A clear deviation from a Gaussian to positive values can be seen.

6.4. Lightcurve

To measure the variability of the source the sample has been divided into six subsamples on a day-by-day basis. The analysis of the data has been carried out as described in chapter 4 except that only a single spectral point for E $>$ 100 GeV has been calculated. The result, shown in figure 6.3,

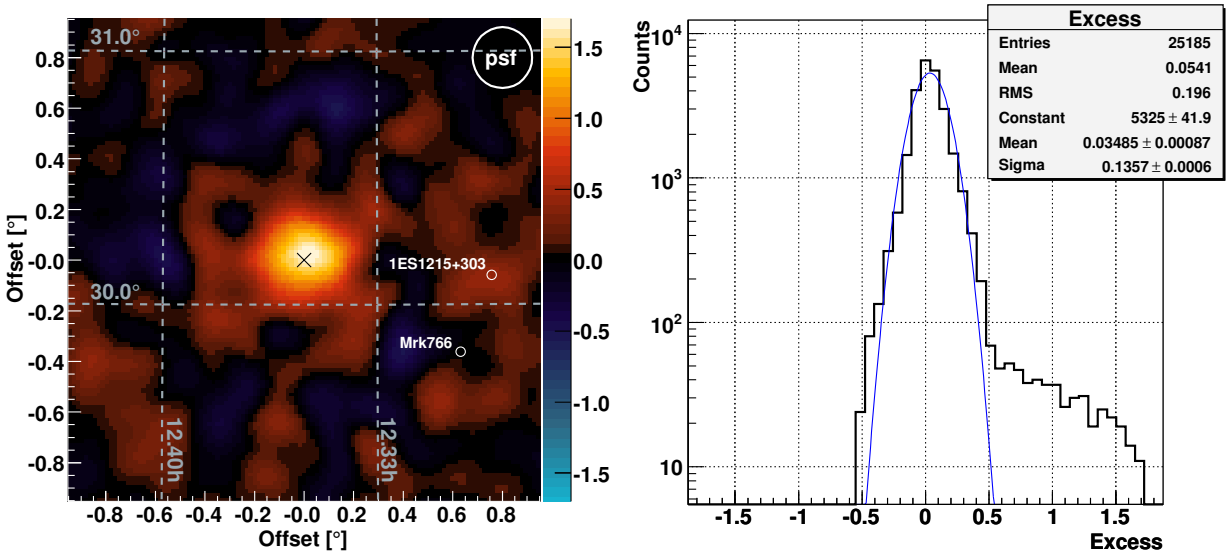

Figure 6.2.: Left: Background subtracted distribution (left) of excess events in sky coordinates (dashed lines) and its distribution (right). The color code denotes units of 10 events/arcmin^2. The center (black cross) corresponds to the nominal position of 1ES 1218+304. The distribution is consistent with the point-spread function shown and its peak is well inside the systematic pointing uncertainty. The two other X-ray sources in the field-of-view are on the map. The distribution of excess events shows a clear deviation from the Gaussian (blue line) background to positive excess values.

for an analysis threshold of ∼120 GeV, is consistent ($\chi^2/ndf = 2.4/5$) with a constant flux of

$$F(> 100\,\mathrm{GeV}) = \frac{(8.7 \pm 1.4) \cdot 10^{-7}}{\mathrm{s} \cdot \mathrm{m}^2} \tag{6.1}$$

6.5. Measured spectrum

The measured spectrum obtained, see figure 6.4, is compatible ($\chi^2/ndf = 1.1/4$) with a power law of

$$F_E(E) = \frac{(1.5 \pm 0.8) \cdot 10^{-8}}{\mathrm{s} \cdot \mathrm{m}^2 \cdot \mathrm{TeV}} \left(\frac{E}{\mathrm{TeV}}\right)^{-(3.0 \pm 0.4)} \tag{6.2}$$

corresponding to

$$F_E(E) = \frac{(8.1 \pm 2.1) \cdot 10^{-7}}{\mathrm{s} \cdot \mathrm{m}^2 \cdot \mathrm{TeV}} \left(\frac{E}{250\,\mathrm{GeV}}\right)^{-(3.0 \pm 0.4)} \tag{6.3}$$

For convenience the spectral points are also shown in table 6.1.

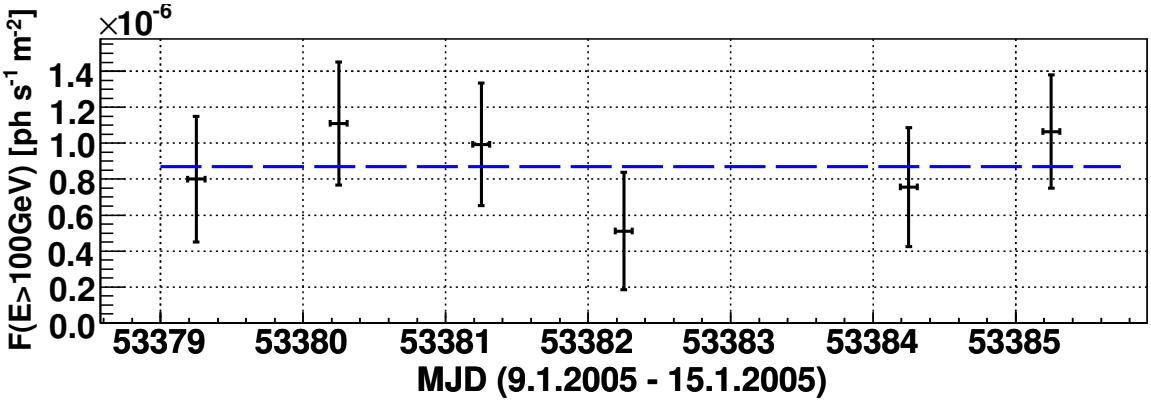

Figure 6.3.: Integral flux above 100 GeV of the source 1ES 1218+304 versus Modified Julian Date measured with the MAGIC-telescope. The total sample has been divided into six sub-samples with observations times in the order of ∼80 min, one day each. The lightcurve is consistent with a constant flux (blue line) within the errors.

The error bars corresponding to one standard deviation show the statistical uncertainty only. Two data points with a significance around unity have been replaced by upper limits at a confidence level of 99%, which was calculated using the algorithm by Feldman and Cousins, 1998. The gray shaded region shows the size of the systematic error resulting from the analysis. The total systematic error for the spectral slope is estimated to be ∼0.3. Additional systematics for the flux level are estimated to be in the order of ∼40%. The main contributions are uncertainties of the atmospheric conditions, the mirror reflectivity and the quantum efficiency of the PMT.

To determine a spectrum from observational data and the corresponding Monte Carlo based estimations for the efficiency the background suppression has to be done such that the slope of the efficiency curve is not too steep. This is normally achieved by loosening the background suppression cuts until the cut efficiency for Monte Carlo gammas is well above 50%. Especially for the lowest energy bins this condition can not easily been fulfilled and the resulting spectrum may still depend on the cuts used. Therefore a couple of different cuts have been carried out. The result is shown as systematic error.

Also the input spectra of the Monte Carlo sample can influence the result. As the measured spectrum can only be determined within the errors, a couple of other spectra allowed by the errors were fed into the analysis and the results were added to the systematic error.

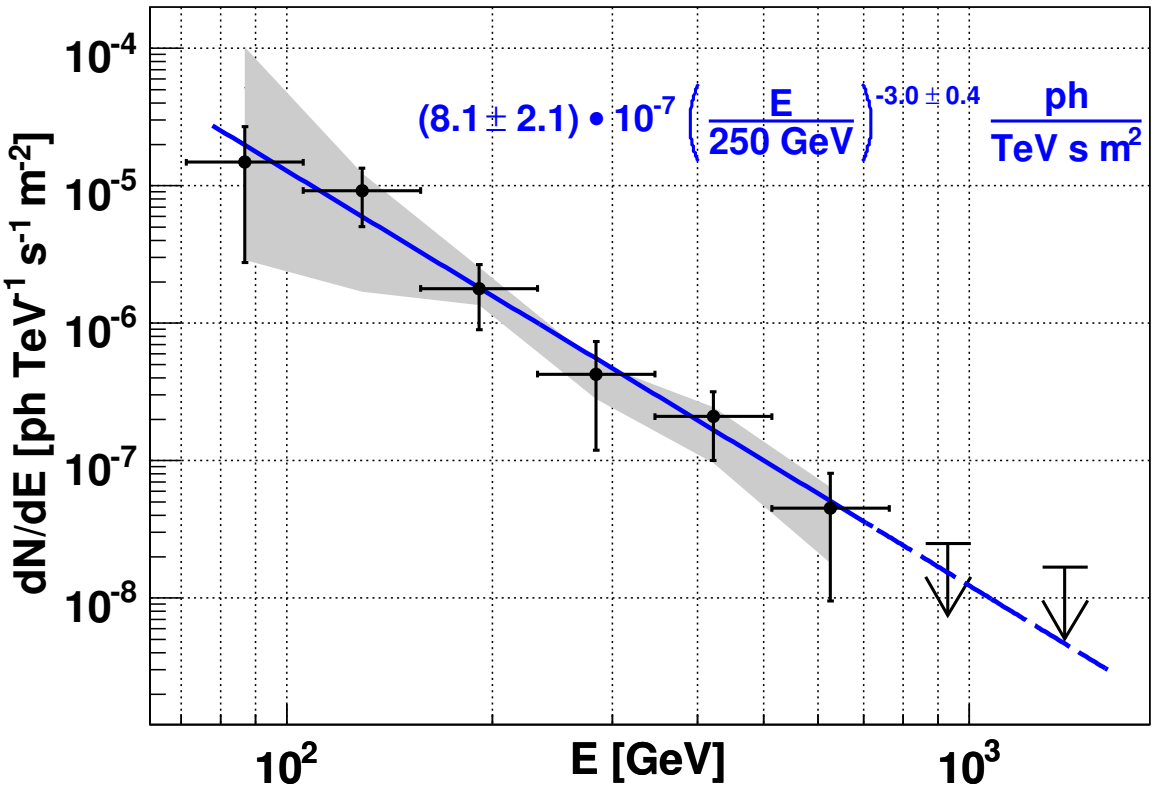

Figure 6.4.: Differential spectrum for 1ES 1218+304 measured with the MAGIC-telescope. The best powerlaw fit to the spectrum between 80 GeV and 700 GeV is shown as blue line. The gray shaded region corresponds to the systematic error originating from analyses with different cut efficiencies and simulated spectra.

Energy / GeV	$F_E(E)$ / TeV^{-1} m^{-2} s^{-1}
87	$(1.5 \pm 1.2 \pm 4.9) \cdot 10^{-5}$
130	$(9.2 \pm 4.2 \pm 5.2) \cdot 10^{-6}$
190	$(1.8 \pm 0.9 \pm 0.4) \cdot 10^{-6}$
280	$(4.3 \pm 3.1 \pm 1.4) \cdot 10^{-7}$
420	$(2.1 \pm 1.1 \pm 0.7) \cdot 10^{-7}$
630	$(4.5 \pm 3.5 \pm 2.3) \cdot 10^{-8}$

Table 6.1.: Differential flux of 1ES 1218+304 with statistical and systematic error.

Type	Sequence Number	Start Time	Duration	Azimuth min	Azimuth max	Zenith Angle min	Zenith Angle max
On	47736	2005-01-09 05:30:28	18.27 min	76°	79°	6°	10°
On	47744	2005-01-09 05:49:49	48.70 min	-74°	75°	1°	6°
On	47955	2005-01-10 05:28:46	70.95 min	-76°	79°	1°	9°
On	48170	2005-01-11 05:11:39	5.93 min	80°	80°	11°	12°
On	48174	2005-01-11 05:18:38	80.15 min	-77°	80°	1°	11°
On	48405	2005-01-12 05:10:46	87.78 min	-78°	80°	1°	11°
On	[49018]	2005-01-14 05:09:21	5.83 min	79°	79°	9°	10°
On	49022	2005-01-14 05:16:11	83.42 min	-79°	78°	1°	10°
On	49196	2005-01-15 04:59:22	19.93 min	77°	80°	8°	11°
On	49205	2005-01-15 05:20:51	22.78 min	52°	76°	2°	7°
On	49216	2005-01-15 05:45:40	55.02 min	-80°	41°	1°	11°
On	(49884)	2005-03-12 01:58:32	19.90 min	-41°	58°	1°	3°
On	(49893)	2005-03-12 02:20:27	57.02 min	-80°	-56°	2°	15°
On	{50072}	2005-03-15 00:52:49	16.02 min	80°	80°	11°	15°
On	{50079}	2005-03-15 01:10:40	33.52 min	59°	80°	3°	10°
Off	47667	2005-01-09 01:38:36	35.10 min	109°	12°	12°	22°
Off	47684	2005-01-09 02:17:15	29.03 min	126°	151°	10°	14°
Off	47698	2005-01-09 02:48:50	29.58 min	155°	197°	9°	10°
Off	47988	2005-01-10 19:55:26	96.15 min	112°	193°	10°	22°
Off	48216	2005-01-11 20:18:16	67.87 min	132°	211°	10°	14°
Off	48246	2005-01-11 21:40:25	59.05 min	92°	115°	5°	19°
Off	48275	2005-01-11 22:45:18	52.22 min	131°	252°	3°	9°
Off	48298	2005-01-11 23:41:19	15.45 min	253°	258°	9°	12°
Off	48305	2005-01-11 23:57:48	38.93 min	259°	267°	12°	21°

Table 6.2.: $1.1 \cdot 10^7$ events have been recorded in 15 sequences at Zenith Angles between 1° and 15° in a total observation time of 10.4 h. The sequences marked with ()-parentheses were excluded, due to a misfocused mirror, the sequences marked with {}-parentheses due to malfunctioning of the calibration system and the sequence marked with []-parentheses was omitted due to a failed effective on-time fit.

7. Intrinsic spectrum

The measured spectrum can be altered by processes taking place between the emitter and the observer, becoming more and more important on cosmical length scales. This effect could be the reason that the total number of Blazars, known to emit gamma-rays, reported in the literature as of February 2006 amounts to 11, while the number of high-confidence Blazars in the 3^{rd} EGRET catalog is 66 (Hartman et al., 1999).

A likely explanation for this difference is the attenuation of gamma-rays due to photon-photon interactions with low energy photons from the extragalactic background radiation as pointed out by Stecker et al., 1992. This is in agreement with the fact that all Blazars detected so far above 350 GeV are rather nearby as predicted by correlation between the gamma-ray attenuation and the redshift of the source, known as *Fazio-Stecker relation*, see Fazio and Stecker (1979); Kneiske et al. (2004).

Taking this attenuation into account the spectrum intrinsically emitted by the source can be calculated from the measured spectrum and consequently used to understand the physics processes taking place at the emission region.

The alteration of the spectrum along the line of sight and the results for the intrinsic spectrum of 1ES 1218+304 is discussed hereafter.

7.1. Basic principle

The attenuation depends on the line of sight integral of the evolving density of low energy photons in the universe, i.e. on the history of the diffuse, isotropic radiation field.

Provided the threshold energy for pair production is exceeded, low energy photons γ_{LE} and high energy gamma-rays γ_{HE} can produce electron-positron pairs:

$$\gamma_{HE} + \gamma_{LE} \longrightarrow e^+ + e^- \tag{7.1}$$

The low energy photons are mainly from optical galaxies (star light), absorbed and reemitted by interstellar dust, and obscured luminous and ultra-luminous infrared galaxies (LIG/ULIG). At wavelengths longer than $\sim$200 μm they are dominated by the 2.7 K cosmic microwave background.

If the energy of one of the interacting particles is known, the minimum wavelength of the other particle can be concluded using the condition for the pair production threshold:

$$E_{HE} \cdot E_{LE} = E_{e^+} \cdot E_{e^-} = 2 \cdot (m_e c^2)^2 \gtrsim 2.6 \cdot 10^{11} \mathrm{eV}^2 \tag{7.2}$$

To be able to infer the intrinsic spectrum emitted by a cosmic source, the consequent flux attenuation must be taken into account, i.e. the measured spectrum must be corrected for the flux attenuation function.

This function is computed from the evolving extragalactic background light (EBL), the so-called Metagalactic Radiation Field (MRF). Since the EBL of past times cannot be measured directly a model describing its evolution is mandatory. On the other hand employing a predictive model for the emitted high energy spectra of AGN, measurements of their spectra would constrain MRF models. Alternatively, lacking such predictive models the effects of the intrinsic spectra and the MRF must be distinguished on a statistical basis. Currently there are only a few AGN known to be bright-enough gamma ray emitters so that there spectra could be determined; furthermore most of them are nearby (at relatively low redshifts $z < 0.1$). The low energy threshold and high sensitivity of the MAGIC-telescope promises the discovery of more sources at higher redshifts as 1ES 1218+304 (Elvis et al., 1992; Urry et al., 2000) at $z = 0.182$ (Véron-Cetty and Véron, 2003; Sbarufatti et al., 2005).

With an increasing number of detections at redshifts higher $z > 0.2$ it would be possible to disentangle the shape of the source spectra itself and the flux attenuation due to the discussed pair production. This could consequently lead to a determination of the MRF. Due to the low number of sources detected so far in the gamma-ray energies a satisfying determination of the MRF is still not possible. Therefore unfolding a source spectrum from the influence of the MRF still relies on theoretical or empirical models for the MRF. A semi-empirical model (Kneiske et al., 2002, 2004) based on stellar light produced and reprocessed in evolving galaxies will be discussed now. A review of different models can be found in Hauser and Dwek, 2001.

7.2. Metagalactic radiation field

To compile the MRF the contributions to the photon density at any time must be known. This photon density is a direct result of the homogeneous cosmic microwave background and the inhomogeneous distribution of point like sources homogeneously distributed in space. Assuming that their luminosity evolution is independent of their absolute creation time their resulting photon density is well described by the formation rate of these sources and their luminosity evolution.

As star formation is an ongoing process with relatively short time scales of 10^5 years to 10^7 years, the star-burst spectra can be convolved directly with the global star formation rate $\dot{\tilde{\rho}}_*(t) = \dot{\rho}_*(z)$ per comoving unit volume to derive the global luminosity density (comoving emissivity) due to cosmic star formation.

With the temporal luminosity evolution $L_\nu(t)$ the luminosity density at cosmic epoch t is obtained as

$$\varepsilon_\nu(t) = \int_t^{t_m} L_\nu\,(t - t') \cdot \dot{\tilde{\rho}}_*(t')\,dt' \tag{7.3}$$

Rewriting this equation on terms of redshift, $z = z(t)$, for a star formation which began at a finite

epoch $z_m = z(t_m)$ yields

$$\varepsilon_\nu(z) = \int_z^{z_m} L_\nu \left(t(z) - t(z')\right) \cdot \dot{\rho}_*(z') \left| \frac{dt'}{dz'} \right| dz' \tag{7.4}$$

Integrating this evolution of the emissivity over redshift returns the energy density and, after unit transformation, the comoving power spectrum of the MRF

$$P_\nu(z) = \nu I_\nu(z) = \nu \frac{c}{4\pi} \int_z^{z_m} \varepsilon_{\nu'}(z') \left| \frac{dt'}{dz'} \right| dz' \qquad \text{with} \qquad \nu' = \nu \frac{1+z'}{1+z} \tag{7.5}$$

Cosmological parameters, Ω_r, Ω_R, Ω and Ω_Λ enter through dt/dz, which is given by, e.g. Peebles 1983

$$\left| \frac{dt}{dz} \right| = \frac{1}{H_0 \left(1+z\right) E(z)} \tag{7.6}$$

with an *equation of state*

$$E(z)^2 \; = \; \Omega_r (1+z)^4 \; + \; \Omega (1+z)^3 \; + \; \Omega_R (1+z)^2 \; + \; \Omega_\Lambda \tag{7.7}$$

With the critical density ρ_c of the universe

$$\rho_c = \frac{3H_0^2}{8\pi G} = 10.54 h^2 \, \frac{\text{keV}}{\text{cm}^3} \tag{7.8}$$

and u_r the relativistic energy density, the density of contributions from relativistic components Ω_r (such as the cosmic microwave background or star light) can be defined as

$$\Omega_r = \frac{u_r}{c^2 \rho_c} \tag{7.9}$$

7.2.1. Parameters

Being able to calculate the MRF from the star formation rate and the luminosity evolution, and given the difficulties in determining the MRF from direct measurements, both must be modeled. This models can subsequently be constraint by direct measurements of their ingredients.

A precise description of the semi-empirical models used hereafter is given in Kneiske et al. (2002, 2004). These models are based on interpolating measurements and can be interpreted as upper and lower limits, depending on the choice of the parameters, e.g. metalicity, emissivity and the dust temperatures. For the following considerations the highest and lowest model is used.

7.2.2. Optical depth, Unfolding

To unfold a measured spectrum of a source at redshift z_0 and an observed energy E_0, with the mentioned MRF-model, the optical depth τ is calculated from the cosmological line element

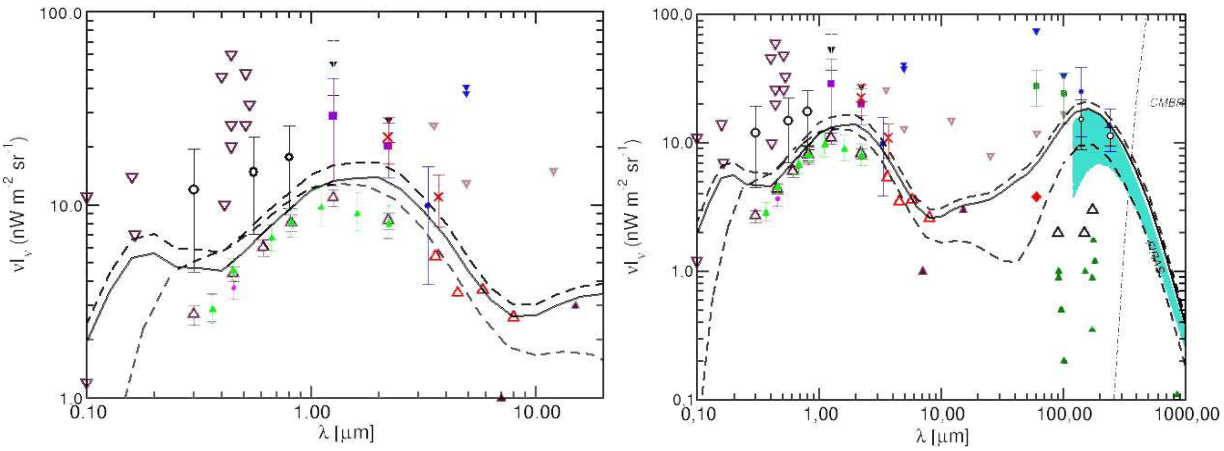

Figure 7.1.: Both plots show the best-fit model for the extragalactic background light as solid line. The upper and lower limit models as used in this thesis are shown as dashed lines. The left plot shows the left part of the right plot zoomed in. The symbols show direct and indirect measurements, upper and lower limits. A detailed description of these measurements can be found in Kneiske, 2004.

dl/dz', the angle θ between the interacting photons with $\mu = cos\,\theta$, the number density $n(z, \varepsilon)$ of the photons of the metagalactic radiation field as a function of redshift z and photon energy ϵ, and the $\gamma\gamma$-pair production cross-section $\sigma_{\gamma\gamma}$:

$$\tau_{\gamma\gamma}(E_0, z_0) = c \int_0^{z_0} \int_0^{2} \int_{\epsilon_{gr}}^{\infty} \frac{dl}{dz'} \frac{\mu}{2} \cdot n(z, \epsilon)\, \sigma_{\gamma\gamma}(E_0, \epsilon, \mu, z') \cdot d\epsilon\, d\mu\, dz' \tag{7.10}$$

The attenuation factor $1/f$ of gamma rays with energy E emitted at redshift z_0 follows from this equation.

$$f(E, z_0) = e^{\tau_{\gamma\gamma}(E, z_0)} \tag{7.11}$$

The intrinsic spectrum F_{int} of a source with known redshift can thus be calculated from the observed one F_{obs} by

$$F_{int}(E) = f(E, z_0) \cdot F_{obs}(E) \tag{7.12}$$

7.3. Intrinsic spectrum of 1ES 1218+304

The redshift of 1ES 1218+304 (Elvis et al., 1992; Urry et al., 2000) is given as $z = 0.182$ (Véron-Cetty and Véron, 2003; Sbarufatti et al., 2005). Consequently the influence of the flux attenuation discussed above has to be taken into account if the measured data should be interpreted in the context of AGN physics.

Result Unfolding the measured spectrum of 1ES 1218+304 with the highest and lowest MRF-model from Kneiske et al. (2004) yields the intrinsic spectra shown in figure 7.2, i.e. the spectra which would have been observed without pair-production along the line of sight. The gray shaded region and gray points are identical to the direct measurement of the spectrum as shown in section 6.5. The two intrinsic spectra can be interpreted as phenomenological upper (red) and lower (blue) limits.

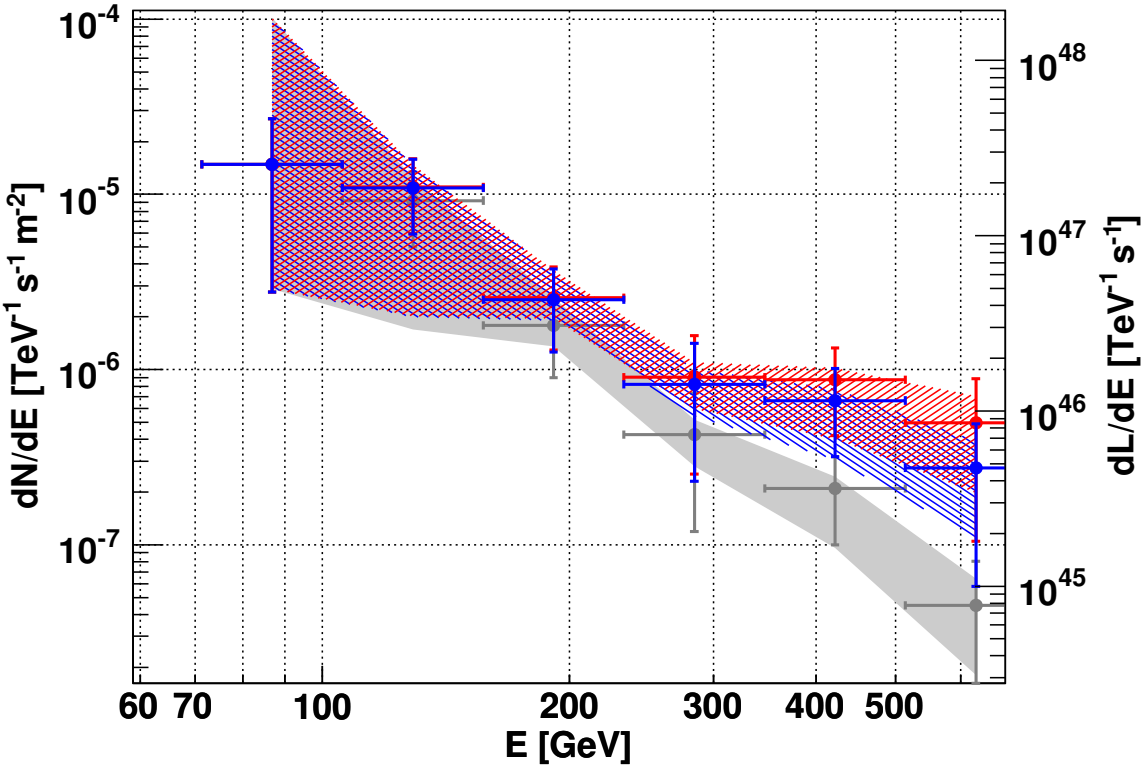

Figure 7.2.: The differential spectrum of 1ES 1218+304 versus energy. The spectrum as measured by the telescope (gray, same as in figure 6.4) and the intrinsic spectrum of the source corrected for a high MRF-model (red) and a low MRF-model (blue) as discussed in Kneiske et al., 2004. The right axis denotes the emission per unit energy and time, corrected for the distance assuming isotropic emission.

To make the representation of the spectrum completely independent of the distance to the observer the emitted energy must be corrected for the distance of the object. The redshift of $z = 0.182$ corresponds to a luminosity distance D_L of $\sim$1.2 Gpc, which is the distance taking the geometry of the universe into account. If not stated explicitly different, for easy comparison with older publications, a Hubble constant of $H_0 = 50$ km/s/Mpc and $q_0 = 0$ is assumed. (Newer measurements, e.g. Spergel et al. (2006), yield $H_0 \simeq 72$ km/s/Mpc) With the relation $L = 4\pi D_L^2 F$ between the intrinsic luminosity L and the luminosity density D_L the measured flux F can be converted into the emitted luminosity, assuming isotropic emission. For 1ES 1218+304 this yields a conversion factor of $\sim 1.7 \cdot 10^{56}$ cm^2 (figure 7.2, right axis). The Doppler shift of

$1+z$ of the frequencies, also known as K-correction, e.g. Schmidt and Green (1986); Hogg et al. (2002), can be neglected compared to more than ten orders of magnitude which is the energy range AGN are supposed to emit radiation.

Discussion Fitting a pure power-law to the unfolded spectra leads to a spectral slope in the order of 2.0-2.2 with a $\chi^2/ndf \simeq 1.7/3$. If the 87 GeV point is omitted due to its high systematic uncertainty and the last two points are considered upper limits due to their possible overestimation discussed in section 4.9.3, the fitted power-law yields a spectral index of $\sim$3.9 before unfolding and $\sim$3.2 to $\sim$3.3 after unfolding with the optical depth for pair production.

However, as a cutoff due to pair-creation along the line of sight is expected around 400 GeV (discussed previously), and a peak is expected around $\lesssim$ 100 GeV (discussed later), a power-law might not describe the spectrum well even if it is compatible with a power-law fit within its statistical and systematic errors.

8. Active Galactic Nuclei

Black holes are where God divided by zero.
— Stephen W. Hawking.

Since the discovery of the first Quasar (Quasi Stellar Object) 1963 by Schmidt extremely high luminosities, emitted from compact extragalactic objects over a wide range of frequencies from the radio to gamma-rays, became a well established phenomenon.

If one of the following conditions are fulfilled these extragalactic object (galaxies) are called Active Galactic Nuclei (AGN):

- non-thermal continuum emission with broad emission lines
- brighter than *normal* galaxies at all frequencies
- polarized radiation
- variability of their properties
- radio lobes and/or jets
- point-like and compact core

Explaining the high luminosities, the non-thermal spectra and the high photon energies requires to consider other physical processes than nuclear fusion powering stars.

Since measurements of different objects showed a variety of spectral properties as by orders of magnitude different peak luminosities, or different line emission, these objects were previously classified by their spectral properties and therefrom thought to be different object classes.

Newer measurements could reverse this impression revealing properties that are continuous in their characteristics. This suggests that the observed objects are of the same type, and the physical processes observed are the same.

Different models for a unifying explanation have been proposed. Currently the most widely accepted model is that all these objects are the same class of object but observed from different directions (Browne, 1983; Wardle et al., 1984; Ghisellini and Maraschi, 1989; Urry and Padovani, 1995), but also show intrinsic differences w.r.t. radio emission (Padovani and Giommi, 1995).

Due to their high luminosity AGN are the best candidates to probe properties of our universe at large distances.

To sort out the meaning of the measured spectrum of 1ES 1218+304 for the emission processes taking place in AGN the underlying physics of these objects is outlined hereafter.

8.1. Overview

For completeness the earlier classification, which lead to the common names used for AGN with different emission properties, is touched and leads over to a commonly accepted unified scheme.

8.1.1. Classification

Earlier classification

Besides classifying AGN according to their spectral lines in the optical, they can also be classified by their radio-loudness. Roughly 15%-20% of AGN are radio-loud, meaning that their radio flux at 5 GHz F_5 is more than ten times higher than the flux in the optical B-Band F_B (Kellermann et al., 1989):

$$F_5 \gtrsim 10 \cdot F_B \tag{8.1}$$

This fraction increases with increasing optical (Padovani, 1993; La Franca et al., 1994) and X-ray (della Ceca et al., 1994) luminosities.

AGN with bright continua and broad emission lines from hot, high-velocity gas are referred to as *Type-1* AGN, whereas those with weak continua and narrow emission lines are called *Type-2* AGN. In the radio quite case they are known as Seyfert I and Seyfert II type galaxies mostly hosted in spiral galaxies (Sarajedini et al., 1999). This can be explained by the absence of the high-velocity gas as in *Type-1* AGN or by a big wall of absorbing material along the line of sight (Krull, 1997). Table 8.1 shows the different names assigned to AGN ordered by their radio-loudness and emission line widths. For a tree-like scheme see also Dermer, 1994.

Radio-loud AGN, showing unusual spectral characteristics (e.g. no emission lines), are called *Blazars* (in the table referred to as *Type-0* AGN). The spectrum of this population lacks strong emission or absorption features with typical equivalent width limits of $W_\lambda < 5\,\text{Å}$. In some cases also very broad P-Cygni-like absorption lines have been observed. In addition to this non-thermal emission Blazars are characterized by rapid variability and superluminal velocities of their radio cores.

	Type 2 (narrow line)	Type 1 (broad line)	Type 0 (unusual)
Radio quiet	Seyfert 2	Seyfert 1	
	NELG		
	IR Quasar	QSO	BAL QSO
Radio loud	FR I (NLRG) (Fanaroff and Riley, 1974)	BLRG	BL Lac (Blazar)
		SSRQ	
	FR II (NLRG) (Fanaroff and Riley, 1974)	FSRQ	FSRQ (Blazar)

Table 8.1.: Classical classification of Active Galactic Nuclei adopted from Lawrence (1987), ordered horizontally by their emission line properties and vertically by radio-loudness.

A unified model

New observations lead to unifying models, e.g. Rowan-Robinson (1977); Lawrence (1987); Antonucci and Ulvestad (1985) implying that the observed characteristics are dominated by different random inclinations of the object w.r.t. the observer rather than different physical properties. For reviews see Antonucci, 1993; Urry and Padovani, 1995.

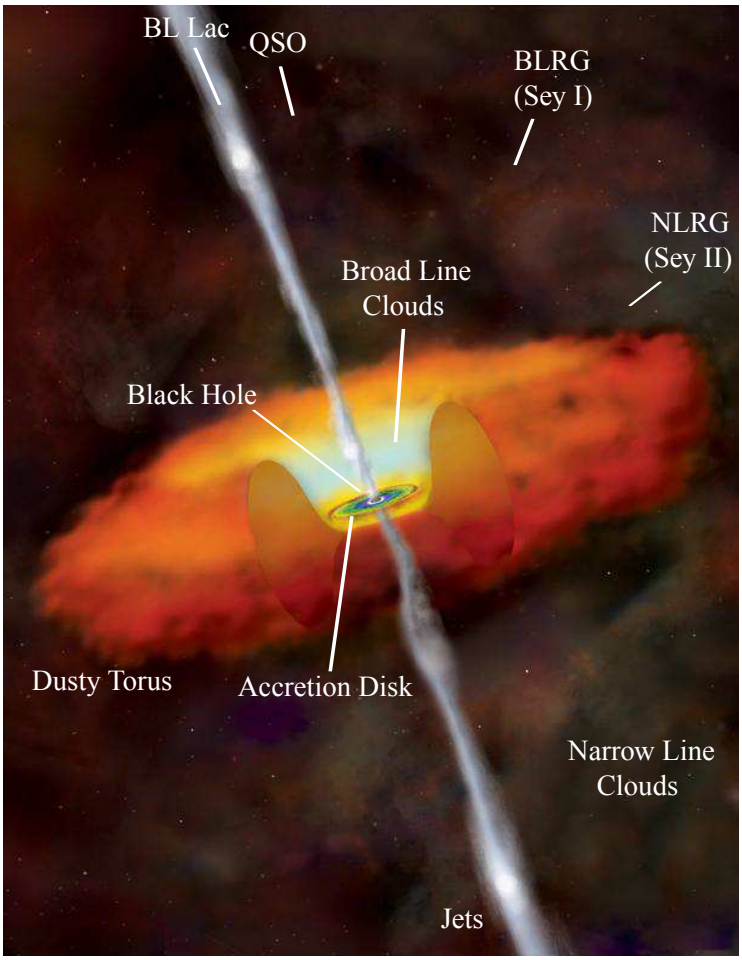

Figure 8.1.: Illustration of an Active Galactic Nucleus and its environment (www-13). The measured spectral characteristic depends on the observation direction. The names in parentheses denote the names in the radio-quite case, i.e. without a jet.

With this unified model, shown in figure 8.1, all types of known AGN can be reduced to a single class of objects. In the center of a host galaxy, a super-massive black hole of typically $10^7 M_\odot - 10^9 M_\odot$ is the central engine and its ultimate source of power, e.g. due to its high gravitational potential energy released in a viscous accretion disk (Shakura and Sunyaev, 1973) or loss of rotational energy by the Blandford-Znajek mechanism or both. Surrounding the central black hole a luminous accretion disk is formed by accreted interstellar gas and objects shattered

by the extreme gravitational impact. In hot clouds of gas orbiting the accretion disk broad optical and ultraviolet emission lines are produced. Also the disk itself may produce them. This emission region is called *broad-line region* (BLR).

Depending on the viewing direction this broad-line emission can be obscured by a thick dusty torus (Pier and Krolik, 1992, 1993) or warped disk (Sanders et al., 1989), preventing infrared to ultraviolet light from penetrating (Rowan-Robinson, 1977). Despite of that hot electrons pervading this region can scatter some continuum or broad-line emission into those lines of sight. Clouds much farther away from the central source produce narrow emission lines.

Radio emitting jets emanate mass from the region near the black hole, initially at relativistic speeds. Due to high temperatures at the source of the mass outflows the gas is ionized (plasma). Because of the movement of the charged particles, magnetic fields are produced and frozen in the mass outflow of infinite conductivity. The magnetic field is responsible for collimating the jet to small opening angles ($< 5°$) along distances much longer than the jet diameter. The jets may form giant radio sources in the case of elliptical host galaxies or weak radio sources in the case of gas-rich spiral host galaxies. AGN with the jet along the line of sight are called Optically Violent Variables (OVV) or BL-Lacertae (BL-Lac) type objects. Objects with the line of sight beneath the jet are called radio-loud Quasi Stellar Objects (QSO) or without a jet radio-quite QSO.

The classification previously done by observational characteristics turns into a two parameter description, namely (1) the angle between the line of sight and the rotation axis of the black hole and (2) the luminosity discriminating between radio-loud and radio-quite objects. The old and new characterization can be compared by table 8.1 and figure 8.1.

Typical length scales For a $10^8 M_\odot$ black hole, the Schwarzschild radius is $\sim 3{\cdot}10^{13}$ cm $\simeq 3.2{\cdot}10^{-6}$ pc, the accretion disk emits mostly from $\sim$(1-30)$\cdot 10^{14}$ cm $\simeq$(3.2-97)$\cdot 10^{-5}$ pc, the broad-line clouds are located within $\sim$(2-20)$\cdot 10^{16}$ cm $\simeq$(6.5-65)$\cdot 10^{-3}$ pc of the black hole, and the inner radius of the dusty torus is perhaps $\sim 10^{17}$ cm $\simeq 3.2{\cdot}10^{-2}$ pc. The narrow-line region extends approximately from $\sim 10^{18}$ cm to 10^{20} cm $\sim$0.3 pc to 30 pc, and radio jets have been detected on scales from 10^{17} cm $\simeq 3{\cdot}10^{-2}$ pc to several times 10^{24} cm $\simeq$100 kpc, which is a factor of ten larger than the largest galaxies.

The typical length scales and their corresponding light travel times, giving a lower limit for time variability, are also shown in table 8.2.

8.1.2. AGN jets

According to this unified AGN model (Urry and Padovani, 1995) Blazars and BL-Lacertae type object are radio galaxies with jets closely aligned with the line of sight. Jets are mass outflows from the accretion disk along the spin axis of the black hole.

	extension/cm	extension/pc	light travel time
Black hole radius	$\sim 3{\cdot}10^{13}$	$\sim 3.2{\cdot}10^{-6}$	~ 5 min
Accretion disk emits mostly from	$(1-30)\cdot 10^{14}$	$(3.2-97)\cdot 10^{-5}$	1 h - 1 d
Broad line clouds located within	$(2-20)\cdot 10^{16}$	$(6.5-65)\cdot 10^{-3}$	1 w - 10 w
Inner radius of dusty torus	$\sim 10^{17}$	$\sim 3.2{\cdot}10^{-2}$	~ 5 w
Narrow line region	$\sim 10^{18}$-10^{20}	$\sim$0.3-30	~ 1 y - 10 y
Known Radio jet extensions	10^{17}-10^{24}	0.03-100.000	5 w - 30,000 y

Table 8.2.: Typical length scales of an Active Galactic Nucleus of $10^8 M_\odot$. for convenience the length scales are given in units of cm, pc and the corresponding light travel time giving a lower limit on variability time-scales.

8.1.3. Jet origin

The matter accreted by the black hole's high gravitational force is shattered into dust and gas. This material is rotating around the black hole in a plane perpendicular to the rotation axis of the black hole. Normally it is assumed that the disk is Keplerian, which means, that it is existing due to the balance between the centrifugal force of the rotating matter and the black holes gravitational force.

The process of extracting mass from the accretion disk is not yet known and still under discussion. A electron-positron origin from vacuum discharge (*Blandford-Znajek Poynting flux*; Blandford and Znajek, 1977) has been suggested by Blandford and Levinson, 1995. Also an electron-proton origin from the accretion disk seems to be reasonable in certain environments, suggested by Blandford and Payne, 1982 (disk wind). More about jet composition can be found for example in Sikora et al. (2005); Celotti (2003); Lyutikov (2005).

Relativistic beaming

The relativistic motion of the jet plasma moving towards the observer is responsible for two remarkable effects: apparent superluminal motion and Doppler boosting. Superluminal motion was predicted before it was observed in a seminal paper by Rees (1966); Doppler boost also known as relativistic beaming was first suggested by Blandford and Rees, 1978.

Especially the amplification due to Doppler boosting is important to understand the extreme nature, of these kind of sources, i.e. its extreme luminosity, e.g. Buckley, 1998.

Superluminal motion If the mean free path of particles in a jet is much smaller than the jet dimensions, particles collide frequently, resulting in a randomization of the initial velocity distribution. In such a case the velocity field is characterized by a randomly fluctuating *thermal* component, while the *bulk* of particles is characterized by an average position. Since matter streams cannot interpenetrate, but instead stop when they collide, sound or shock waves are produced, if the matter is compressible as in the case of jets. Generally these *collisional* flows in

jets are inviscid, turbulent, and supersonic, resulting in the interacting matter-streams producing shock waves. Flows in jets are not really collisional, but because of interactions between the particles and magnetic fields, they behave as though they were. As for the high energetic parts of the particle distribution the mean free path is in the order of the jet dimension, the bulk will move with the so-called *bulk* velocity $v_b = c\beta_b$.

If an emission region or emission blob (source) is moving with the so-called *pattern* speed, $v = c\beta$ at an angle θ to the line of sight, the observer will measure the source moving with an apparent speed $v_a = c\beta_a$ transverse to the line of sight. The pattern and bulk velocity must not necessarily be identical, $\beta_a = \beta'_a(\beta)$. It has also been suggested (Lind and Blandford, 1985), that the velocity responsible for the boosting of the radiation (bulk velocity) may be different (smaller) than the velocity of the pattern responsible for the superluminal motion. Identity would mean, that the emission region is moving with the same speed than the bulk of the emitting particles. With the corresponding Lorentz factor $\gamma = \sqrt{(1-\beta^2)^{-1}}$ the Doppler factor of the moving source can be defined as

$$\delta \equiv \frac{1}{\gamma(1-\beta\cos\theta)} \tag{8.2}$$

Calculating the apparent, i.e. observed transverse, velocity β_a of the emitting blob from the true velocity β in a relativistic beaming model, e.g. Pearson and Zensus (1987), obeys

$$\beta_a = \frac{\beta\sin\theta}{1-\beta\cos\theta} \tag{8.3}$$

Therefrom superluminal motion is observed, if $\beta_a > 1$. This condition turns into the condition

$$\sin\theta + \cos\theta > \frac{1}{\beta} \tag{8.4}$$

which can be fulfilled for some orientations, i.e. if $\beta > \sqrt{1/2} \simeq 0.7$. The maximum apparent velocity $\beta_a = \sqrt{\gamma^2 - 1}$ is achieved for $\cos\theta = \beta$ and $\sin\theta = \gamma^{-1}$. In this case it can be calculated that $\delta = \gamma$. This means that superluminal motion is even possible for large angles to the line of sight, e.g. $\theta \simeq 50^\circ$ and $\gamma \gtrsim 5$ yields $\beta_a \gtrsim 2$.

Superluminal motion in this context can be understood similar to a spot of a rotating Laser far away. If the Laser is rotating with rotation speed ω, its spot will move faster than speed of light c at a distance r to the source, if $r \cdot \omega > c$. In the case the jet plasma is responsible for ionization and subsequent reemission, the corresponding radiation might be detected by the observer as superluminal motion, even if the ionized material is not moving at all. This model is a way to simple but serves well for imagination. A more detailed studies on superluminal motion can be found in Pearson and Zensus, 1987.

By determination of the superluminal velocity and the Doppler factor independently the angle to the line of sight θ and the Lorentz factor γ can be inferred. This can for example be done through direct measurements in the case of the superluminal motion (β_a) and through fitting an emission model (e.g. SSC) to spectral data in case of the Doppler factor δ. Therefrom the Lorentz factor and the angle to the line of sight can be derived, if identity of bulk and pattern

motion is assumed.

$$\gamma = \frac{\beta_a^2 + \delta^2 + 1}{2\delta} \tag{8.5}$$

$$\tan\theta = \frac{2\beta_a}{\beta_a^2 + \delta^2 - 1} \tag{8.6}$$

Doppler boost If the jet is pointing towards the observer, it is amplified as a logical consequence. A jet pointing away from the observer must be attenuated. The ratio J between of the luminosity of both jets can be predicted as

$$J = \left(\frac{1 + \beta\cos\theta}{1 - \beta\cos\theta}\right)^p \tag{8.7}$$

which can be converted into

$$J = (\beta_a^2 + \delta^2)^p \tag{8.8}$$

with p a power typically in the order of $2 + \alpha$ for a moving emission region or $3 + \alpha$ for a continuous jet (Lind and Blandford, 1985; Phinney, 1986) assuming $F \propto E^{-\alpha}$ to be the intrinsic power law spectrum. Typical values for α are in the order of unity.

The intensity *boost*,which is the result of the Doppler boost discussed above, will amplify an intrinsic flux F by the third power of the Doppler factor to the observed flux F' while blue-shifting the corresponding energy E

$$F'(\delta E) = \delta^3 F(E) \tag{8.9}$$

The tree powers of delta are a result of the relativistic compression of time and the compression of length also known as the solid angle $d\Omega' = \delta^2 d\Omega$.

If the blue-shift is taken into account this converts into

$$F'(E) = \delta^{3+\alpha} F(E) \tag{8.10}$$

In both cases a continuous jet was assumed. For a moving source model an exponent of $2 + \alpha$ is appropriate (Blandford and Königl, 1979).

Depending on the morphology of the source, i.e. whether the radiation is emitted isotropically or dependent on the angle θ, the power of the Doppler factor may slightly vary.

For typical values of α in the order of unity already a small Doppler factor of ten will amplify the measured spectrum by three to four orders of magnitude. For broad-band fluxes this effect becomes even more dramatic due to an additional boost by the Doppler factor δ.

8.2. Blazars

Theory is knowledge that doesn't work.
Practice is when everything works
and you don't know why.
— Hermann Hesse.

In the following, Blazars, i.e. AGN observed from a point inside a small cone around the jet axis, will be discussed.

8.2.1. Spectral properties

Two peak nature of the non-thermal part of the spectral energy distribution The spectral energy distribution of Blazars, maybe all AGN, is characterized by two main peaks. While the first peak resides in the infrared to X-ray regime, the second peak is at typical γ-ray energies above some MeV.

Observations before the 90's showed a possible bimodality in the distribution of X-ray peak frequencies (in a νF_ν-representation). This could have been due to selection effects by the sensitivity of several experiments measuring in this energy region (Giommi and Padovani, 1994).

Newer surveys like DXRB (Perlman et al., 1998), RGB (Laurent-Muehleisen et al., 1998) and REX (Caccianiga et al., 1999) confirmed this impression and have shown a more continuous distribution.

Additionally observations of Markarian 501 (Pian et al., 1997) and 1ES 2344+514 (Giommi et al., 2000) have also extended the distribution of peak frequencies above 10 keV up to 100 keV.

Since the EGRET mission on board of the Compton Gamma Ray Observatory (CGRO) satellite (Hartman et al., 1999) many known X-ray sources have been found to emit high energy γ-rays (MeV region) (Fichtel et al., 1994; von Montigny et al., 1995; Thompson et al., 1995). Consequently ground-based gamma-ray astronomy was invented to search for the very high energy (VHE) counterparts of these objects. The first imaging air-Cherenkov telescopes (Catanese and Weekes, 1999) Whipple (Weekes et al., 1996; Petry et al., 1996) and HEGRA (Daum et al., 1997; Bradbury et al., 1997; Aharonian et al., 2004b) could extend less than a handful of EGRET-detections into this VHE region. On basis of this detections it turned out, that in some cases the bulk of the power is emitted in this very high energy band, which is of fundamental importance for the spectral energy distribution of Blazars.

It has to be kept in mind, that all currently available flux ratios between the X-ray and γ-ray peak might be biased by the limited sensitivity of the available MeV, GeV and TeV instruments, which implies the selection of the most luminous or even flaring sources.

While the source of emission might not be the same particle distribution but is still the same object, a possible correlation between the luminosity and peak frequency is expected.

Correlation of spectral properties - Blazar sequence On the basis of a large sample of well measured AGN spectra, spectral correlations have been investigated phenomenologically in Fossati et al., 1998, also known as *Blazar-sequence*. To be independent of the AGN models

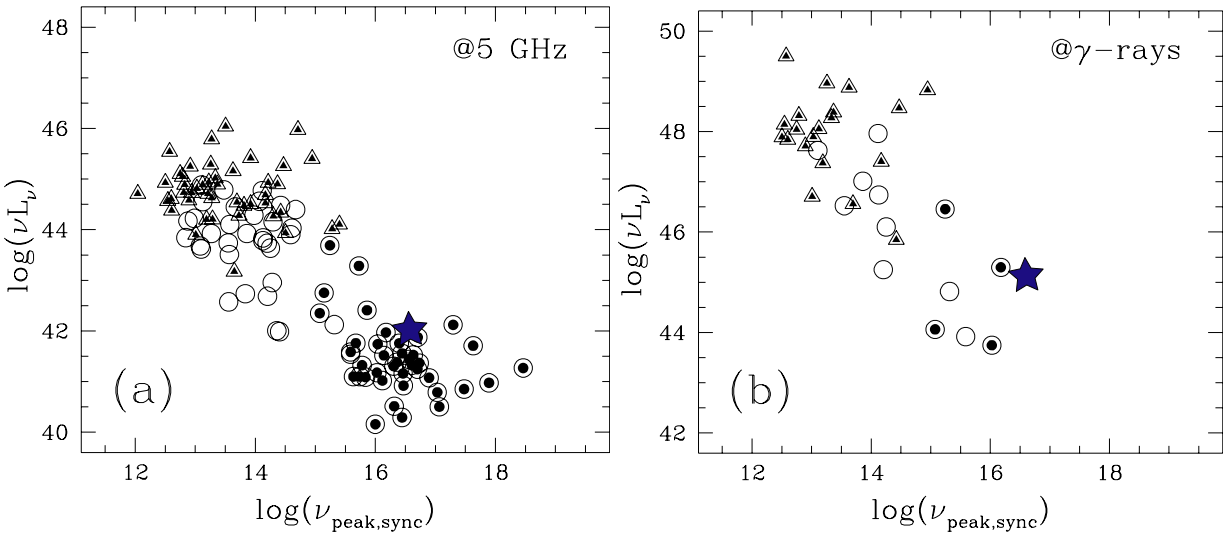

Figure 8.2.: The luminosity in the radio (5 GHz, left) and γ-ray (100 MeV) plotted versus the synchrotron peak frequency from Fossati et al. (1998) were extended with the data from the SED best-fit for 1ES 1218+304 (star).

the two peak structure has been fitted by two polynomials of the third order. Taking the strong redshift dependence of the luminosity of all the examined parameters phenomenologically into account, it turned out that a clear correlation, between the luminosity at radio frequencies (5 GHz) and γ-ray energies (100 MeV) versus the synchrotron peak frequency exists. In both cases the luminosity at the two fixed frequencies decreases with increasing peak frequencies (figure 8.2). In contradiction the peak luminosity seem to be uncorrelated with the peak frequency, especially if the sample is reduced to sources with a redshift of $z < 0.5$ to further decrease a possible dependence on redshift.

Also the two point radio-to-optical and radio-to-X-ray spectral indices α_{RO} and α_{RX}, defined as, cf. Ledden and Odell (1985),

$$\alpha_{RO} = -\frac{\log(L(\nu_R)) - \log(L(\nu_O))}{\log(\nu_R) - \log(\nu_O)} \tag{8.11}$$

and

$$\alpha_{RX} = -\frac{\log(L(\nu_R)) - \log(L(\nu_X))}{\log(\nu_R) - \log(\nu_X)} \tag{8.12}$$

show a significant decrease with increasing peak frequencies (figure 8.3, right). Investigating the γ-dominance, defined as the ratio between the γ-peak luminosity and the X-ray-peak luminosity, clearly shows, that the γ-ray peak becomes weaker compared to the X-ray peak by four orders of magnitude with increasing synchrotron peak frequencies by two orders of magnitude (figure 8.3, left). While the X-ray luminosity is decreasing with radio luminosity, the γ-ray luminosity shows an anti-correlation (increasing), figure 8.4.

According to Fossati et al. (1998) the results for the γ-ray luminosities still have to be taken carefully, due to the strong selection effect due to the sensitivity in the very high energy region.

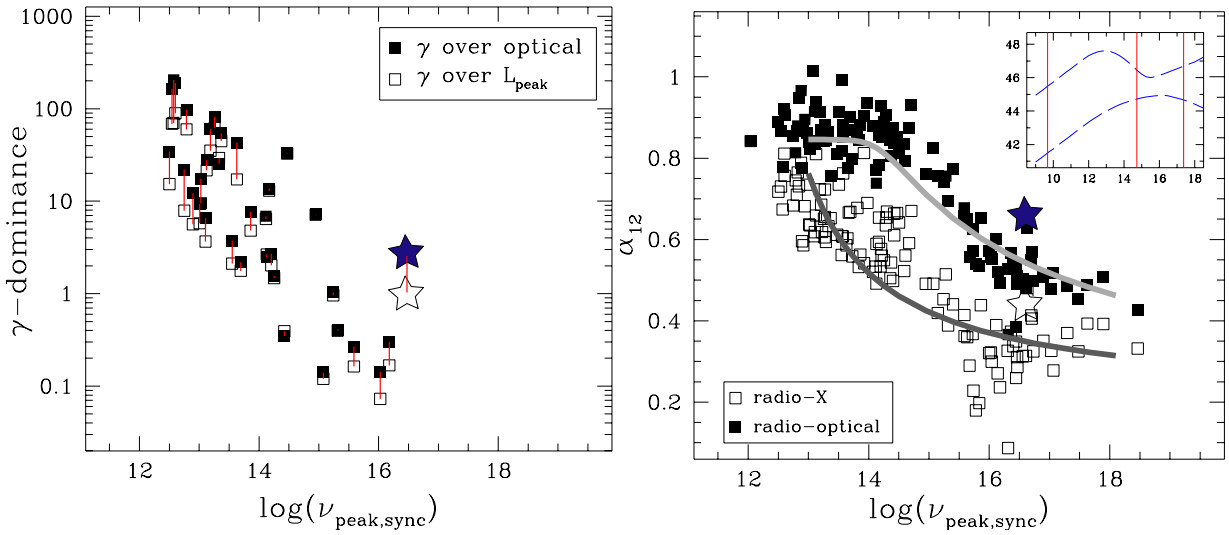

Figure 8.3.: The γ-dominance (left), expressed as ratio of the inverse Compton peak luminosity and the optical luminosity (filled) or synchrotron peak luminosities (open). Broad-band spectral indices α_{RO} and α_{RX} versus synchrotron peak luminosity (right) overlaid with the relation (lines) obtained for the average SED of the Blazar-sequence. Two typical examples of SED's are shown for reference. The three red lines mark the frequencies used to determine the spectral indices. Both plots from Fossati et al. (1998) were extended with the data from the SED best-fit for 1ES 1218+304 (star).

Similar to the model-independent approach presented, a model based study using an SSC model fit with an external component (EC) has been done by Ghisellini et al., 1998. The general results of Fossati et al. (1998) could be confirmed and quantified by this study. Based on the model the resulting correlations can be interpreted as a consequence of a change in the radiation density of the external field.

These overall similarity and regularity of the spectral energy distribution and the continuity in the properties of the large sample of Blazars used in this study suggests a basic similarity among all Blazars irrespective of their classical classification and different appearance in a specific energy band.

Summarizing these results, no correlation between the peak luminosity and its frequency could be found, while the shape of the spectrum is well determined by its luminosity, i.e. from the luminosity in X- and γ-rays, the peak positions and the proportion of both peaks can be derived.

With this assumption average SED can be calculated dividing the data sample into sub-samples differentiated by total emitted energy, cf. figure 9.1 (left). This phenomenological result has been confirmed by a model dependent approach, fitting a SSC model to the data, by (Ghisellini et al., 1998), cf. figure 9.1 (right). In both cases the resulting sequences of average SED are also known as *Blazar-sequence*.

However, the prediction for γ-ray energies by the correlations discussed above is still rather weak due to the low number of sources yet detected in this energy regime.

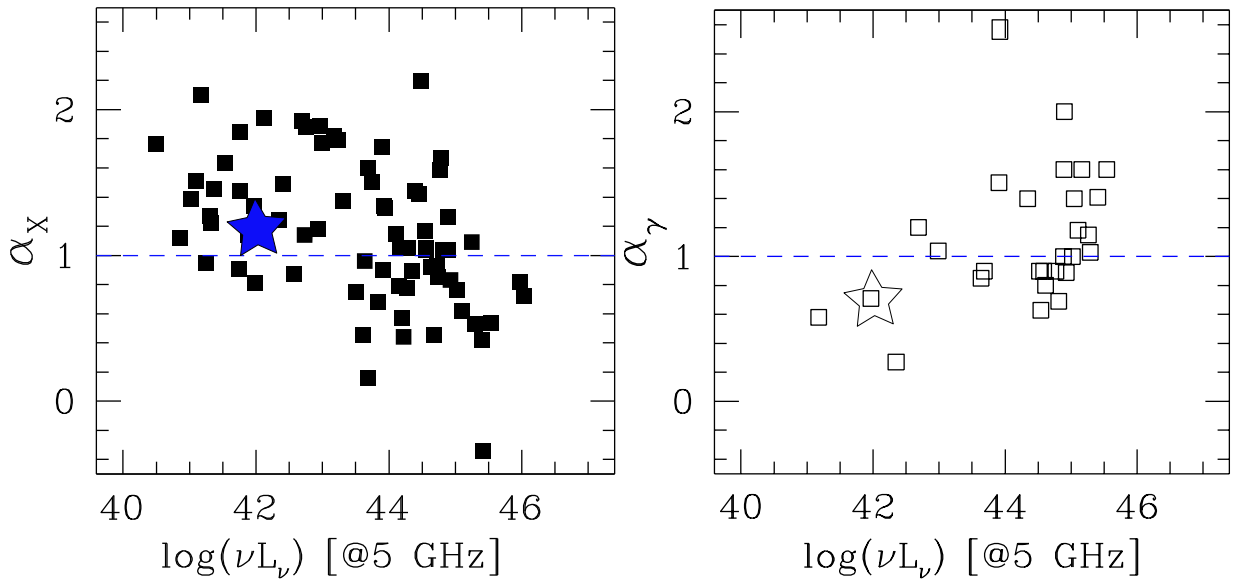

Figure 8.4.: X-ray (1 keV) and γ-ray (100 MeV) spectral index versus radio luminosity (5 GHz) from Fossati et al. (1998) extended with the data from the SED best-fit for 1ES 1218+304 (star).

To further constrain or disprove such correlations especially more data in the GeV/TeV energy domain is mandatory.

8.3. Emission models

For acceleration of particles into the very high energy region no generally accepted model exists so far, however some of the existing models are good candidates.

In Sikora (2001) leptonic models are discussed, in which the TeV gamma-rays are produced by inverse Compton radiation, originally suggested by Jones et al. (1974), of electrons at X-ray energies with synchrotron photons emitted by the same electron population (called *synchrotron self-Compton*, SSC).

Furthermore the possibility of synchrotron emission by electrons from proton induced cascades is discussed in Mannheim, 1993 (*Proton Blazar*). In Mannheim (1998) it is discussed in the context of the precise source Markarian 501.

Other models favor interaction of relativistic protons with matter (Pohl and Schlickeiser, 2000a) or the magnetic field (Aharonian, 2000).

Even more models haven been proposed, e.g. Pohl and Schlickeiser (2000b); Mücke et al. (2003).

In the following sections an outline of the SSC and Proton Blazar model will be given.

8.3.1. Synchrotron radiation

Synchrotron radiation is emitted by charged particles accelerated in magnetic fields. In Blazars relativistic electrons are accelerated in a jet moving with relativistic speed towards the observer and emit synchrotron radiation.

Simple models suggest that density deviations in the injection region are responsible for shock fronts moving with relativistic speed along the jet axis. These shocks are capable of acceleration of charged particles by first and second order Fermi acceleration and such take the charged particles outwards with the jet material. The charged particles undergo energy losses due to adiabatic expansion of the jet and synchrotron radiation emitted by interaction with the magnetic field. Adiabatic expansion means a lower density in region with higher diameter.

If magnetic field and particle distribution are assumed to be homogeneous along the jet axis models are called *homogeneous*, e.g. Inoue and Takahara (1996); Chiaberge and Ghisellini (1997); Mastichiadis and Kirk (1997), otherwise *inhomogeneous*, e.g. Marscher (1996); Maraschi et al. (1992); Marscher and Travis (1996).

With increasing energy due to the acceleration (heating) the gyro-radius of the accelerated particles widens resulting in a higher probability escaping the shock. On the other hand interaction with the magnetic field causes energy loss due to synchrotron emission (cooling).

The resulting gamma-spectrum is a consequence of the balance of the energy dependent heating and cooling with the particles escaping from the shock or the acceleration region in general.

After escaping the shock with its high magnetic field into the downstream region synchrotron radiation in the low magnetic field is negligible (Kirk et al., 1998).

Therefore the spectral shape of the synchrotron emission can be divided into three regions of different origin. At low energies the spectrum is dominated by the heating process while cooling is unimportant. With increasing energy heating and escaping becomes balanced until the spectrum is cutoff due to the energy losses. Balancing heating and escaping means that particles above a certain break energy γ_b suffer from adiabatic energy loss.

For the heating dominated part of the spectrum the spectral index of the synchrotron emission depends directly on the spectral index of the primary particle distribution, which can be calculated as follows.

Dependence of particle and emission spectral index

The motion of charged particles[1] with mass $m = \gamma m_0$ and velocity $\vec{v}$ in a magnetic field $\vec{B}$ is characterized by conservation of its momentum (Rybicki and Lightman, 1979; cf. equation 4.84):

$$\frac{d}{dt}(\gamma m_0 \vec{v}) = \frac{q}{c}\vec{v} \times \vec{B} \tag{8.13}$$

$$\frac{d}{dt}(\gamma m_0 c^2) = q\vec{v} \cdot \vec{E} = 0 \tag{8.14}$$

Equation 8.14 implies the constness of γ or $|\vec{v}|$, which further yields

$$m\gamma \frac{d\vec{v}}{dt} = \frac{q}{c}\vec{v} \times \vec{B} \tag{8.15}$$

[1] For the following discussion the charge is assumed to be unity

Splitting this equation into a component parallel and perpendicular to the magnetic field, it gives

$$\frac{d\vec{v}_{\parallel}}{dt} = 0 \tag{8.16}$$

and

$$\frac{d\vec{v}_{\perp}}{dt} = \frac{q}{\gamma m_0 c}\vec{v}_{\perp} \times \vec{B} \tag{8.17}$$

From these equations it follows, that $\vec{v}_{\parallel}$, $|\vec{v}|$ and $|v_{\perp}|$ must be constant, which is identical to a circular motion in the projection on the plane normal to the field axis. Together with the uniform motion along the field axis a helical motion is performed.

The frequency of gyration $\omega = qB/\gamma m_0 c$ can be derived from identification of the Lorentz force $qv_{\perp}B$ with the centrifugal force $m_0 v_{\perp}^2/r$ and $v_{\perp} = \omega r$, yielding the total emitted power (Rybicki and Lightman, 1979; cf. equation 4.92)

$$P = \frac{2q^2}{3c^3}\gamma^4 \frac{q^2 B^2}{\gamma^2 m_0^2 c^2} v_{\perp}^2 \tag{8.18}$$

$$P(\omega) = \frac{2q^2}{3c^3}\gamma^4 \omega^2 v_{\perp}^2 \tag{8.19}$$

Using the same identification and $m_0 c^2 = q^2/r_0$ this can be rewritten as

$$P(\beta_{\perp}) = \frac{2}{3}(r_0 \beta_{\perp} \gamma B)^2 c \tag{8.20}$$

Taking the velocity distribution (Three dimensions with two perpendicular dimensions yield $v_{\perp}^2 = 2/3v^2$) into account the following formula can be obtained

$$P = (\frac{2}{3} r_0 \beta \gamma B)^2 c = \frac{4}{3}\sigma_T c \beta^2 \gamma^2 U_B \tag{8.21}$$

with $\sigma_T = 8/3\pi r_0^2$ the Thomson cross section and $U_B = B^2/8\pi$ the magnetic energy density.

Defining a critical frequency

$$\omega_c = \frac{3}{2}\gamma^3 \omega \sin\alpha \tag{8.22}$$

later seen to be representing a spectral cutoff, equation 8.21 turns into

$$P(\omega) = \frac{\sqrt{3}}{2\pi}\frac{q^3 B \sin\alpha}{mc^2} F\left(\frac{\omega}{\omega_c}\right) \tag{8.23}$$

If the number density of particles with energies between E and $E + dE$ can be approximately expressed in the form

$$N(E)dE = CE^{-p}dE \qquad \text{for} \qquad E_1 < E < E_2 \tag{8.24}$$

the total power radiated per unit volume per unit frequency is given by the integral $N(\gamma)d\gamma$ times the single particle radiation formula over all energies γ

$$P_{tot}(\omega) = C \int \gamma_1\gamma_2 P(\omega)\gamma^{-p} d\gamma \tag{8.25}$$

Changing variable of integration yields

$$P_{tot}(\omega) \propto \omega^{-(p-1)/2} \tag{8.26}$$

Thus the spectral index s of total power emitted at frequency ω $P(\omega) \propto \omega^{-s}$ is related to the slope p of the primary particle distribution $N(E) \propto E^{-p}$

$$s = \frac{p-1}{2} \tag{8.27}$$

See also Landau and Lifshitz, 1971.

8.3.2. Fermi acceleration

In the past the calculation of the particle distribution $N(E) \propto E^{-p}$ resulting from Fermi acceleration in relativistic shocks has been evolved.

While non relativistic strong shocks produce a particle spectrum with a slope of $p = 2$ for the number of particles per unit energy, Kirk and Schneider (1987) found that for relativistic shocks a slightly higher slope of $p \approx 2.0 - 2.4$ is expected.

In Blasi and Vietri (2005) more dependencies, especially the one on the pitch-angle, were taken into account yielding a particle spectrum with $p \approx 1.5 - 3.0$, which is reduced to the previous result in the limit of small pitch-angle scattering.

Consequently a primary particle spectrum of $p \approx 1.5 - 3.0$ will result in a spectral index s of the synchrotron radiation spectrum $F(E) \propto E^{-s}$ of

$$s \approx 0.25 - 1.0 \tag{8.28}$$

due to the relation from equation 8.27).

The above estimation is valid for the spectral energy region in which cooling and heating are balanced. As discussed in the next subsection inverse Compton radiation would produce an identical or steeper slope at higher energies (MeV-TeV). Thus measurements in the cutoff region above the region of balance should show a steeper spectrum.

8.3.3. Inverse Compton

By the inverse Compton process photons can be upscattered into the TeV energy range by the accelerated charged particles. The target photons can be either synchrotron photons (Maraschi et al., 1992; Bloom et al., 1993; Ghisellini and Maraschi, 1994) or produced by processes in the accretion disk (Dermer and Schlickeiser, 1993) or in the broad line region itself. The broad

line region can be illuminated by the accretion disk (Sikora et al., 1994; Blandford, R. D., 1993; Blandford and Levinson, 1995) or self-illuminated by the jet (Ghisellini and Madau, 1996). Also target photons from the dusty torus seem possible (Wagner et al., 1995).

The current two leading pictures are synchrotron photons (synchrotron self-Compton, SSC) as target photons and target photons produced outside the γ-ray emission region (External Compton, EC). For simplicity in the following the target photons are named synchrotron photons γ_{sync}.

$$e^{\pm} + \gamma_{sync} \longrightarrow \tilde{e}^{\pm} + \gamma_{HE} \tag{8.29}$$

Inverse Compton scattering by electrons of Lorentz factor γ shifts the energy of synchrotron photons γ_{sync} with energies E_{sync} to a distribution with mean energy $\bar{E}$:

$$\bar{E} = \frac{4}{3} E_{sync} \gamma^2 \tag{8.30}$$

The width of the resulting energy distribution for mono energetic photons is small compared to the synchrotron photon source distribution. The particle distribution can be assumed to be mono energetic, because almost all energy is deposited at the break energy. This leads to a simple copy of the shape of the spectral energy distribution from X-ray energies to TeV energies while the energy deposited per unit energy is of the same order, due to the cross section being the Thomson cross section and constant.

The initial electron spectrum, in the case of Fermi acceleration, has no obvious high-energy cutoff. This yields energies high enough, that the cross section enters the Klein-Nishina regime steepening the falling edge of the inverse-Compton peak (Tavecchio et al., 1998), i.e. the emission region becomes optically thick.

Inverse Compton radiation of accelerated heavier particles (protons) is highly attenuated compared with electrons, because the $\sim$1800-time higher mass of protons enters the probability for the process to the third power, e.g. Mannheim (1997); Pohl and Schlickeiser (2000b).

Thus Fermi acceleration of electrons will be much less efficient than acceleration of protons leading to the fact that electrons should be less dominant in cosmic-ray energy, which is consistent with observations (Sikora et al., 1987).

Subsequently a proton population will produce a secondary high energy electron population which is capable of the process described above. This process will be discussed in the next section.

8.3.4. Proton Blazar

Fermi acceleration is sensitive to charge only, hence it follows, that in addition to the accelerated electrons and positrons accelerated protons must be expected.

The acceleration process terminates, when the cooling or particle escape rate exceeds the acceleration rate. While the gyro radius of protons is larger by the order of the mass ratio between protons and electrons the cooling time is correspondingly smaller. This allows protons to be accelerated to higher energies (10^{11} GeV) than electrons in the shock front, if the jet morphology (diameter) is large enough compared to the proton gyro radius at their acceleration break energy.

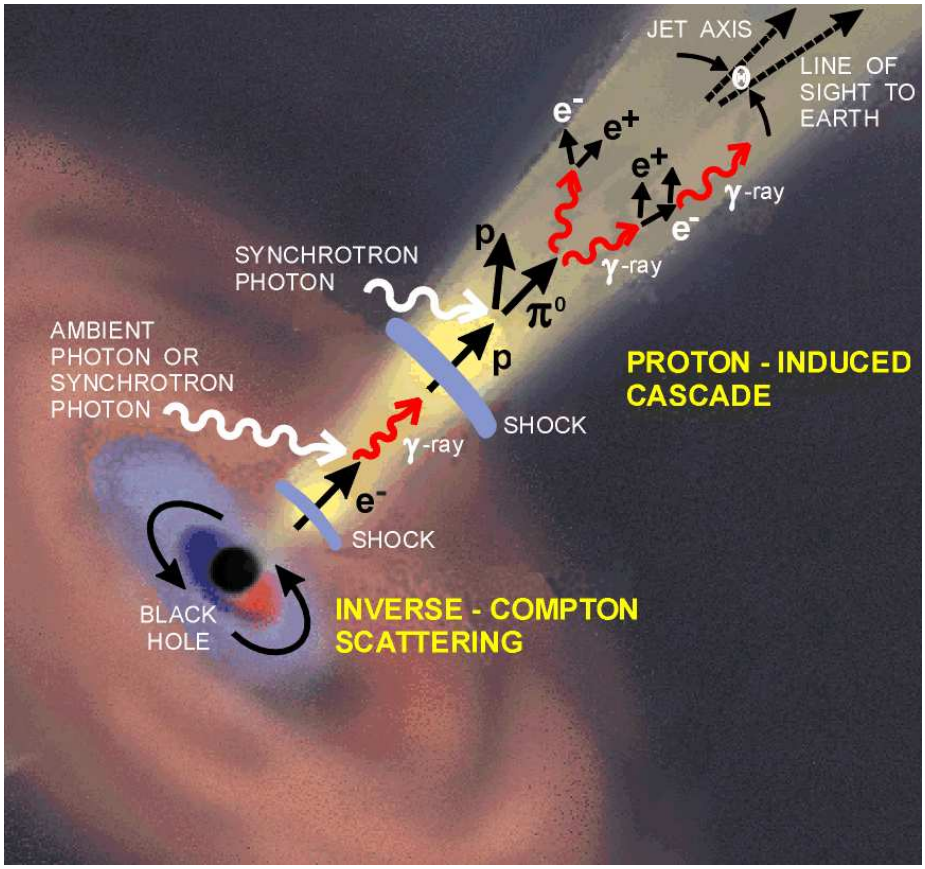

Figure 8.5.: Gamma-ray production in relativistic jets. (Reprinted from Buckley J 1998 *Science* **279** 676. ©1998 American Association for the Advancement of Science.)

Electron acceleration should be less efficient than proton acceleration, because of the smaller gyro radius of electrons and the finite shock thickness, which is consistent with the observation, that electrons contain only $\sim$2% of the energy of cosmic rays, e.g. Schlickeiser, 2003. By meson-, mainly pion-photo-production (Sikora et al., 1987) and subsequent decay into neutrinos, gamma-rays and electron-positron pairs, a secondary electron population is created with energies well above the energies of the primary electron population.

Due to the high cross-section for pair-production and inverse Compton radiation of extremely high energy electrons with the synchrotron photon, the plasma is optically thick (opaque), e.g. Burns and Lovelace (1982); Svensson (1987); Berezinskii et al. (1990). This leads to an instantaneous redistribution of energy through electromagnetic cascades below the critical energy E^*_γ, which is the energy at which the jet becomes optically thin (transparent).

There are two possibilities of photo-production by the protons with similar probability, the weak and electromagnetic decay.

In the first case π^0-mesons are produced by an interaction of the accelerated (high energy)

proton with the synchrotron photons:

$$p^+ + \gamma_{sync} \longrightarrow p^+ + \pi^0 \tag{8.31}$$

The π^0 itself decays into two (high energy) γ-rays:

$$\pi^0 \longrightarrow \gamma + \gamma \tag{8.32}$$

In this process a fair fraction of the initial proton-energy is transferred to the γ-rays, which can consequently further produce pairs by interacting with the lower energy synchrotron photons:

$$\gamma + \gamma_{sync} \longrightarrow e^+ + e^- \tag{8.33}$$

The $e^\pm$ will now loose their energy either by synchrotron radiation or due to inverse Compton scattering with the synchrotron photons

$$e^\pm_{HE} + \gamma_{sync} \longrightarrow e^\pm_{LE} + \gamma \tag{8.34}$$

These processes will happen iteratively until the energy of the γ-rays are small enough that the γ-rays can leave the medium. The transition from an optically thick to an optically thin medium happens at TeV-energies, therefrom the emitted photons are expected to be in the TeV-energy range.

In the second case photo-production happens through the conversion of the proton into a neutron and π^+-meson. The neutron will decay into an electron, the corresponding electron-antineutrino and a proton. The π^+ will decay into a muon and the corresponding muon-neutrino. The muon itself will decay into an muon-antineutrino, an electron-neutrino and a positron.

$$p^+ + \gamma_{sync} \longrightarrow n + \pi^+ \quad \left\{ \begin{array}{lcl} n & \longrightarrow & e^- + \bar{\nu}_e + p^+ \\ \pi^+ & \longrightarrow & \nu_\mu + \mu^+ \quad \Rightarrow \quad \mu^+ \longrightarrow \bar{\nu}_\mu + \nu_e + e^+ \end{array} \right. \tag{8.35}$$

The neutrinos will directly leave the jet due to their very long mean free paths and their detection would thus be a direct indication for the existence of ultra high energy protons in the jets and their subsequent cascades. Depending on the maximum energy reached by the acceleration mechanism the neutrino energies might be in the detection range of experiments like AMANDA, DUMAND II, BAIKAL (Stenger et al., 1992; Halzen and Zas, 1992) at TeV/PeV energies or their successors ICE-CUBE, Antares (Hernández-Rey, 2005) above PeV energies.

Vice versa also an evidence for very high-energy γ-ray emission from proton initiated cascades would imply the existence of neutrino emission.

The transition between optically thick and thin plasma leads to a cutoff in the spectrum and a steepening of the spectral slope of $F \propto E^{-3}$ at TeV energies compared to $F \propto E^{-2}$ in the MeV/GeV energy domain (Mannheim, 1997).

A detailed description of proton initiated cascades in Blazar jets can be found in Mannheim et al. (1991) and Mannheim (1993).

9. Spectral Energy Distribution

Vorstellungskraft ist wichtiger als Wissen.
— Albert Einstein, 1879-1955.

By measuring the spectral energy distribution (SED), from radio to TeV energies, models, as the ones discussed in the last chapter, can be tested.

Since the emission of AGN spreads over more than ten decades of frequencies no current instrument is able to detect emission in more than a small fraction of the full energy range. Therefrom current SED are combined from the data taken with a lot of different instruments, which in most cases are not simultaneously.

Especially at TeV energies most of the sources are not visible at all due to the limited sensitivity of current Cherenkov telescopes. Therefore predictions with common models have been made about the SED of several objects and thus their visibility at TeV energies, e.g. Mannheim et al. (1996); Costamante et al. (2001).

For the MAGIC-telescope ∼50 high-peaked BL-Lacertae (HBL; Padovani and Giommi, 1995) object have been proposed and their observation has started in autumn 2004. In January 2005 the first HBL, 1ES 1218+304, has been discovered at 100 GeV. The result of the observation has been presented in this thesis.

In the following the measured spectrum should be discussed in the context of available measurements in other wavelengths and common models describing this object class.

The data The source 1ES 1218+304 has already been detected by many previous experiments at a lot of different wavelengths, namely in the radio, optical, UV and X-ray. Since all of this observations have been independent, and in many cases is was not obvious that the same source was detected, 1ES 1218+304 is also known by a lot of other catalog-names, shown in table 9.1.

QSO B1218+304	2A 1218+304	2A 1219+305
3A 1218+303	D113	B2 1218+30.4
BWE 1218+3027	CSO 133	B1218+304
QSO B1218+304	EXO 1218.8+3027	FBQS J1221+3010
FIRST J122121.9+3010	87GB 121852.6+302715	H 1219+305
H 1218+304	1H 1219+301	PG 1218+304
RBS 1100	1REX J122121+3010.6	RGB J1221+301
RX J1221.3+3010	1RXS J122121.7+30104	J122121.9+301037

Table 9.1.: Known synonyms (www-16) for 1ES 1218+304, see also (www-17).

The spectral information available publicly has been collected and updated with the data achieved with the presented analysis.

Additional to a collection of multi-wavelength data available at (www-14) as 1H 1219+301, X-ray data from ROSAT (Lamer et al., 1996) and XMM-Newton (Blustin et al., 2004) was added. The preliminary data of the Swift satellite (Giommi et al., 2006) available at the ASDC web-page could also be added.

Further upper limits in the MeV and TeV energy region have been published in the past years. The upper limit of the EGRET experiment is $F(>100\,\mathrm{MeV}) \approx 10^{-11}\,\mathrm{erg\,cm^{-2}\,s^{-1}}$. Several observations with the Whipple telescope between 1995 and 2000 resulted in an upper flux limit of $F(>350\,\mathrm{GeV}) = 8.3 \cdot 10^{-8}\,\mathrm{m^{-2}\,s^{-1}}$ (corresponding to $\sim$8% of the Crab Nebula flux) (Horan et al., 2004). The source was also observed by HEGRA between 1996 and 2002. An upper flux limit above 840 GeV of $2.67 \cdot 10^{-8}\,\mathrm{m^{-2}\,s^{-1}}$ (or 12% of the Crab Nebula flux) is reported by Aharonian et al., 2004b.

With the new measurements of the MAGIC-telescope the upper limits already available in the TeV energy region could be turned into a spectral point and extend the SED of 1ES 1218+304 to the highest energies.

As of its huge systematic uncertainty due to the measurement (see chapter 6) the first point was omitted. Since the last two points suffer from high uncertainties in the correction for pair-production along the line of sight (see section 7) the last two points are also omitted. All upper limits above 100 GeV have been corrected for the effect of pair-production along the line of sight by an upper limit for the MRF as discussed in Kneiske et al. (2004), so that they can still be considered real upper limits. For the remaining MAGIC data points a correction with a lower and upper limit for the MRF is shown, resulting in corrected spectral points still inside the statistical and systematic errors of the original data points.

None of the measurements was taken simultaneously, except the KVA optical data (www-15), which showed no significant variability. The closest other observation are the preliminary data of the Swift satellite taken in October 2005.

The model The collected data was fitted by a synchrotron self-Compton model publicly accessible at (www-14). According to Giommi (2006) the model was programmed based on Tavecchio et al. (1998), which is an extension of Ghisellini et al. (1996).

The model is a homogeneous SSC model, with the assumption that the radiation is produced by a single zone in the jet. The emission zone is supposed to be a sphere with radius r moving at small angle to the observer's line of sight. The photons of the lower energy peak are produced by synchrotron radiation of electrons Fermi-accelerated in a magnetic field B to relativistic energies. The second peak at gamma-ray energies originates from subsequent inverse-Compton scattering of these photons on the same electrons. The key parameter is the Doppler factor Γ (cf. equation 8.10). For the highest energy electrons the Klein-Nishina limit is taken into account yielding a steepening of the falling edge of the inverse-Compton peak. Since radio frequencies are self-absorbed by this model the radio-emission will not be reproduced correctly. For a correct representation of the radio data further constraints from the outer region of the jet are necessary. For this reason the radio data is omitted in the following study.

The relativistic electron spectrum is assumed to steepen with increasing energy. This behavior is approximated with a broken power-law, breaking at the Energy $E_{br} = \gamma_{br} m_e c^2$:

$$N(\gamma) = \begin{cases} K\gamma^{-n_1} & \text{for} \quad \gamma < \gamma_{br} \\ K\gamma^{n_2-n_1}\gamma^{-n_2} & \text{for} \quad \gamma > \gamma_{br} \end{cases} \tag{9.1}$$

Therefrom the model is fully constrained by the radius r of the emission region, the magnetic field strength B, the Doppler factor Γ, the Lorentz factor (energy) of the electrons at the break γ_{br}, the spectral indices n_1 and n_2 before and after the break and the normalization K of the electron density.

Constraints This seven model parameters can directly be correlated with observable quantities, which can directly be derived from available SED data, if measured simultaneously. These quantities are the spectral slopes α_1 and α_2 before and after the synchrotron peak, the two peak-frequencies ν_s and ν_c, and the corresponding luminosities $L_s(\nu_s)$ and $L_c(\nu_c)$. The quality of this correlation suffers from asynchronous measurement due to the typical high variability of AGN. The better the wavelength coverage of synchronous data is the better the model can be constrained.

Since the model counts seven parameters and the observations six quantities another quantity is necessary to close the system. This can be the minimum time scale for variability t_{var} or the source dimension $R \leq c t_{var} \delta$. Further quantities give additional and independent constraints, see Tavecchio et al., 1998.

Constraints on the magnetic field strength B and the Doppler factor δ can already be calculated from the knowledge of the synchrotron and inverse Compton peak-frequencies, also shown in Tavecchio et al., 1998. These constraints in the $B\delta$-plane are shown in figure 9.2 at the end of the chapter. The peak frequencies, $\nu_s = 4 \cdot 10^{16}$ Hz and $\nu_c = 2 \cdot 10^{25}$ Hz, are derived from the model fit shown in the next section. For the spectral indices the same values as given by Tavecchio et al. (1998) for Markarian 421, $\alpha_1 = 0.5$ and $\alpha_2 = 1.75$, are used due to the similar shape of the SED of both objects, also shown later. The dashed lines show a lower and upper limit, calculated from equation

$$\delta < \delta_{KN} = \sqrt{\frac{\nu_c \nu_s}{\frac{3}{4}\left(\frac{mc^2}{h}\right)^2}} \tag{9.2}$$

and

$$\delta < \delta_{KN} = \sqrt{\frac{\nu_c \nu_s}{\frac{3}{4}\left(\frac{mc^2}{h}\right)^2} \frac{1}{e^g}} \qquad \text{with} \qquad g = \frac{1}{\alpha_1 - 1} + \frac{1}{2(\alpha_2 - \alpha_1)} \tag{9.3}$$

describing the transition from the Thomson to the Klein-Nishina regime, calculated in the Thomson and Klein-Nishina limit respectively. This can be understood as a lower and upper limit for the transition. In the intermediate region no clear distinction can be drawn. The solid black line gives a lower limit $\delta \gtrsim 14$ on the Doppler factor calculated from the condition of transparency of γ-rays due to pair-production absorption

$$\delta > \left(\frac{\sigma_T}{5hc^2} \, d_L^2 (1+z)^{2\beta} \, \frac{F(\nu_0)}{t_{var}} \right)^{\frac{1}{4+2\beta}} \tag{9.4}$$

for $\nu_\gamma = \nu_c$, $d_L = 1.2\,\mathrm{Gpc}$ and a time scale of variability $t_{var} = 1\,\mathrm{h}$. As time scale a typical variability time scale of AGN as Markarian 421 has been chosen. Due to the similarity of both objects, neglecting the fact that the intrinsic power of 1ES 1218+304 seems to be greater by one order of magnitude, this should be a reasonable assumption. If the time scale would change by a factor ten the limit would correspondingly change by $\sim$30%. This condition does not depend on the specific emission mechanism and is therefore a strong independent constraint on the minimum Doppler factor in the SSC model. It has been derived by Tavecchio et al. (1998) from Dondi and Ghisellini (1995).

Even if the variability time scale is different by two orders of magnitude it is likely that the emission takes place in the Klein-Nishina limit. The red solid line gives a constraint on the magnetic field and the Doppler factor for the case of the Klein-Nishina regime, calculated from

$$\frac{B}{\delta} = \frac{\nu_s}{\nu_c^2}\left(\frac{mc^2}{h}\right)\frac{e^{g\cdot g}}{3.7\cdot 10^6}\,\frac{1}{1+z} \qquad \text{with} \qquad g = \frac{1}{\alpha_1 - 1} + \frac{1}{2(\alpha_2 - \alpha_1)} \tag{9.5}$$

For completeness also the Thomson case is shown (blue)

$$B\delta = (1+z)\,\frac{v_s^2}{2.8\cdot 10^6\,\nu_c} \tag{9.6}$$

This constraint is derived from the dependence of the peak frequencies and the break energy. To take care of the uncertainty in the peak frequencies the gray lines show how the limits would shift with changing peak frequencies. The case of a higher inverse Compton peak is not shown because this would contradict the MAGIC measurement.

Since the time variability is of more importance in all other conditions than in the transparency condition no further constraints can be drawn without direct measurements of the time variability of 1ES 1218+304.

Taking the uncertainties into account it can be concluded that the Doppler factor is above 14 and the magnetic field between 0.1 G and 2 G.

SSC model fit The result of the model fit discussed above is shown in figure 9.3 at the end of the chapter. The black line, called *best-fit*, is prepared to match the simultaneous KVA optical data point, the MAGIC data and the previously calculated constraints. The lower and upper limit shown take the wide spread of the optical and X-ray data into account. To include the MAGIC error bars into the discussion the lower and upper limit can be scaled respectively by changing the magnetic field, the Doppler factor or the jet radius. The result for the three fits is given in the following table:

Parameter	Min	Best-Fit	Max
Norm/cm^{-3}	2.4	2.4	2.4
Index 1	1.54	1.59	1.65
Index 2	5.00	5.12	5.20
Break Energy $\log_{10}(\gamma_{brk})$	4.58	4.59	4.48
Magnetic Field/G	0.5	0.63	0.98
Doppler Factor Γ	16.2	19.5	24.8
Jet Radius/pc	0.0011	0.0011	0.0011

The legend in the plot gives the experiments and, if available, times of observations. The optical data taken from NASA's extragalactic database (NED) is not subdivided into single observations.

Conclusion Figure 9.1 shows the average SED calculated phenomenologically by Fossati et al. (1998) and with a model-fit approach by Ghisellini et al. (1998) as discussed in section 8.2.1. Comparing the best-fit SED of 1ES 1218+304 (blue) with these average SED, indicates, that the observed source belongs to the average SED with the lowest radio-flux shown, which was suggested to be the common SED of HBL.

Taking the strong correlation between the fit coefficients into account the resulting coefficients of SSC model fit match well the coefficients given by Ghisellini et al. (1998) for the matching average SED.

To compare the result further with the correlations discussed in section 8.2.1 the peak luminosities have to be corrected for the beaming effect. Taking a mean Doppler factor, e.g. Ghisellini et al. (1993), of $\delta = 7$ and $\alpha = 0.75$, e.g. Ghisellini et al. (1993), equation 8.10 yields an peak luminosity between $1.5 \cdot 10^{41}$ erg/s and $2.2 \cdot 10^{42}$ erg/s, depending on the precise jet model used. The resulting luminosity range fits into the correlations as shown in figures 8.2 to 8.4.

This can be interpreted as an evidence for the existence of a common class of objects as predicted by the *Blazar-sequence* well described by their radio-luminosity. However, there are indications for objects contradicting the predictions of this sequence, e.g. Giommi et al. (1999); Padovani et al. (2003); Caccianiga and Marchã (2004); Giommi et al. (2005); Nieppola et al. (2006), as a slightly higher luminosity for an object like the discussed one would also do.

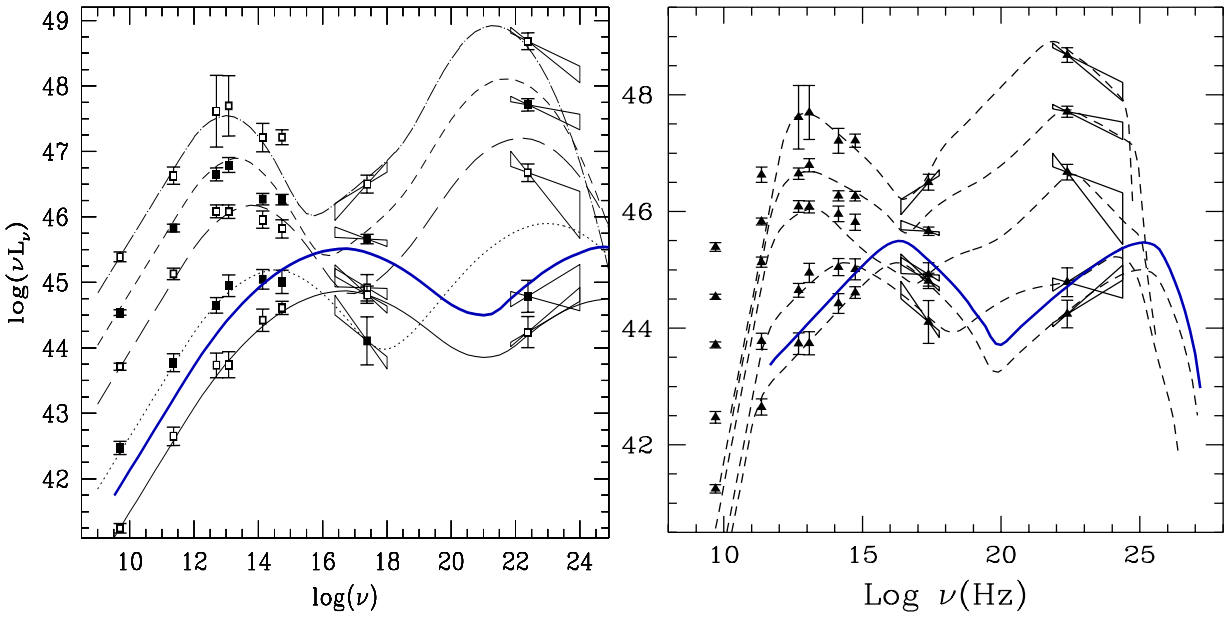

Figure 9.1.: Average spectral energy distributions calculated for a phenomenological approach (Fossati et al., 1998) (left) and a model-fit approach (Ghisellini et al., 1998) (right) superimposed by the SED of 1ES 1218+304 (blue line) as shown in figure 9.3.

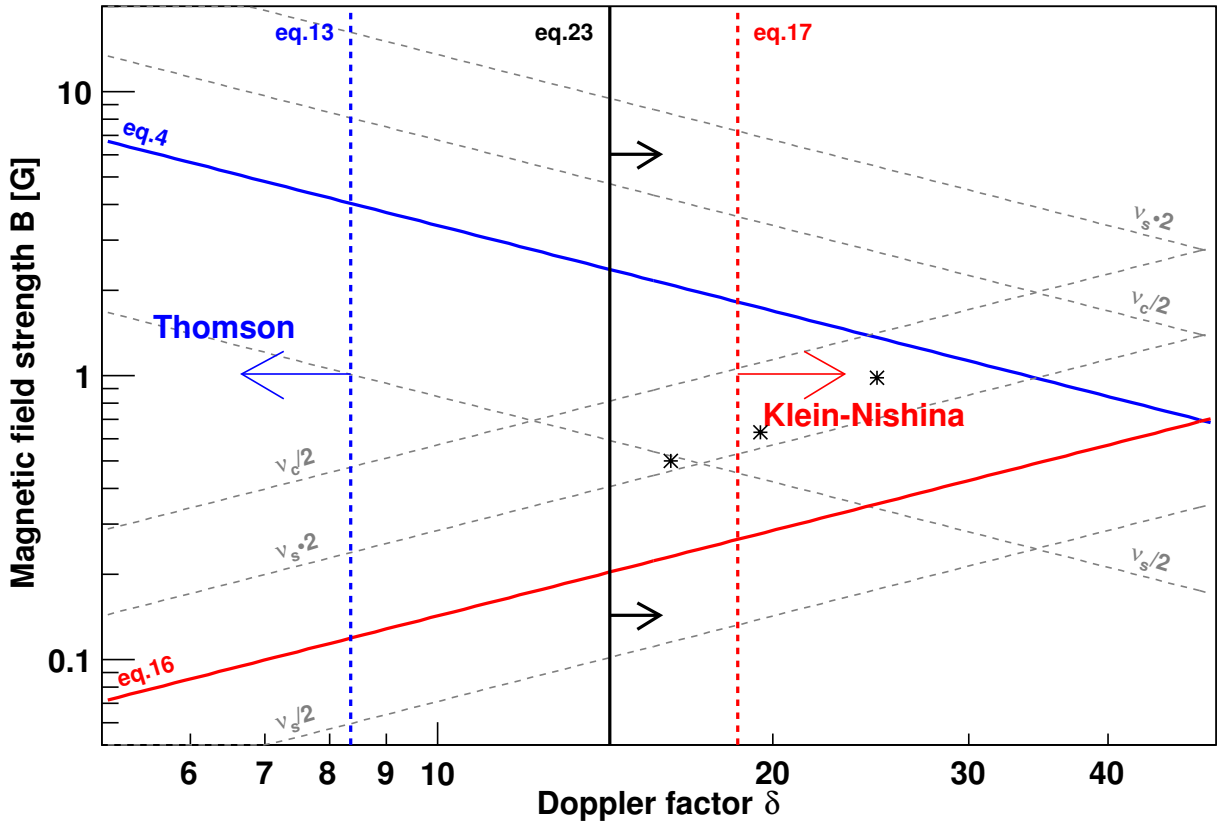

Figure 9.2.: Constraints in the Bδ-plane. The blue dashed line corresponds to a lower limit for the transition between the Thomson and Klein-Nishina regime, the red dashed line to an upper limit. The black solid line gives a strong lower limit on the Doppler factor calculated from the transparency condition. The blue solid line corresponds to a correlation calculated for the Thomson case from the two peak frequencies; the red solid line is the Klein-Nishina case. The dashed gray lines show how these correlations would move due to a factor two uncertainty in the peak frequencies. The three stars are the values for the SSC fits discussed in the text. The number of the equations given refer to the enumeration from Tavecchio et al., 1998. More details are given in the text.

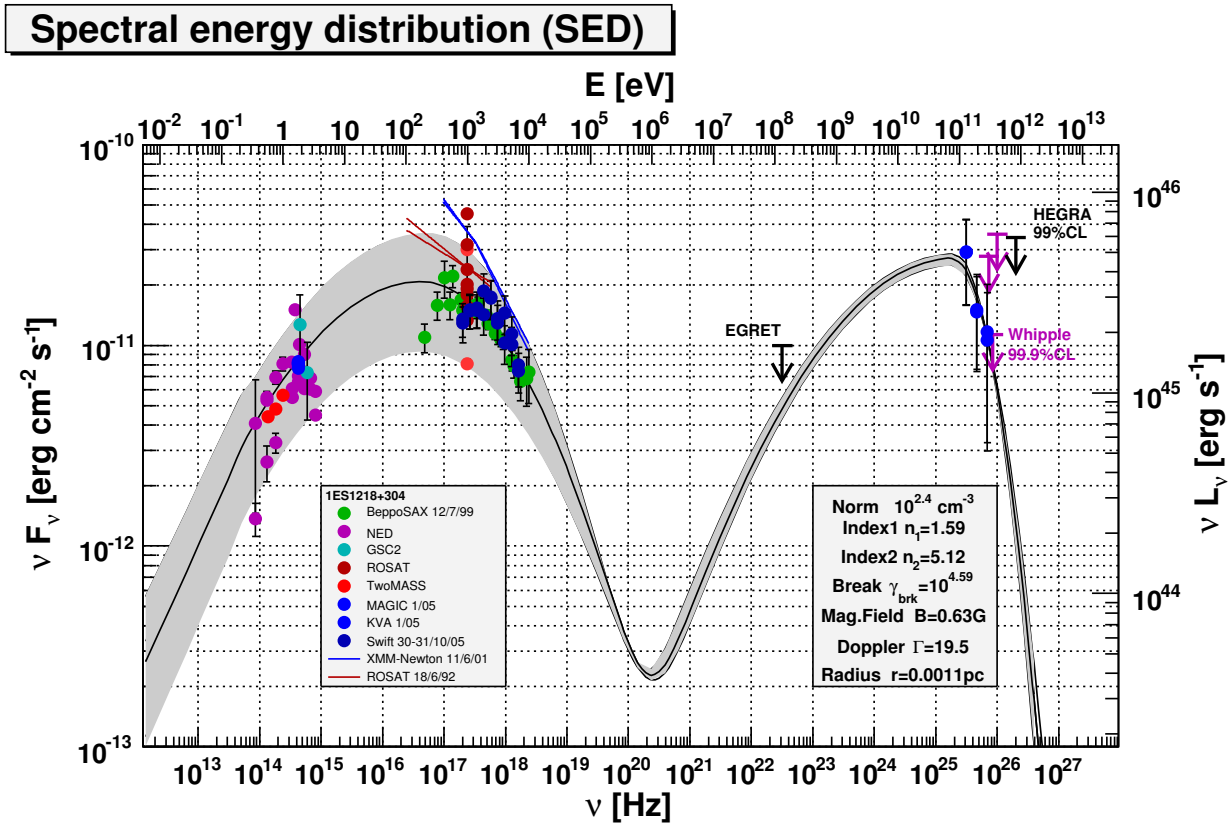

Figure 9.3.: Spectral energy distribution, i.e. total emitted power per unit energy, of the Active Galactic Nucleus 1ES 1218+304. The upper limits of previous TeV measurements and the new data from the MAGIC-telescope are shown corrected for the influence of the metagalactic radiation field. For the MAGIC-data an upper and lower limit of this correction is shown. For the upper limits from other experiments only the higher values are given. The best fit of a SSC model is shown matching the synchronous optical data of MAGIC and the KVA; the corresponding numbers are given. A possible range allowed by the asynchronous multi-frequency data is shown as gray-shaded region.

10. Summary and Conclusion

Not only is the universe stranger than we imagine,
it is stranger than we can imagine.
— Sir Arthur Eddington.

Since measurements of the EGRET experiment on board of the CGRO-satellite uncovered *Blazars* as sources of high energy gamma-rays, the search for emission of very high energy (VHE) from these sources has been a major goal for ground-based gamma-ray astronomy. The first discovery of a Blazar emitting at VHE energies ($\gtrsim$350 GeV) was the detection of Markarian 421 by the Whipple-observatory (Punch et al., 1992). A total of 271 discrete sources were detected in the energy range in which the EGRET experiment was sensitive to (100 MeV-10 GeV). However, only a handful of VHE sources were found by ground-based telescopes, although their sensitivity is superior in their energy range to that of EGRET. The total number of detections of VHE Blazars published in the literature so far amounts to 11, while the number of high-confidence Blazars in the 3^{rd} EGRET catalog is 66 (Hartman et al., 1999).

A likely explanation for this difference is the attenuation of gamma-rays due to photon-photon interactions with low energy photons from the extragalactic background radiation as pointed out by Stecker et al. (1992). This is in agreement with the fact that all Blazars detected so far above 350 GeV are rather nearby sources. Gamma-ray attenuation is expected to increase with the redshift of the source and with photon energy. The resulting relation between the e-folding attenuation energy and the redshift has been coined the *Fazio-Stecker relation* Fazio and Stecker (1979); Kneiske et al. (2004) and can be observationally probed by Blazar observations.

The VHE gamma-ray emitting Blazars known so far all belong to the class of high-frequency-peaked BL-Lacertae objects (HBL; Padovani and Giommi, 1995), a subclass of Blazars characterized by a low luminosity when compared with quasars and a synchrotron peak in the X-ray band. Their *spectral energy distribution* (SED) is characterized by a second peak at very high gamma-ray energies. Theoretical models invoke either a synchrotron self-Compton (Costamante and Ghisellini, 2002) or hadronic (Mannheim et al., 1996) origin of the very high energy gamma-rays. In synchrotron self-Compton (SSC) models it is assumed that the observed gamma-ray peak is due to the inverse-Compton emission from the accelerated electrons up-scattering previously produced synchrotron photons to high energies (Maraschi et al., 1992). In hadronic models, secondary electrons and positrons, arising from photo-meson production, initiate electromagnetic cascades (Mannheim, 1993; Mücke and Protheroe, 2001).

By increasing the sensitivity and decreasing the energy threshold, the MAGIC-telescope has been designed to provide answers to the problem of the missing Blazars at VHE energies.

The telescope has been designed to detect faint air showers (Moralejo et al., 2003; Albert et al., 2005). It was built and is located at the Roque de los Muchachos at the Canary island San Miguel

de La Palma at 28.8° N, 17.8° W, 2200 m above sea level. The main reflector of the MAGIC-telescope is an isochronous, tessellated 17 m dish controlled by an automatic adjustment system maintaining the parabolic shape during pointing and tracking maneuvers. The tracking system has to allow fast repositioning in case of Gamma Ray Burst alerts, and a tracking accuracy of less than 0.01° is required. Detection of faint air showers needs the use of a fine pixelized camera with high efficiency photomultipliers and accompanies a high trigger rate in the order of 200 Hz-300 Hz. Therefore a large data stream must be recorded and analyzed.

By designing a tracking system based on microcontrollers and three 11 kW motors driving the telescope a stable positioning and tracking could be achieved. The coupling of two motors rotating the telescope (azimuth) by their nominal torque allows to move the more than 60 t weight of the structure fast enough to detect GRB already in their prompt phase. With high precision 14 bit absolute shaftencoders a positioning accuracy of $\sim$1.3 minutes of arc was realized. Combining the shaftencoder information with the information of relative encoders at the motor axes a tracking accuracy of less than 1.3 minutes of arc were realized. A new starguider algorithm comparing a CCD image of the stars of the night sky with their nominal catalog position allows absolute calibration of the pointing algorithm and can even be used for further improving the tracking accuracy.

To manage the high data rates produced by the new generation of Cherenkov telescopes a new generation of analysis software had to be developed. The successfully coded general framework MARS allows easy testing and implementation of new analysis methods. A new robust method for background suppression was developed which is based on the MARS framework and a full analysis chain including most of the algorithms currently used in Cherenkov astronomy was implemented. The robust software package and the easy and highly flexible setup of the analysis chain allowed to automate the data analysis, previously done manually, to deal with the variable observation conditions.

The implementation of an automation turned out to be a powerful tool for further improving the analysis, because it allows a simple re-analysis of all data with a changed setup. By automatically calculating quality parameters and storing them in a database for all data, e.g. the muon-parameters, a fast and easy cross-check of the data quality is possible. To keep track of the large number of files produced an automatic grouping was implemented which allows easy and direct access to a huge set of data.

The analysis and automation was commissioned: The automatic analysis produces results comparable with refined analyses of the data especially adapted to the observation conditions. The automatic analysis revealed its power by subsequently processing the data as soon as they were available for analysis on a short time scale.

After completion of its construction and the commissioning of all systems and the analysis chain, a large number of sources were observed with the MAGIC-telescope in 2005. To further study the properties of Blazars, a selection of promising candidates, mainly HBL, have been chosen from existing compilations (e.g. Donato et al. (2001)). The main selection criteria were a high X-ray flux, which is assumed to be related to a high flux of very high energy gamma-rays, and a low redshift, in order to avoid the metagalactic pair attenuation near the threshold energy.

Based on this selection the first AGN, namely 1ES 1218+304 at a redshift of $z = 0.182$, emitting very high energy gamma-rays at 100 GeV was discovered. It is one of the two farthest known

AGN emitting in the TeV energy region.

The source was observed in on-/off-observation mode from January 9^{th} to 15^{th} 2005 at zenith angles between 1.5° and 13° during six moonless nights, with a total observation time of 8.2 h. For the analysis 6.5 h off-data, taken between January 9^{th} and January 11^{th}, were used, which match the observation conditions and detector performance of the on-data. Simultaneously the KVA-telescope (www-15) nearby MAGIC observed 1ES 1218+304 in the optical band.

The analysis of the data yields a significance of 6.4 standard deviations for the emission of very high energy gamma-rays from the position of 1ES 1218+304. The calculated lightcurve shows no day-to-day variability and within the statistical errors it is compatible with a constant flux of $F(>100\,\mathrm{GeV}) = (8.7 \pm 1.4) \cdot 10^{-7}\,\mathrm{m}^{-2}\,\mathrm{s}^{-1}$. A differential energy-spectrum, which is compatible with a power law of $F_E(E) = (8.1 \pm 2.1) \cdot 10^{-7} (E/250\,\mathrm{GeV})^{-3.0\pm0.4}\,\mathrm{TeV}^{-1}\,\mathrm{m}^{-2}\,\mathrm{s}^{-1}$ was obtained between 87 GeV and 630 GeV. The spectrum emitted by the source was obtained employing a model describing the attenuation due to pair-production with low-energy photons of the cosmologically evolving extragalactic background Kneiske et al. (2002, 2004).

The basic structure of Active Galactic Nuclei has been outlined. Two well known models for very high energy gamma-ray emission from the AGN's jets, namely synchrotron self-Compton and proton induced cascades, have been presented. A homogeneous, one-zone synchrotron self-Compton model taking the Klein-Nishina cross-section into account has been fitted to the collected multi-wavelength data. It turned out that already this simple model is capable of explaining the data quite well.

By using the optical data measured simultaneously a best fit could be obtained. With the high variations seen by X-ray experiments, upper and lower limits have been obtained. With constraints discussed in Tavecchio et al. (1998) some physical properties (magnetic field and Doppler factor) of the emitting plasma For further constraints measurements of the variability time-scale of the object are required.

The result was compared to the average spectral energy distributions for high-peaked Blazars based on a phenomenological model by Fossati et al. (1998) and a SSC model based approach by Ghisellini et al. (1998). In both cases the shape of the SED of 1ES 1218+304 matches well with the average SED. The luminosity of the object is at the upper limit but still compatible with the average HBL-SED. This can be interpreted as still in line with the classes grouped in the *Blazar-sequence*, according to which the spectral energy distribution of Blazars changes markedly with their luminosity. If high-peaked objects of just slightly higher luminosity would be detected in future observations, they would then contradict the *Blazar-sequence*.

Acknowledgments I thank the Instituto de Astrofísica de Canarias for the excellent working conditions at the Observatorio del Roque de los Muchachos in La Palma and the support of the German BMBF. I also thank Prof. Dr. Karl Mannheim for his advice, strong support of my work and ideas and his believe in the quality of our work.

Special thanks to my girl-friend Daniela Dorner and my colleagues J. Albert, K. Berger, D. Elsässer, D. Höhne, T. Kneiske, M. Meyer, B. Riegel, S. Rügamer and R. Schmitt, for their assistance.

Last but not least I thank the whole MAGIC-collaboration for their effort of planning, building and maintaining this powerful experiment.

A. Quality parameters

Sequence	Events	(1)	(2)	(3)	(4)	(5)	(6)	(7)	(8)
47736	321126	4	3	12	10	4.5	5.1	0.63	0.62
47744	858314	3	3	12	7	4.6	5.2	0.75	0.74
47955	1291034	4	3	12	9	4.7	5.3	0.66	0.66
48170	107042	4	3	10	8	4.9	5.5	0.79	0.77
48174	1449549	6	3	12	12	4.9	5.4	0.76	0.75
48405	1633695	3	3	13	7	4.9	5.5	0.85	0.84
49196	371747	3	3	11	6	4.3	4.9	0.62	0.62
49205	422752	4	3	12	5	4.2	4.8	0.58	0.58
49216	1084020	4	2	10	7	4.2	4.8	0.56	0.56
47667	614350	4	3	12	6	4.4	5.0	0.55	0.56
47684	516763	4	3	12	6	4.3	4.9	0.55	0.56
47698	525157	4	3	7	11	4.4	5.0	0.58	0.58
47988	1758363	3	3	16	14	4.4	5.0	0.53	0.53
48216	1233713	5	3	8	8	4.3	4.9	0.52	0.52
48246	1094134	3	3	11	11	4.5	5.1	0.53	0.53
48275	944843	3	3	11	11	4.3	4.9	0.55	0.55
48298	267605	5	3	14	8	4.6	5.2	0.55	0.54
48305	669512	5	3	14	5	4.9	5.5	0.57	0.57
49022	1517093	3	3	5	4	4.3	4.9	0.60	0.60

Table A.1.: Quality parameters I.
(1) Number of unsuitable pixel inner camera
(2) Number of unsuitable pixel outer camera
(3) Number of unreliable pixel inner camera
(4) Number of unreliable pixel outer camera
(5) Average calibration pulse arrival time inner camera/au
(6) Average calibration pulse arrival time outer camera/au
(7) RMS calibration pulse arrival time inner camera/au
(8) RMS calibration pulse arrival time outer camera/au

Sequence	(9)	(10)	(11)	(12)	(13)	(14)	(15)
47736	0.92	1.35	1.65	0.90	0.360	1.557	10.75
47744	0.93	1.35	1.65	0.90	0.358	1.679	10.75
47955	0.96	1.38	1.67	0.92	0.365	1.553	11.06
48170	0.92	1.33	1.64	0.89	0.351	1.461	10.67
48174	0.91	1.32	1.63	0.88	0.353	1.476	10.75
48405	0.93	1.34	1.65	0.90	0.349	1.439	10.60
49196	0.90	1.30	1.64	0.89	0.351	1.421	10.49
49205	0.89	1.29	1.63	0.89	0.350	1.415	10.47
49216	0.89	1.29	1.57	0.87	0.348	1.405	10.51
47667	0.97	1.40	1.71	0.94	0.358	1.522	10.55
47684	0.98	1.41	1.72	0.95	0.353	1.493	10.62
47698	0.99	1.42	1.73	0.95	0.354	1.487	10.65
47988	1.03	1.45	1.77	0.98	0.330	1.313	10.34
48216	1.01	1.42	1.77	0.97	0.350	1.423	10.44
48246	0.99	1.44	1.72	0.96	0.346	1.392	10.57
48275	1.00	1.41	1.77	0.96	0.353	1.459	10.52
48298	1.00	1.42	1.77	0.97	0.349	1.451	10.51
48305	1.00	1.43	1.77	0.97	0.350	1.443	10.48
49022	0.94	1.34	1.71	0.93	0.350	1.421	10.43

Table A.2.: Quality parameters II.
(9) Average Pedestal-RMS inner camera/phe
(10) Average Pedestal-RMS outer camera/phe
(11) Average signal inner camera/phe
(12) Average signal outer camera/phe
(13) Average relative calibration conversion factor inner camera
(14) Average relative calibration conversion factor outer camera
(15) Average pulse position for pulses >15phe/au

Sequence	(16)	(17)	(18)	(19)	(20)	(21)	(22)	(23)	(24)	(25)
47736	223	1.17	38.1	9.0	0.59	642	102.1	18.9	1090	0.99
47744	224	1.17	37.7	9.3	0.59	1723	99.2	18.1	2904	0.99
47955	223	1.18	54.9	9.2	0.65	2745	101.9	18.0	4215	0.99
48170	236	1.17	22.9	9.4	0.66	231	101.6	17.8	352	0.99
48174	249	1.17	26.4	9.0	0.68	3050	101.5	18.2	4468	0.93
48405	238	1.17	11.8	8.2	0.66	3428	102.5	17.7	5233	0.99
49196	243	1.18	6.7	8.8	0.70	829	101.0	17.7	1184	0.99
49205	241	1.18	6.9	8.5	0.68	934	103.2	19.0	1366	1.00
49216	239	1.18	9.3	9.2	0.68	2237	10¡1.7	18.7	3273	0.99
47667	217	1.17	54.4	9.3	0.63	1329	99.8	18.7	2106	1.00
47684	223	1.17	54.1	8.7	0.63	1082	100.9	18.4	1730	0.99
47698	223	1.17	51.3	8.7	0.59	1049	99.9	17.4	1764	0.99
47988	227	1.18	43.3	9.1	0.73	4209	101.0	18.2	5741	1.00
48216	234	1.18	5.9	9.0	0.70	2818	102.0	17.6	4039	0.99
48246	236	1.18	7.0	8.8	0.69	2438	101.8	17.2	3514	0.99
48275	231	1.18	6.5	9.0	0.68	2108	101.8	18.3	3119	1.00
48298	225	1.18	4.3	8.1	0.66	607	100.7	18.2	922	0.99
48305	222	1.18	5.3	7.9	0.68	1569	100.9	17.9	2322	0.99
49022	237	1.18	11.5	9.2	0.71	3527	102.3	17.8	4977	0.99

Table A.3.: Quality parameters III.
(16) Event rate after image cleaning/Hz
(17) Average number of islands
(18) Maximum relative humidity/%
(19) Camera inhomogeneity parameter/%
(20) Muon rate/Hz
(21) Number of *good* muons
(22) Ratio Average MC Muon Size/Average Data Muon Size/%
(23) Total Point-Spread-Function/mm
(24) Effective on-time/s
(25) Ratio effective on-time/observation time

List of Figures

List of Tables

Bibliography

F. Aharonian.
TeV gamma rays from BL Lac objects due to synchrotron radiation of extremely high energy protons.
New A, 5:377–395, November 2000.

F. Aharonian et al.
Calibration of cameras of the H.E.S.S. detector.
Astroparticle Physics, 22:109–125, November 2004a.

F. Aharonian et al.
Observations of 54 Active Galactic Nuclei with the HEGRA system of Cherenkov telescopes.
A&A, 421:529–537, July 2004b.

F. Aharonian et al.
A New Population of Very High Energy Gamma-Ray Sources in the Milky Way.
Science, 307:1938–1942, March 2005.

F. Aharonian et al.
Evidence for VHE Gamma-ray Emission from the Distant BL Lac PG 1553+113.
A&A, 2006.
in press.

J. Albert et al.
Physics and astrophysics with a ground-based gamma-ray telescope of low energy threshold.
Astroparticle Physics, 23:493–509, June 2005.

J. Albert et al.
Flux Upper Limit on Gamma-Ray Emission by GRB 050713a from MAGIC Telescope Observations.
ApJ, 641:L9–L12, April 2006.

R. Antonucci.
Unified models for active galactic nuclei and quasars.
ARA&A, 31:473–521, 1993.

R. R. J. Antonucci and J. S. Ulvestad.
Extended radio emission and the nature of blazars.
ApJ, 294:158–182, July 1985.

H. Bartko, M. Gaug, A. Moralejo, and N. Sidro.
FADC pulse reconstruction using a digital filter for the MAGIC telescope.
astro-ph, 2005.
astro-ph/0506459.

D. Bastieri et al.
The mirrors of the MAGIC telescope.
In 29^{th} *International Cosmic Ray Conference*, August 2005.
astro-ph/0508274.

M. Begelman and M. Rees.
Gravity's Fatal Attraction: Black Holes in the Universe.
Scientific American Library, 1995.

C. Beixeras et al.
MAGIC II.
In 29^{th} *International Cosmic Ray Conference*, volume 5, page 227, August 2005.
astro-ph/0508274.

V. S. Berezinskii, S. V. Bulanov, V. A. Dogiel, and V. S. Ptuskin.
Astrophysics of cosmic rays.
Amsterdam: North-Holland, 1990, edited by Ginzburg, V.L., 1990.

R. D. Blandford and A. Königl.
Relativistic jets as compact radio sources.
ApJ, 232:34–48, August 1979.

R. D. Blandford and A. Levinson.
Pair cascades in extragalactic jets. 1: Gamma rays.
ApJ, 441:79–95, March 1995.

R. D. Blandford and D. G. Payne.
Hydromagnetic flows from accretion discs and the production of radio jets.
MNRAS, 199:883–903, June 1982.

R. D. Blandford and M. J. Rees.
Some comments on radiation mechanisms in Lacertids.
In *Pittsburgh Conference on BL Lac Objects, Pittsburgh, Pa., April 24-26, 1978, Proceedings. (A79-30026 11-90) Pittsburgh, Pa., University of Pittsburgh, 1978, p. 328-341; Discussion, p. 341-347. NATO-supported research*, pages 328–341, 1978.

R. D. Blandford and R. L. Znajek.
Electromagnetic extraction of energy from Kerr black holes.
MNRAS, 179:433–456, May 1977.

Blandford, R. D.
Gamma ray jets from active galactiv nuclei.
In Gehrels, editor, *Compton Gamma Ray Observatory*, volume 280, page 533, 1993.

P. Blasi and M. Vietri.
On Particle Acceleration around Shocks. II. A Fully General Method for Arbitrary Shock Velocities and Scattering Media.
ApJ, 626:877–886, June 2005.

S. D. Bloom, A. P. Marscher, and W. K. Gear.
Multiwavelength Observations of Flat Radio Spectrum Quasars and Active Galaxies.
BAAS, 25:920–+, May 1993.

A. J. Blustin, M. J. Page, and G. Branduardi-Raymont.
Intrinsic absorbers in BL Lac objects: The XMM-Newton view.
A&A, 417:61–70, April 2004.

C. T. Bolton.
Identification of Cyg X-1 with HDE 226868.
Nature, 235:271, 1972.

S. M. Bradbury et al.
Detection of γ-rays above 1.5TeV from MKN 501.
A&A, 320:L5–L8, April 1997.

S. M. Bradbury and H. J. Rose.
Pattern recognition trigger electronics for an imaging atmospheric Cherenkov telescope.
Nuclear Instruments and Methods in Physics Research A, 481:521–528, April 2002.

Leo Breiman.
Machine Learning 45(1), 5, 2001.

T. Bretz.
Magnetfeldeigenschaften des Spektrometers HADES.
Master's thesis, Technische Universität München, 1999.

T. Bretz.
The MAGIC Analysis and Reconstruction Software.
In 28^{th} *International Cosmic Ray Conference*, August 2003.

T. Bretz.
MARS - Roadmap to a standard analysis.
In 2^{nd} *International Symposium on High Energy Gamma-Ray Astronomy*, July 2004.

T. Bretz.
Standard analysis for the MAGIC telescope.
In 29^{th} *International Cosmic Ray Conference*, volume 4, page 315, August 2005.
astro-ph/0508274.

T. Bretz and D. Dorner.
MARS - A framework for a standard analysis.
In *Towards a network of atmospheric Cherenkov detectors VII*, April 2005.

I. W. A. Browne.
Is it possible to turn an elliptical radio galaxy into a BL Lac object?
MNRAS, 204:23P–27P, July 1983.

J. H. Buckley.
ASTROPHYSICS: What the Wild Things Are.
Science, 279:676–+, January 1998.

M. L. Burns and R. V. E. Lovelace.
Theory of electron-positron showers in double radio sources.
ApJ, 262:87–99, November 1982.

A. Caccianiga, T. Maccacaro, A. Wolter, R. della Ceca, and I. M. Gioia.
The REX Survey: A Search for Radio-emitting X-Ray Sources.
ApJ, 513:51–68, March 1999.

A. Caccianiga and M. J. M. Marchã.
The CLASS blazar survey: testing the blazar sequence.
MNRAS, 348:937–954, March 2004.

M. Catanese and T. C. Weekes.
Very High Energy Gamma-Ray Astronomy.
PASP, 111:1193–1222, October 1999.

A. Celotti.
On the energetics and composition of jets.
New A Rev., 47:525–528, October 2003.

S. Chandrasekhar.
The Maximum Mass of Ideal White Dwarfs.
ApJ, 74:81–+, July 1931.

M. Chiaberge and G. Ghisellini.
Time dependent spectra of blazars.
Memorie della Societa Astronomica Italiana, 68:191–+, 1997.

J. Cortina et al.
Technical performance of the MAGIC telescope.
In 29^{th} *International Cosmic Ray Conference*, August 2005.
astro-ph/0508274.

L. Costamante and G. Ghisellini.
TeV candidate BL Lac objects.
A&A, 384:56–71, March 2002.

L. Costamante, G. Ghisellini, P. Giommi, G. Tagliaferri, A. Celotti, M. Chiaberge, G. Fossati, L. Maraschi, F. Tavecchio, A. Treves, and A. Wolter.
Extreme synchrotron BL Lac objects. Stretching the blazar sequence.
A&A, 371:512–526, May 2001.

A. Daum et al.
First results on the performance of the HEGRA IACT array.
Astroparticle Physics, 8:1–2, December 1997.

R. della Ceca, G. Lamorani, T. Maccacaro, A. Wolter, R. Griffiths, J. T. Stocke, and G. Setti.
The properties of X-ray selected active galactic nuclei. 3: The radio-quiet versus radio-loud samples.
ApJ, 430:533–544, August 1994.

C. D. Dermer.
In *NATO Advanced Study Institute: The Gamma-Ray Sky*, page 39. Dodrecht: Kluwer Academic, 1994.

C. D. Dermer.
Neutrino, Neutron, and Cosmic-Ray Production in the External Shock Model of Gamma-Ray Bursts.
ApJ, 574:65–87, July 2002.

C. D. Dermer and R. Schlickeiser.
Model for the High-Energy Emission from Blazars.
ApJ, 416:458–+, October 1993.

D. Donato, G. Ghisellini, G. Tagliaferri, and G. Fossati.
Hard X-ray properties of blazars.
A&A, 375:739–751, September 2001.

L. Dondi and G. Ghisellini.
Gamma-ray-loud blazars and beaming.
MNRAS, 273:583–595, April 1995.

D. Dorner.
System zum Ausrichten und Nachführen des MAGIC-Teleskops.
Master's thesis, Bayerische Julius-Maximilians-Universität Würzburg, 2003.

D. Dorner, K. Berger, T. Bretz, M. Gaug, et al.
Data managment and processing for the MAGIC telescope.
In 29^{th} *International Cosmic Ray Conference*, volume 5, page 175, August 2005.
astro-ph/0508274.

D. Dorner and T. Bretz.
A concept for data managment and processing.
In *Towards a network of atmospheric Cherenkov detectors VII*, pages 571–575, April 2005.

M. Doro.
The commissioning and characterization of the calibration system of the MAGIC telescope.
Master's thesis, Universitá di Padova, 2004.
`http://wwwmagic.mppmu.mpg.de/publications/theses/LaureaMDoro.ps.gz`.

A. S. Eddington.
Note on "relativistic degeneracy".
MNRAS, 96:20–+, November 1935a.

A. S. Eddington.
On "relativistic degeneracy,".
MNRAS, 95:194–206, January 1935b.

A. Einstein.
Zur Elektrodynamik bewegter Körper.
Annalen der Physik, 17:891–921, 1905.

A. Einstein.
Die Grundlage der allgemeinen Relativitätstheorie.
Annalen der Physik, 49:769–822, 1916.

M. Elvis, D. Plummer, J. Schachter, and G. Fabbiano.
The Einstein Slew Survey.
ApJS, 80:257–303, May 1992.

B. L. Fanaroff and J. M. Riley.
The morphology of extragalactic radio sources of high and low luminosity.
MNRAS, 167:31P–36P, May 1974.

G. G. Fazio and F. W. Stecker.
Predicted high energy break in the isotropic gamma ray spectrum: a test of cosmological origin.
Nature, 226:135–+, 1979.

G. J. Feldman and R. D. Cousins.
Unified approach to the classical statistical analysis of small signals.
Phys. Rev. D, 57:3873–3889, April 1998.

E. Fermi.
Phys. Rev., 75:1169, 1949.

E. Fermi.
Galactic Magnetic Fields and the Origin of Cosmic Radiation.
ApJ, 119:1–+, January 1954.

C. E. Fichtel et al.
The first energetic gamma-ray experiment telescope (EGRET) source catalog.
ApJS, 94:551–581, October 1994.

G. Fossati, L. Maraschi, A. Celotti, A. Comastri, and G. Ghisellini.
A unifying view of the spectral energy distributions of blazars.
MNRAS, 299:433–448, September 1998.

M. Gaug, H. Bartko, J. Cortina, J. Rico, et al.
Calibration of the MAGIC telescope.
In 29^{th} *International Cosmic Ray Conference*, August 2005.
astro-ph/0508274.

G. Ghisellini, A. Celotti, G. Fossati, L. Maraschi, and A. Comastri.
A theoretical unifying scheme for gamma-ray bright blazars.
MNRAS, 301:451–468, December 1998.

G. Ghisellini and P. Madau.
On the origin of the gamma-ray emission in blazars.
MNRAS, 280:67–76, May 1996.

G. Ghisellini and L. Maraschi.
Bulk acceleration in relativistic jets and the spectral properties of blazars.
ApJ, 340:181–189, May 1989.

G. Ghisellini and L. Maraschi.
Are γ-rays from HPQs and BL Lacs due to the same process?
AIP Conf. Proc., 304:616, 1994.

G. Ghisellini, L. Maraschi, and L. Dondi.
Diagnostics of Inverse-Compton models for the γ-ray emission of 3C 279 and MKN 421.
A&AS, 120:C503+, December 1996.

G. Ghisellini, P. Padovani, A. Celotti, and L. Maraschi.
Relativistic bulk motion in active galactic nuclei.
ApJ, 407:65–82, April 1993.

P. Giommi.
private communication, 2006.

P. Giommi et al.
in preparation, 2006.

P. Giommi, M. T. Menna, and P. Padovani.
The sedentary multifrequency survey - I. Statistical identification and cosmological properties of high-energy peaked BL Lacs.
MNRAS, 310:465–475, December 1999.

P. Giommi and P. Padovani.
Bl-Lacertae Reunification.
MNRAS, 268:L51+, May 1994.

P. Giommi, P. Padovani, and E. Perlman.
Detection of exceptional X-ray spectral variability in the TeV BL Lac 1ES 2344+514.
MNRAS, 317:743–749, October 2000.

P. Giommi, S. Piranomonte, M. Perri, and P. Padovani.
The sedentary survey of extreme high energy peaked BL Lacs.
A&A, 434:385–396, April 2005.

F. Goebel, K. Mase, M. Meyer, R. Mirzoyan, M. Shayduk, M. Teshima, et al.
Absolute energy scale calibration of the MAGIC telescope using muon images.
In 29^{th} *International Cosmic Ray Conference*, August 2005.
astro-ph/0508274.

R. J. Gould.
High-Energy Photons from the Compton-Synchrotron Process in the Crab Nebula.
Phys. Rev. Lett., 15:577–579, October 1965.

R. F. Green, M. Schmidt, and J. Liebert.
The Palomar-Green catalog of ultraviolet-excess stellar objects.
ApJS, 61:305–352, June 1986.

F. Halzen and E. Zas.
Giant horizontal air showers. Implications for AGN neutrino fluxes.
Physics Letters B, 289:184–188, September 1992.

R. C. Hartman et al.
The Third EGRET Catalog of High-Energy Gamma-Ray Sources.
ApJS, 123:79–202, July 1999.

G. Hasinger, R. Burg, R. Giacconi, M. Schmidt, J. Trumper, and G. Zamorani.
The ROSAT Deep Survey. I. X-ray sources in the Lockman Field.
A&A, 329:482–494, January 1998.

M. G. Hauser and E. Dwek.
The Cosmic Infrared Background: Measurements and Implications.
ARA&A, 39:249–307, 2001.

Stephen W. Hawking.
Particle creation by black holes.
Comm. Math. Phys., 43:199, 1975.

D. Heck, J. Knapp, J. N. Capdevielle, G. Schatz, and T. Thouw.
CORSIKA: A Monte Carlo Code to Simulate Extensive Air Showers.
Forschungszentrum Karlsruhe, Report FZKA 6019, 1998.
`http://www-ik.fzk.de/corsika/physics\_description/corsika\_phys.html`.

J. J. Hernández-Rey.
The Neutrino Telescope Antares.
Ap&SS, 297:257–267, June 2005.

D. A. Hill and N. A Porter.
Photography of Čerenkov Light from Extensive Air Showers in the Atmosphere.
Nature, 191:690, August 1960.
Letters to Editor.

A. M. Hillas.
Ultra high energy cosmic rays.
In *NATO ASIC Proc. 107: Composition and Origin of Cosmic Rays*, pages 125–148, 1983.

A. M. Hillas.
Cerenkov light images of EAS produced by primary gamma.
In 19^{th} *International Cosmic Ray Conference*, pages 445–448, August 1985.

D. W. Hogg, I. K. Baldry, M. R. Blanton, and D. J. Eisenstein.
The K correction.
astro-ph, October 2002.
astro-ph/0210394.

D. Höhne.
Beobachtung von HESS J1813-178 mit dem MAGIC-Teleskop.
Master's thesis, Bayerische Julius-Maximilians-Universität Würzburg, September 2005.

J. Holder et al.
The First VERITAS Telescope.
submitted, April 2006.
astro-ph/0604119.

D. Horan et al.
Constraints on the Very High Energy Emission from BL Lacertae Objects.
ApJ, 603:51–61, March 2004.

S. Inoue and F. Takahara.
Electron Acceleration and Gamma-Ray Emission from Blazars.
ApJ, 463:555–+, June 1996.

A. Janiuk, B. Czerny, R. Moderski, D. B. Cline, C. Matthey, and S. Otwinowski.
On the origin of the bimodal duration distribution of gamma-ray bursts and the subjet model.
MNRAS, 365:874–884, January 2006.

J. V. Jelley and N. A. Porter.
Čerenkov Radiation from the Night Sky, and its Application to γ-Ray Astronomy.
QJRAS, 4:275–+, September 1963.

T. W. Jones, S. L. O'dell, and W. A. Stein.
Physics of Compact Nonthermal Sources. Theory of Radiation Processes.
ApJ, 188:353–368, March 1974.

K. I. Kellermann, R. Sramek, M. Schmidt, D. B. Shaffer, and R. Green.
VLA observations of objects in the Palomar Bright Quasar Survey.
AJ, 98:1195–1207, October 1989.

Roy Patrick Kerr.
Gravitational field of a spinning mass as an example of algebraically special metrics.
Phys. Rev. Lett., 11:237, 1963.

J. G. Kirk, F. M. Rieger, and A. Mastichiadis.
Particle acceleration and synchrotron emission in blazar jets.
A&A, 333:452–458, May 1998.

J. G. Kirk and P. Schneider.
On the acceleration of charged particles at relativistic shock fronts.
ApJ, 315:425–433, April 1987.

R. W. Klebesadel, I. B. Strong, and R. A. Olson.
Observations of Gamma-Ray Bursts of Cosmic Origin.
ApJ, 182:L85+, June 1973.

T. Kneiske.
Wechselwirkung von Gammastrahlung mit dem metagalaktischen Strahlungsfeld.
PhD thesis, Bayerische Julius-Maximilians-Universität Würzburg, 2004.

T. M. Kneiske, T. Bretz, K. Mannheim, and D. H. Hartmann.
Implications of cosmological gamma-ray absorption. II. modification of gamma-ray spectra.
A&A, 413:807–815, January 2004.

T. M. Kneiske, K. Mannheim, and D. H. Hartmann.
Implications of cosmological gamma-ray absorption. I. Evolution of the metagalactic radiation field.
A&A, 386:1–11, April 2002.

F. Krull.
Soft X-ray excess in Aktiven Galaxienkernen.
PhD thesis, Eberhard-Karls Universität Tübingen, 1997.

H. Kubo et al.
Status of the CANGAROO-III project.
New Astronomy Review, 48:323–329, April 2004.

F. La Franca, L. Gregorini, S. Cristiani, H. de Ruiter, and F. Owen.
Deep VLA observations of an optically selected sample of intermediate redshift QSOs and the optical luminosity function of the radio loud QSOs.
AJ, 108:1548–1556, November 1994.

R. C. Lamb and D. J. Macomb.
Point Sources of GeV Gamma Rays.
ApJ, 488:872–+, October 1997.

G. Lamer, H. Brunner, and R. Staubert.
ROSAT observations of BL Lacertae objects.
A&A, 311:384–392, July 1996.

L. D. Landau and E. M. Lifshitz.
The classical theory of fields.
Course of theoretical physics - Pergamon International Library of Science, Technology, Engineering and Social Studies, Oxford: Pergamon Press, 1971, 3rd rev. engl. edition, 1971.

S. A. Laurent-Muehleisen, R. I. Kollgaard, and E. D. Feigelson.
The Rosat-Green Bank Sample of Intermediate BL Lac Objects.
In *ASP Conf. Ser. 144: IAU Colloq. 164: Radio Emission from Galactic and Extragalactic Compact Sources*, pages 163–+, 1998.

A. Lawrence.
Classification of active galaxies and the prospect of a unified phenomenology.
PASP, 99:309–334, May 1987.

J. E. Ledden and S. L. Odell.
The radio-optical-X-ray spectral flux distributions of blazars.
ApJ, 298:630–643, November 1985.

R. W. Lessard, J. H. Buckley, V. Connaughton, and S. Le Bohec.

A new analysis method for reconstructing the arrival direction of TeV gamma rays using a single imaging atmospheric Cherenkov telescope.
Astroparticle Physics, 15:1–18, March 2001.

T.-P. Li and Y.-Q. Ma.
Analysis methods for results in gamma-ray astronomy.
ApJ, 272:317–324, September 1983.

K. R. Lind and R. D. Blandford.
Semidynamical models of radio jets - Relativistic beaming and source counts.
ApJ, 295:358–367, August 1985.

E. Lorenz.
Status of the 17 m MAGIC telescope.
New Astronomy Review, 48:339–344, April 2004.

D. Lynden-Bell.
Galactic Nuclei as Collapsed Old Quasars.
Nature, 223:690–+, 1969.

D. Lynden-Bell and M. J. Rees.
On quasars, dust and the galactic centre.
MNRAS, 152:461–+, 1971.

M. Lyutikov.
Composition of ultra-relativistic jets.
American Astronomical Society Meeting Abstracts, 206:–+, May 2005.

P. Majumdar, A. Moralejo, C. Bigongiari, O. Blanch, and D. Sobczynska.
Monte Carlo simulation for the MAGIC telescope.
In 29^{th} *International Cosmic Ray Conference*, August 2005.
astro-ph/0508274.

K. Mannheim.
The proton blazar.
A&A, 269:67–76, March 1993.

K. Mannheim.
AGN Models: High-Energy Emission.
In *Very High Energy Phenomena in the Universe; Moriond Workshop*, pages 17–+, 1997.

K. Mannheim.
Possible Production of High-Energy Gamma Rays from Proton Acceleration in the Extragalactic Radio Source Markarian 501.
Science, 279:684–+, January 1998.

K. Mannheim, P. L. Biermann, and W. M. Kruells.
A novel mechanism for nonthermal X-ray emission.
A&A, 251:723–731, November 1991.

K. Mannheim, S. Westerhoff, H. Meyer, and H.-H. Fink.
Beacons at the gamma ray horizon.
A&A, 315:77–85, November 1996.

L. Maraschi, G. Ghisellini, and A. Celotti.
A jet model for the gamma-ray emitting blazar 3C 279.
ApJ, 397:L5–L9, September 1992.

A. P. Marscher.
The Inner Jets of Blazars.
In P. E. Hardee, A. H. Bridle, and J. A. Zensus, editors, *ASP Conf. Ser. 100: Energy Transport in Radio Galaxies and Quasars*, pages 45–+, 1996.

A. P. Marscher and J. P. Travis.
Synchrotron self-Compton interpretation of multiwaveband observations of gamma-ray bright blazars.
A&AS, 120:C537+, December 1996.

A. Mastichiadis and J. G. Kirk.
Variability in the synchrotron self-Compton model of blazar emission.
A&A, 320:19–25, April 1997.

P. Meszaros and M. J. Rees.
Optical and Long-Wavelength Afterglow from Gamma-Ray Bursts.
ApJ, 476:232–+, February 1997.

R. Mirzoyan et al.
The first telescope of the HEGRA air Cherenkov imaging telescope array.
Nuclear Instruments and Methods in Physics Research A, 351:513–526, December 1994.

A. Moralejo et al.
The MAGIC telescope for gamma-ray astronomy above 30 GeV.
Chinese J. Astron. Astrophys., 3:531–538, December 2003.

P. Morrison.
On gamma-ray astronomy.
Il nuovo cimento, Vol. VII, N. 6, 1958.

A. Mücke and R. J. Protheroe.
A proton synchrotron blazar model for flaring in Markarian 501.
Astroparticle Physics, 15:121–136, March 2001.

A. Mücke, R. J. Protheroe, R. Engel, J. P. Rachen, and T. Stanev.
BL Lac objects in the synchrotron proton blazar model.
Astroparticle Physics, 18:593–613, March 2003.

A. Müller.
Lexikon der Astrophysik.
September 2005.
URL `http://www.mpe.mpg.de/~amueller`.

E. Nieppola, M. Tornikoski, and E. Valtaoja.
Spectral energy distributions of a large sample of BL Lacertae objects.
A&A, 445:441–450, January 2006.

Julius Robert Oppenheimer and Hartland Snyder.
On continued gravitational contraction.
Phys. Rev., 56:455, 1939.

W. S. Paciesas et al.
The Fourth BATSE Gamma-Ray Burst Catalog (Revised).
ApJS, 122:465–495, June 1999.

P. Padovani.
The Radio Loud Fraction of QSOs and its Dependence on Magnitude and Redshift.
MNRAS, 263:461–+, July 1993.

P. Padovani and P. Giommi.
The connection between x-ray- and radio-selected BL Lacertae objects.
ApJ, 444:567–581, May 1995.

P. Padovani, E. S. Perlman, H. Landt, P. Giommi, and M. Perri.
What Types of Jets Does Nature Make? A New Population of Radio Quasars.
ApJ, 588:128–142, May 2003.

T. J. Pearson and J. A. Zensus.
Superluminal radio sources.
Cambridge University Press, 1987.

Philip James Edwin Peebles.
Principles of Physical Cosmology.
Princton Series in Physics, 1983.

Roger Penrose.
Gravitational collapse and space-time singularities.
Phys. Rev. Lett., 14:57, 1965.

E. S. Perlman, P. Padovani, P. Giommi, R. Sambruna, L. R. Jones, A. Tzioumis, and J. Reynolds.
The Deep X-Ray Radio Blazar Survey. I. Methods and First Results.
AJ, 115:1253–1294, April 1998.

D. Petry et al.
Detection of VHE γ-rays from MKN 421 with the HEGRA Cherenkov Telescopes.
A&A, 311:L13–L16, July 1996.

Phinney.
Astrophysics of Active Galaxies and QSOs.
1986.

E. Pian, G. Vacanti, G. Tagliaferri, G. Ghisellini, L. Maraschi, A. Treves, C. M. Urry, F. Fiore, P. Giommi, E. Palazzi, L. Chiappetti, and R. M. Sambruna.
BeppoSAX Monitoring of the BL Lac MKN 501.
In *Proceedings of the Fourth Compton Symposium*, volume 410, pages 1412–+, 1997.

E. A. Pier and J. H. Krolik.
Radiation-pressure-supported obscuring tori around active galactic nuclei.
ApJ, 399:L23–L26, November 1992.

E. A. Pier and J. H. Krolik.
Infrared Spectra of Obscuring Dust Tori around Active Galactic Nuclei. II. Comparison with Observations.
ApJ, 418:673–+, December 1993.

M. Pohl and R. Schlickeiser.
On the conversion of blast wave energy into radiation in active galactic nuclei and gamma-ray bursts.
A&A, 354:395–410, February 2000a.

M. Pohl and R. Schlickeiser.
On the conversion of blast wave energy into radiation in active galactic nuclei and gamma-ray bursts.
A&A, 354:395–410, February 2000b.

G. Pühlhofer et al.
The technical performance of the HEGRA system of imaging air Cherenkov telescopes.
Astroparticle Physics, 20:267–291, December 2003.

M. Punch et al.
Detection of TeV photons from the active galaxy Markarian 421.
Nature, 358:477–+, August 1992.

M. J. Rees.
Appearance of Relativistically Expanding Radio Sources.
Nature, 211:468–+, 1966.

B. Riegel.
Systematische Untersuchung der Bildparameter für das MAGIC-Teleskop.
Master's thesis, Bayerische Julius-Maximilians-Universität Würzburg, 2005.

B. Riegel and T. Bretz.
A systematic study of the interdependance of the IACT image parameters.
In 29^{th} *International Cosmic Ray Conference*, volume 5, page 215, August 2005.
astro-ph/0508274.

B. Riegel, T. Bretz, D. Dorner, R. M. Wagner, et al.
A tracking monitor for the MAGIC telescope.
In 29^{th} *International Cosmic Ray Conference*, volume 5, page 219, August 2005.
astro-ph/0508274.

W. Rindler.
Visual horizons in world models.
MNRAS, 116:662–+, 1956.

M. Rowan-Robinson.
On the unity of activity in galaxies.
ApJ, 213:635–647, May 1977.

S. Rügamer.
Master's thesis, Bayerische Julius-Maximilians-Universität Würzburg, 2006.
in preparation.

George B. Rybicki and Alan P. Lightman.
Radiative Processes in Astrophysics.
Wiley-Interscience, 1979.

D. B. Sanders, E. S. Phinney, G. Neugebauer, B. T. Soifer, and K. Matthews.
Continuum energy distribution of quasars - Shapes and origins.
ApJ, 347:29–51, December 1989.

V. L. Sarajedini, R. F. Green, R. E. Griffiths, and K. Ratnatunga.
Compact Nuclei in Galaxies at Moderate Redshift. II. Their Nature and Implications for the Active Galactic Nucleus Luminosity Function.
ApJ, 514:746–764, April 1999.

B. Sbarufatti, A. Treves, and R. Falomo.
Imaging Redshifts of BL Lacertae Objects.
ApJ, 635:173–179, December 2005.

Reinhard Schlickeiser.
Cosmic Ray Astrophysics.
Springer, 2003.

M. Schmidt.
3C 273: a star-like object with large red-shift.
Nature, 197:1040–1040, 1963.

M. Schmidt and R. F. Green.
Counts, evolution, and background contribution of X-ray quasars and other extragalactic X-ray sources.
ApJ, 305:68–82, June 1986.

K. Schwarzschild.
Über das Gravitationsfeld einer Kugel aus inkompressibler Flüssigkeit nach der Einsteinschen Theorie.
In *Sitzungsberichte der königlich preußischen Akademie der Wissenschaften zu Berlin*, pages 424–434, 1916a.
physics/9912033.

K. Schwarzschild.
Über das Gravitationsfeld eines Massenpunktes nach der Einsteinschen Theorie.
In *Sitzungsberichte der königlich preußischen Akademie der Wissenschaften zu Berlin*, pages 189–196, 1916b.
physics/9905030.

N. I. Shakura and R. A. Sunyaev.
Black holes in binary systems. Observational appearance.
A&A, 24:337–355, 1973.

M. Sikora.
Jets in Quasars.
In *ASP Conf. Ser. 227: Blazar Demographics and Physics*, pages 95–+, 2001.

M. Sikora, M. C. Begelman, G. M. Madejski, and J.-P. Lasota.
Are Quasar Jets Dominated by Poynting Flux?
ApJ, 625:72–77, May 2005.

M. Sikora, M. C. Begelman, and M. J. Rees.
Comptonization of diffuse ambient radiation by a relativistic jet: The source of gamma rays from blazars?
ApJ, 421:153–162, January 1994.

M. Sikora, J. G. Kirk, M. C. Begelman, and P. Schneider.
Electron injection by relativistic protons in active galactic nuclei.
ApJ, 320:L81–L85, September 1987.

D. N. Spergel et al.
Three Year Wilkinson Microwave Anisotropy Probe (WMAP) Observations: Implications for cosmology.

in preparation, 2006.
`http://lambda.gsfc.nasa.gov/product/map/dr2/map_bibliography.cfm`.

L. Spitzer.
Physics of Fully Ionized gases.
Interscience, New York, 1956.

F. W. Stecker, O. C. de Jager, and M. H. Salamon.
TeV gamma rays from 3C 279 - A possible probe of origin and intergalactic infrared radiation fields.
ApJ, 390:L49–L52, May 1992.

V. J. Stenger, J. G. Learned, S. Pakvasa, and X. Tata, editors.
High Energy Neutrino Astrophysics, 1992.

R. Svensson.
Non-thermal pair production in compact X-ray sources - First-order Compton cascades is soft radiation fields.
MNRAS, 227:403–451, July 1987.

F. Tavecchio, L. Maraschi, and G. Ghisellini.
Constraints on the Physical Parameters of TeV Blazars.
ApJ, 509:608–619, December 1998.

D. J. Thompson et al.
The Second EGRET Catalog of High-Energy Gamma-Ray Sources.
ApJS, 101:259–+, December 1995.

C. M. Urry and P. Padovani.
Unified Schemes for Radio-Loud Active Galactic Nuclei.
PASP, 107:803–+, September 1995.

C. M. Urry, R. Scarpa, M. O'Dowd, R. Falomo, J. E. Pesce, and A. Treves.
The Hubble Space Telescope Survey of BL Lacertae Objects. II. Host Galaxies.
ApJ, 532:816–829, April 2000.

M.-P. Véron-Cetty and P. Véron.
A catalogue of quasars and active nuclei: 11th edition.
A&A, 412:399–403, December 2003.

C. von Montigny et al.
High-Energy Gamma-Ray Emission from Active Galaxies: EGRET Observations and Their Implications.
ApJ, 440:525–+, February 1995.

S. J. Wagner et al.
High-Energy Gamma Rays from PKS 1406-076 and the Observation of Correlated Gamma-Ray and Optical Emission.
ApJ, 454:L97+, December 1995.

J. F. C. Wardle, R. L. Moore, and J. R. P. Angel.
The radio morphology of blazars and relationships to optical polarization and to normal radio galaxies.
ApJ, 279:93–98, April 1984.

E. Waxman.
Cosmological Gamma-Ray Bursts and the Highest Energy Cosmic Rays.
Phys. Rev. Lett., 75:386–389, July 1995.

T. C. Weekes.
Very high energy gamma-ray astronomy.
Astronomy and Astrophysics. Institute of Physics Publishing, 2003.

T. C. Weekes, M. F. Cawley, D. J. Fegan, K. G. Gibbs, A. M. Hillas, P. W. Kowk, R. C. Lamb, D. A. Lewis, D. Macomb, N. A. Porter, P. T. Reynolds, and G. Vacanti.
Observation of TeV gamma rays from the Crab nebula using the atmospheric Cerenkov imaging technique.
ApJ, 342:379–395, July 1989.

T. C. Weekes et al.
Observations of gamma-ray sources at energies >300GeV.
A&AS, 120:C603+, December 1996.

T. C. Weekes et al.
VERITAS: the Very Energetic Radiation Imaging Telescope Array System.
Astroparticle Physics, 17:221–243, May 2002.

D. G. Wentzel.
Fermi Acceleration of Charged Particles.
ApJ, 137:135–+, January 1963.

www-01.
`http://www.nrao.edu/imagegallery/`, 2006.
Credit: NRAO/AUI/NSF.

www-02.
`http://integral.esa.int/integ_pictures.html`, 2006.

www-03.
`http://www.spacetelescope.org/images/`, 2006.
Credit: ESA/NASA, the AVO Project and Paolo Padovani.

www-04.
http://chandra.harvard.edu/resources/illustrations/xlightScatter.html, 2006.

www-05.
http://www.mpi-hd.mpg.de/hfm/CosmicRay/shower.png, 2006.

www-06.
http://abyss.uoregon.edu/~js/glossary/cosmic_rays.html, 2006.

www-07.
http://magic.astro.uni-wuerzburg.de/mars/, 2006.

www-08.
http://earth.google.com, 2006.

www-09.
http://star-www.rl.ac.uk/star/docs/sun67.htx/sun67.html, 2006.

www-10.
http://root.cern.ch, 2006.

www-11.
http://magic.astro.uni-wuerzburg.de/mars/htmldoc/, 2006.

www-12.
http://www.mysql.com, 2006.

www-13.
http://chandra.harvard.edu/resources/illustrations/quasar.html, 2006.
Credit: NASA/CXC, Melissa Weiss.

www-14.
http://www.asdc.asi.it/blazars/, 2006.

www-15.
http://tur3.tur.iac.es/, 2006.

www-16.
http://altamira.asu.cas.cz/iblwg/show.php?id=131, 2006.

www-17.
http://nedwww.ipac.caltech.edu/cgi-bin/nph-objsearch?objname=1es1218+304, 2006.

List of Publications

Printed articles

- Diploma Thesis, Technische Universität München (1999), Magnetfeldeigenschaften des Spektrometers HADES.
- Chinese Journal of Astronomy and Astrophysics 3, 531-538 (2003), A. Moralejo, ..., T. Bretz, et al., The MAGIC telescope for gamma-ray astronomy above 30 GeV
- A&A 413, 807-815 (2004), T. M. Kneiske, T. Bretz, K. Mannheim, D. H. Hartmann, Implications of cosmological gamma-ray absorption. II. Modification of gamma-ray spectra
- astro-ph/0403180, C. Beixeras, ..., T. Bretz, et al., Design studies for a European Gamma-ray observatory
- NIM A 518, 188-192 (2004), C. Beixeras, ..., T. Bretz, et al., Comissioning and first tests of the MAGIC telescope
- In Proc., *28th International Cosmic Ray Conference*, 2943 (2004), T. Bretz, D. Dorner, R. Wagner, et al., The tracking system of the MAGIC Telescope
- In Proc., *28th International Cosmic Ray Conference*, 2947 (2004), T. Bretz, R. Wagner, et al., The MAGIC Analysis and Reconstruction Software
- Astroparticle Physics 23, 493-509 (2005), J. Albert, ..., T. Bretz, et al., Physics and astrophysics with a ground-based gamma-ray telescope of low energy threshold
- AIP Conf. Proc. 745: High Energy Gamma-Ray Astronomy, 730-735 (2005), T. Bretz, MAGIC – Roadmap to a standard analysis
- In *Towards a Network of Atmospheric Cherenkov Detectors VII*, eds. B. Degrange, G. Fontaine, 571-575 (2005), D. Dorner and T. Bretz, A concept of Datamanagment and Processing,
- In *Towards a Network of Atmospheric Cherenkov Detectors VII*, T. Bretz and D. Dorner, MARS – A framework for event-based analysis
- In Proc., *29th International Cosmic Ray Conference* 4, 295 (2006), J. Albert, T. Bretz, et al., First observations of the Giant Radio Galaxy M87 in the 100 GeV Energy Domain with the MAGIC Telescope

- In Proc., *29th International Cosmic Ray Conference* 4, 311 (2006), T. Bretz, et al., Comparison of On-Off and Wobble mode observations for MAGIC

- In Proc., *29th International Cosmic Ray Conference* 4, 315 (2006), T. Bretz, et al., Standard Analysis for the MAGIC Telescope

- In Proc., *29th International Cosmic Ray Conference* 4, 335 (2006), M. Meyer, T. Bretz, et al., MAGIC observations of high-peaked BL Lacertae objects

- In Proc., *29th International Cosmic Ray Conference* 5, 175 (2006), D. Dorner, T. Bretz, et al., Data Managment and Processing for the MAGIC Telescope

- In Proc., *29th International Cosmic Ray Conference* 5, 215 (2006), B. Riegel, T. Bretz, et al., A systematic study of the interdependence of IACT image parameters

- In Proc., *29th International Cosmic Ray Conference* 5, 219 (2006), B. Riegel, T. Bretz, et al., A tracking monitor for the MAGIC Telescope

- In Proc., *29th International Cosmic Ray Conference* 5, 227 (2006), C. Beixeras, ..., T. Bretz, et al., MAGIC II

- ApJ Letters 637, L41-L44 (2006), J. Albert, ..., T. Bretz, et al., MAGIC Observations of Very High Energy γ-Rays from HESS J1813-178

- ApJ Letters 638, L101-L104 (2006), J. Albert, ..., T. Bretz, et al., Observation of Gamma Rays from the Galactic Center with the MAGIC Telescope

- ApJ 639, 761-765 (2006), J. Albert, ..., T. Bretz, et al., Observation of Very High Energy Gamma-Ray Emission from the Active Galactic Nucleus 1ES 1959+650 Using the MAGIC Telescope

- ApJ Letters 641, L9-L12 (2006), J. Albert, ..., T. Bretz, et al., Flux Upper Limit on Gamma-Ray Emission by GRB 050713a from MAGIC Telescope Observations

- ApJ Letters, in press, J. Albert, ..., T. Bretz, et al., Observation of VHE Gamma Radiation from HESS J1834-087/W41 with the MAGIC Telescope

- ApJ Letters, in press, J. Albert, ..., T. Bretz, et al., Discovery of VHE gamma-ray emission from 1ES1218+304

- ApJ, submitted, J. Albert, ..., T. Bretz, et al., Observation of Mkn 421 with the MAGIC Telescope

Talks and Posters

- DPG 2001 (T604.4), Bonn, 2001, Beobachtung von Gamma Ray Bursts mit dem MAGIC Teleskop
- AG Tagung, Berlin, Germany, 2002, T. M. Kneiske, Karl Mannheim and T. Bretz, Upper Limit for the dust enshrouded SFR in the universe
- Astroteilchenphysik in Deutschland, Karlsruhe, 2003, T. Bretz, D. Dorner and R. Wagner, The Magic Analysis and reconstruction software
- Astroteilchenphysik in Deutschland, Karlsruhe, 2003, T. Bretz, D. Dorner and R. Wagner The Tracking System of the Magic Telescope
- DPG 2004, Mainz, 2004, T. Bretz, D. Dorner and R. Wagner, Die MAGIC Analysesoftware MARS
- DPG 2004, Mainz, 2004, R. Wagner, T. Bretz und D. Dorner, Das Antriebssystem des MAGIC-Teleskops
- DPG 2004, Mainz, 2004, D. Dorner, T. Bretz und R. Wagner, Der Camera Oscillation Monitor des MAGIC-Teleskops
- Seminar Astroteilchenphsik, Universität Würzburg, Mai 2004, Wie funktioniert eigentlich Magic?
- Seminar Astroteilchenphsik, Universität Würzburg, Mai 2004, Statistical learning methods
- Astroteilchenphysik in Deutschland, DESY Zeuthen, 2005 Observation of VHE Gamma Radiation from Galactic Source with the MAGIC Telescope
- Astroteilchenphysik in Deutschland, DESY Zeuthen, 2005 Automatische Datenanalyse für das MAGIC-Teleskop - Überblick und Ergebnisse
- Astroteilchenphysik in Deutschland, DESY Zeuthen, 2005 VHE Gamma ray spectrum of 1ES 1218+304
- Astroteilchenphysik in Deutschland, DESY Zeuthen, 2005 A systematic study of the interdependence of the IACT image parameters
- DPG 2006 (T306.5), Dortmund, 2006, Observation of extragalactic sources above 100 GeV with the MAGIC telescope
- DPG 2006 (T407.1), Dortmund, 2006, Spektrale Energieverteilung von 1ES 1218+304
- DPG 2006 (T606.7), Dortmund, 2006, Automatische Datananalyse für abbildende Cherenkov Teleskope